J. Fluid Mech. (1997), *vol.* 350, *pp.* 29–96. Printed in the United Kingdom

Vorticity, strain-rate and dissipation characteristics in the near-wall region of turbulent boundary layers

By ANANT HONKAN AND YIANNIS ANDREOPOULOS

Experimental Fluid Mechanics and Aerodynamics Laboratory, Department of Mechanical Engineering, The City College of the City University of New York, Convent Avenue and 140th Street, New York, NY 10031, USA

(Received 17 April 1996 and in revised form 27 May 1997)

Experimental results are presented that reveal the structure of a two-dimensional turbulent boundary layer which has been investigated by measuring the time-dependent vorticity flux at the wall, vorticity vector, strain-rate tensor and dissipation-rate tensor in the near-wall region with spatial resolution of the order of 7 Kolmogorov viscous length scales. Considerations of the structure function of velocity and pressure, which constitute vorticity flux and vorticity, indicated that, in the limit of vanishing distance, the maximum attainable content of these quantities which corresponds to unrestricted resolution, is determined by Taylor's microscale. They also indicated that most of the contributions to vorticity or vorticity flux come from the uncorrelated part of the two signals involved. The measurements allowed the computation of all components of the vorticity stretching vector, which indicates the rate of change of vorticity on a Lagrangian reference frame if viscous effects are negligible, and several matrix invariants of the velocity gradient or strain-rate tensor and terms appearing in the transport equations of vorticity, strain rate and their squared fluctuations. The orientation of vorticity revealed several preferential directions. During bursts or sweeps vorticity is inclined at 35° to the longitudinal direction. It was also found that there is high probability of the vorticity vector aligning with the direction of the intermediate extensive strain corresponding to the middle eigenvector of the strain-rate matrix. The results of the joint probability distributions of the vorticity vector orientation angles showed that these angles may be related to those of hairpin vortex structures. All invariants considered exhibit a very strong intermittent behaviour which is characterized by large-amplitude bursts which may be of the order of 10 r.m.s. values. Small-scale motions dominated by high rates of turbulent kinetic energy dissipation and high enstrophy density are of particular interest. It appears that the fluctuating strain field dominates the fluctuations of pressure more than enstrophy. Local high values of the invariants are also often associated with peaks in the shear stress.

1. Introduction

Most of the experimental research conducted so far on turbulent flows has been aimed mainly at gathering information on the velocity field in different types of flow configurations, which enhanced our understanding of the underlying physics of these flows. The velocity field, however, is not well suited for defining and identifying organized structures in time-dependent vortical flows because the streamlines and

pathlines are completely different in two different inertial frames of reference. Better understanding of the nature of turbulent structures and vortex motions of turbulent flows, particularly in the high-wavenumber region, often requires spatially and temporally resolved measurements of the so-called structure function of velocity ΔU or pressure Δp. Thus obtaining experimental information on velocity or pressure derivatives may provide insight into the complicated fluid dynamics phenomena of turbulent flows. The availability of these measurements, even in the case of the simplest possible wall-bounded flows, for example that in a zero-pressure-gradient incompressible two-dimensional boundary layer over a smooth flat plate, will lead to information on important quantities like vorticity, rate-of-strain tensor and its matrix invariants and dissipation rate of turbulent kinetic energy, all of which are therefore well suited for describing physical phenomena in vortical flows.

The incompressible Navier–Stokes equations in tensor notation

$$\frac{\mathrm{D}u_i}{\mathrm{D}t} = -\frac{1}{\rho}\frac{\partial p}{\partial x_i} + \frac{1}{\rho}\frac{\partial \tau_{ki}}{\partial x_k} \tag{1.1}$$

give a coupled set of equations for the vorticity $\omega_k = \epsilon_{ijk}\,\partial u_j/\partial x_i$ and the rate-of-strain-tensor $s_{ij} = \frac{1}{2}[\partial u_i/\partial x_j + \partial u_j/\partial x_i]$ or simply the strain tensor in a Lagrangian reference frame (She, Jackson & Orszag 1991)

$$\frac{\mathrm{D}\omega_i}{\mathrm{D}t} = s_{ik}\,\omega_k + \nu\frac{\partial^2 \omega_i}{\partial x_k\,\partial x_k}, \tag{1.2}$$

$$\frac{\mathrm{D}s_{ij}}{\mathrm{D}t} = -s_{ik}\,s_{kj} - \tfrac{1}{4}(\omega_i\,\omega_j - \delta_{ij}\,\omega_k\,\omega_k) - \frac{1}{\rho}\frac{\partial^2 p}{\partial x_i\,\partial x_j} + \nu\frac{\partial^2 s_{ij}}{\partial x_k\,\partial x_k}, \tag{1.3}$$

$$\frac{1}{\rho}\frac{\partial^2 p}{\partial x_k\,\partial x_k} = \tfrac{1}{2}\omega_k\omega_k - s_{ik}\,s_{ik}, \tag{1.4}$$

where $(\mathrm{D}/\mathrm{D}t = \partial/\partial t + u_k\,\partial/\partial x_k$ is the total derivative, τ_{ki} is the shear stress, p is the pressure, ρ is the density of the fluid and ν is the kinematic viscosity. The transport equation for vorticity describes two dynamically significant processes for the vorticity vector $\boldsymbol{\omega}$, namely that of stretching or compression by the strain s_{ik} and viscous diffusion down a vorticity gradient. The viscous term may also describe reconnection of vortex lines at very small scales due to viscosity. The convection of vorticity has the characteristic that it is preserved on a particle path, which implies that the vorticity can only be transferred to the neighbouring fluid particle by diffusion, i.e. by the effect of viscosity. The diffusion together with the convection results in the spread/decay of vorticity and thus plays a vital role in the development of vortical flows. Unlike Navier–Stokes equations for momentum conservation, the pressure term does not appear explicitly in the vorticity transport equation and therefore enables simplification in the computation and interpretation of the theoretical models of more 'complex' flows.

The dynamical equation for the strain s is more complex. In addition to the nonlinear interaction and viscous smoothing, the strain undergoes rotation due to vorticity and is subjected to the non-local action of the pressure hessian $\partial^2 p/(\partial x_i\,\partial x_j)$.

When a fluid element approaches the wall of a bounded flow from the outer part and subsequently comes in direct contact with the stationary surface its vorticity will change because of the no-slip condition at the wall. If it were irrotational initially it will acquire vorticity and if it were vortical its vorticity will change. The quantity which

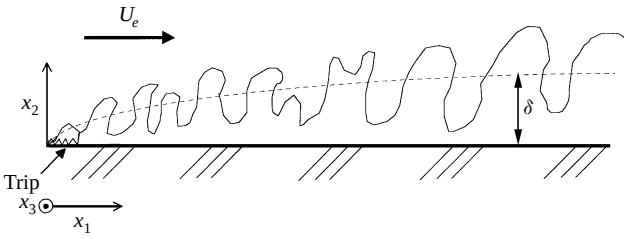

FIGURE 1. Coordinate system in the boundary layer flow.

describes this process is the vorticity gradient normal to the wall $-[\partial\omega_k/\partial x_2]_{wall}$ (see figure 1 for the coordinate system definition) which is called the vorticity flux density, a term first introduced by Lighthill (1963) who in fact defined it for two-dimensional flows by analogy to Fourier's heat conduction as $-\nu[\partial\omega_k/\partial x_2]_{wall}$. The term 'vorticity flux' describes the rate of vorticity production *at the wall* which then enters the flow. In that sense it is more important to know the amount of vorticity entering the flow than the vorticity at the wall. Vorticity dynamics *inside* the flow are, however, best described by using vorticity as a variable. Panton (1984) defines vorticity flux by the expression

$$\boldsymbol{\sigma}_i = -\nu \boldsymbol{n}\cdot(\boldsymbol{\nabla}\boldsymbol{\omega}), \tag{1.5}$$

where $\boldsymbol{n}$ is unit vector normal to the surface and pointing away toward the fluid, which can now be applied to three-dimensional flows. Lyman (1990) looked at the analogy to Fourier's law of heat conduction and proposed another definition of vorticity flux as

$$-\nu \boldsymbol{n}\times(\boldsymbol{\nabla}\times\boldsymbol{\omega}). \tag{1.6}$$

Although the two definitions are not equivalent, both give the same result when they are integrated over a closed control surface.

The vorticity flux at a boundary does not only describe the vorticity source strength on the boundary but it is also related to the total force acting on this surface. Wu & Wu (1996) have provided a formulation for the drag and lift forces acting on a body in terms of vorticity flux at the solid boundary.

The momentum equation evaluated at the wall, where the velocity vector is identically zero because of no-slip conditions, yields

$$\frac{\partial p}{\partial x_i} = \rho\frac{\partial \tau_{ki}}{\partial x_k} \tag{1.7}$$

and

$$\frac{\partial p}{\partial x_i} = -\mu\varepsilon_{ijk}\frac{\partial \omega_k}{\partial x_j}. \tag{1.8}$$

Equation (1.8) indicates that the wall pressure gradient generates flux of vorticity into the fluid and shows that there is a strong coupling between pressure and vorticity. This relation is not apparent in the vorticity transport equation since the latter does not include any pressure term as shown in (1.2).

The present paper reports on new results based on spatially and temporally resolved measurements of the three components of vorticity ω_k, all terms of the rate-of-strain tensor s_{ij} and total dissipation $2\nu s_{ij}s_{ij}$ and several matrix invariants of the velocity gradient and strain-rate tensors inside a two-dimensional incompressible turbulent boundary layer. Ensemble averages of the data conditioned on large excursions of vorticity or vorticity flux at the wall beneath the flow will be also presented.

The difficulties associated with the measurements of velocity gradients in turbulent flows are described in the recent review article by Wallace & Foss (1995) where almost all of the available techniques are discussed in detail and existing data are compared. The majority of the techniques are based on thermal anemometry or on optical methods. These authors demonstrated that thermal anemometry can be used satisfactorily to provide point measurements of vorticity over longer times than optical techniques, which are capable of producing global measurements of vorticity over only very short times. The review concludes that thermal anemometry methods, to date, are the principal experimental source of knowledge about statistical properties of turbulent flow vorticity fields.

The objectives of the present work therefore are as follows:

(i) To design and develop a new probe for measurements of the velocity gradient tensor which is economical, reliable and based on thermal anemometry techniques well established in the field;

(ii) to perform time-dependent measurements of velocity, vorticity vector, rate-of-strain tensor and dissipation using this probe in the turbulent boundary layer and compare major statistical properties including those of vorticity with the existing data, and further understand the dynamic processes associated with turbulence in the flow near the wall by applying conditional sampling techniques to the acquired data;

(iii) to obtain estimates of the vorticity flux at the wall beneath the boundary flow by carrying out time-dependent measurements of pressure gradients by a special pressure module combined with simultaneous measurements of velocity gradients off the wall.

It is hoped that this modest attempt will provide additional information on the dynamics of the near-wall vortical structures.

2. Experimental arrangement, instrumentation and techniques

2.1. *Flow facility*

All the experimental investigations in this research have been carried out in the wind tunnel of The Mechanical Engineering Department, at CCNY (figure 2). It is of open-ended suction type, with 4 ft $\times$ 4 ft cross-section and has a 28 ft long working area. It is powered by a 20 hp, 460 V, three phase frequency-controlled AC motor, driving an axial fan with seven blades rotating at a maximum r.p.m. of 1750 delivering 32000 cubic ft min^{-1} capacity providing a maximum speed of 11.5 m s^{-1} in the working section. The flow velocity can be controlled by varying the frequency from 0 to 100% in 5% increments. The motor and fan assembly is housed in a sound absorbing diffuser, allowing low noise operation of the facility and low levels of acoustical noise transmitted in the working section. It is also mounted on a frame which rests on eight springs to minimize vibration and isolates the motor and fan assembly from the working section. Three sides, i.e. top, bottom and one wall of the working section, are of 1 in. plywood while the other wall has four Plexiglas windows also of 1 in. thickness for observation. The inside of the working section is painted black to aid in flow visualization studies. The inlet of the contraction section is fitted with honeycomb followed by three layers of fine steel screen to obtain uniform flow of turbulence intensity less than 0.1% for the maximum speed in the working section. This contraction section is 12 ft $\times$ 12 ft at one end narrowing down to 4 ft $\times$ 4 ft, resulting in 9:1 contraction ratio.

The boundary layer under investigation is developed on the floor of the wind tunnel and transition to a stable turbulent flow is triggered by a 1 in. wide strip of medium-

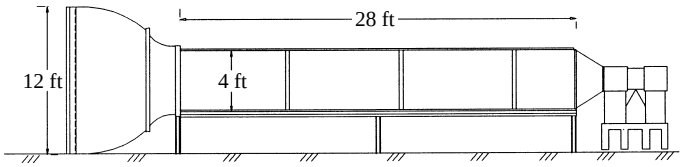

FIGURE 2. Wind tunnel facility.

U_e(m s^{-1})	δ (mm)	θ/δ^* (mm)	c_f	u_τ (m s^{-1})	Re_θ
3.2	140	13.6/17.5	0.0033	0.13	2790

TABLE 1. Principal flow parameters.

grit sandpaper which is glued on the floor across the entire span upstream at the entrance of the working section to obtain a fully developed turbulent boundary layer at the measuring location 22 ft downstream for the test velocity of 3.2 m s^{-1}. The spanwise uniformity of the flow was checked by Preston and Pitot tube traverses 12 in. on either side of the measuring location and it was found to be within the range suggested by Brederode & Bradshaw (1974) for minimum three-dimensional effects in nominally two-dimensional boundary layers. The skin friction coefficient c_f computed from these tests agreed with the values obtained from Clauser charts. The coefficient of skin fraction c_f was evaluated at several Reynolds numbers in the working section and a plot of these values against the Reynolds number based on the momentum thickness θ is shown in Andreopoulos & Agui (1996). On this plot the data of Coles (1962), Schewe (1983) and Spalart (1988) are also shown for comparison. The present values of c_f in the worst case are about 3% higher than those from the analysis by Coles of Weighard's data. The mean velocity profile as measured at the centre of the tunnel width by a Pitot tube indicated a well-developed turbulent boundary layer flow for the investigations.

The principal parameters of the flow are stated in table 1.

2.2 *The individual triple wire probe*

The probe essentially consists of a set of three triple hot wires and several key features of the individual triple-hot-wire probe are as follows.

Each sensor of the triple wire is mutually orthogonal to the others, thus oriented at approximately 54.7° to the probe axis. Each of the 2.5 μm diameter tungsten sensors is welded on two individual prongs which have been tapered at the tips. Thus each sensor is operated independently since no common prongs are used. The hot-wire output voltage E is related to the effective coding velocity U_{eff} 'as seen by the sensor' through the well-know King's law:

$$E^2 = A + BU_{eff}^n. \tag{2.1}$$

The effective cooling velocity is related to that measured during the calibration in at least three different ways: (i) 'Cosine law' as stipulated by Bradshaw (1971), which utilizes the effect of cooling by only one component of velocity, (ii) Hinze's (1959) relation, which accounts for two components on the cooling and (iii) Jorgensen's (1971) expression which takes into consideration the full three-dimensional cooling effect on the sensor. Measurements made by single or cross-wires have always ignored

the effect of at least one component of velocity in the expression for U_{eff}. It has been demonstrated through many experimental tests on hot-wire anemometry that Jorgensen's equation accurately represents the directional response of the hot wire to both yaw and pitch angles up to 70° and so will also be used for the present probe. The effective velocity is related to U_N, U_T and U_B, the normal, tangential and binormal components of the velocity vector respectively, by

$$U_{eff}^2 = U_N^2 + k^2 U_T^2 + h^2 U_B^2, \tag{2.2}$$

where k and h are yaw and pitch coefficients. Details of the techniques associated with the use of triple-wire probes can be found in Andreopoulos (1983*a*) while estimates of errors related to probe geometry and turbulence intensity are described by Andreopoulos (1983*b*).

It has been reported by Willmarth & Bogar (1977), Chang, Adrian & Jones (1983), Willmarth (1985) and Lekakis, Adrian & Jones (1989) that the hot-wire response equations may introduce multiple solutions. This is attributed to the strong dependence of the nonlinear hot-wire output on the yaw and pitch angle of the velocity vector in combination with the probe geometry. This led many researchers to introduce a fourth wire on their triple-wire probes in order to improve the yaw and pitch response (see Tsinober, Kit & Dracos 1992; Marasli, Nguyen & Wallace 1993).

The work of Honkan & Andreopoulos (1993) introduced the following *realizability condition* which the hot-wire response should satisfy in order to avoid multiple solutions. If it is assumed that each of the three output voltages of the triple-hot-wire probe is a continuous function of the velocity vector of the flow, i.e.

$$E_1 = E_1(Q, \gamma, \delta), \quad E_2 = E_2(Q, \gamma, \delta), \quad E_3 = E_3(Q, \gamma, \delta), \tag{2.3}$$

where Q is the magnitude of the velocity vector, γ is the pitch angle and δ is the yaw angle, then it can be concluded that (2.3) define mathematically a mapping of the $\{Q, \gamma, \delta\}$ three-dimensional space onto the $\{E_1, E_2, E_3\}$ three-dimensional space. If the above functions and their partial derivatives are continuous at any point inside a domain T of the three-dimensional space, then the condition for uniqueness of the above mapping is (Apostol 1981)

$$\boldsymbol{J} = \begin{bmatrix} \dfrac{\partial \mathrm{E}_1}{\partial Q} & \dfrac{\partial E_2}{\partial Q} & \dfrac{\partial E_3}{\partial Q} \\ \dfrac{\partial E_1}{\partial \gamma} & \dfrac{\partial E_2}{\partial \gamma} & \dfrac{\partial E_3}{\partial \gamma} \\ \dfrac{\partial E_1}{\partial \delta} & \dfrac{\partial E_2}{\partial \delta} & \dfrac{\partial E_3}{\partial \delta} \end{bmatrix} \neq 0. \tag{2.4}$$

The functional relations in (2.3) can be established through appropriate calibrations and if $\boldsymbol{J}$ does not change sign at any point inside a defined domain, they can be inverted to obtain unique measurements of the velocity vector.

The above condition is very general and it can be applied to any type of probe configuration in terms of geometry, orientation or numbers of wires. It can be expected, however, that not all types of probe configuration automatically satisfies the realizability condition (2.4).

The anemometer output voltages E_1, E_2 and E_3, of the three hot wires are mapped one-to-one to the magnitude of the calibration velocity Q, pitch angle γ and yaw angle δ:

$$(E_1, E_2, E_3) \leftrightarrow (Q, \gamma, \delta). \tag{2.5}$$

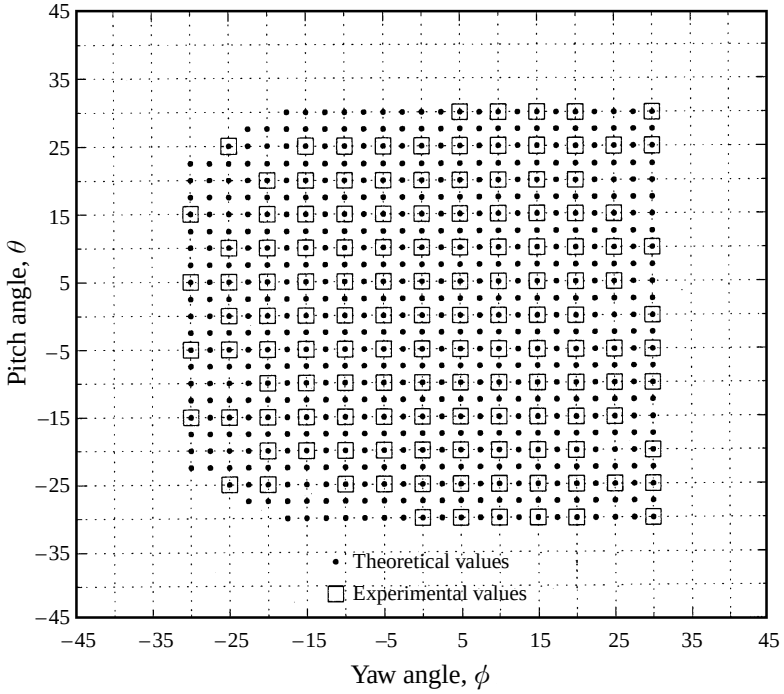

FIGURE 3. Validity domain of the hot-wire probe including all nine wires.

As already mentioned, this mapping is unique if the Jacobian is non-zero. The nine elements of this Jacobian are the sensitivities of each of the hot-wire output voltages with respect velocity, pitch and yaw angles. The first attempt to verify the uniqueness of the mapping for this type of orthogonal-triple-wire probe was reported by Vrettos (1984).

During calibration procedures, the functional relation $E_i = E_i(Q, \gamma, \delta)$, with $i = 1, 2, 3$, was determined. Since Q, γ, δ, were varied by constant increments, consecutive points in the $[Q, \gamma, \delta]$-space represent an orthogonal paralleloepiped. However, this shape is mapped onto an irregular prism where the voltages E_i are not equally spaced. The sensitivities appearing in the Jacobian were computed from finite differences of the corresponding quantities obtained by calibration.

Figure 3 shows a plot of the sign of the Jacobian as a function of pitch and yaw angles, γ and δ. It represents the validity domain or acceptance cone of the triple hot wire as determined by the non-changing sign of the Jacobian. In general the Jacobian is a function of Q, γ and δ. The sign of $\boldsymbol{J}$, however, has been found experimentally to be independent of Q for almost any γ or δ except close to the outer edges of the validity domain. The results shown in figure 3 indicate no change in sign of the Jacobian and therefore they suggest that the mapping is unique. On the same figure the 'theoretical' values have been plotted as calculated using King's law and Jorgensen's expression for the effective velocity. They agree very well with those obtained experimentally except very close to the edges of the domain where theoretical values of the sign of the Jacobian are extended more than the experimental ones.

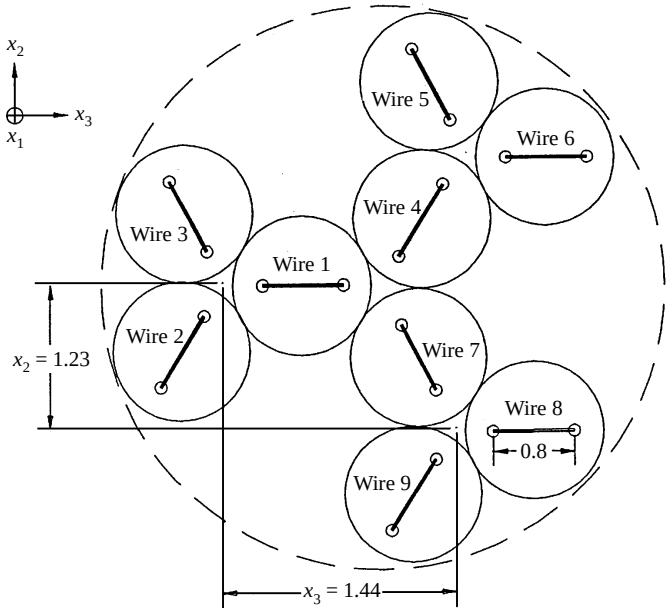

FIGURE 4. Sensor arrangement and probe dimensions in mm.

2.3. *Physical characteristics of the new probe for measurements of gradient velocity tensor*

The probe, shown schematically in figure 4 consists of a set of three individual triple-hot-wire sensors put together so that the probe remains geometrically axisymmetric. In selecting the vorticity probe dimensions several considerations had to be taken into account during the design process. (i) The individual wire length l_w should be as small as possible so that small scales can be resolved adequately. (ii) The size of the individual triple-hot-wire probe, l_p should be as small as possible to satisfy the assumption that the velocity does not change substantially across the probe. Small wire spacing, however, can lead to thermal interference and cross-talk between the wires. (iii) Since vorticity or strain rate will be computed from velocity gradients, spacing of the individual probes should be finite so that velocity gradients do not 'disappear'. If this spacing becomes small the effect of noise may overwhelm the signal (W. K. George 1993, personal communication, and Wallace & Foss 1995). (iv) Each of the wires should be controlled independently from the others. The use of one common prong as in the case of Balint, Wallace & Vukoslavčević (1991) may create problems such as imbalance under dynamic conditions. (v) The transfer function of the hot-wire/anemometer system should be a three-dimensional one. This suggests that the probe should be able to respond to yaw and pitch angle variations of the velocity vector in addition to its magnitude. Very often King's law is confined to contributions from one or two velocity components only. While this assumption simplifies computations and it is adequate for measurements in flows with low turbulence intensity, it is inadequate for measurements in relatively high turbulence intensity. Very close to the wall fluctuations of the three velocity components are very high and their magnitude is about the same in all three directions. Neglecting contributions from one or two velocity components may lead to very large errors in the measurements of turbulence (see Tutu & Chevray 1975).

The dimensions of the probe which were finally adopted are shown in figure 4. Two photographs of the entire probe assembly are shown in figures 5(*a*) and 5(*b*).

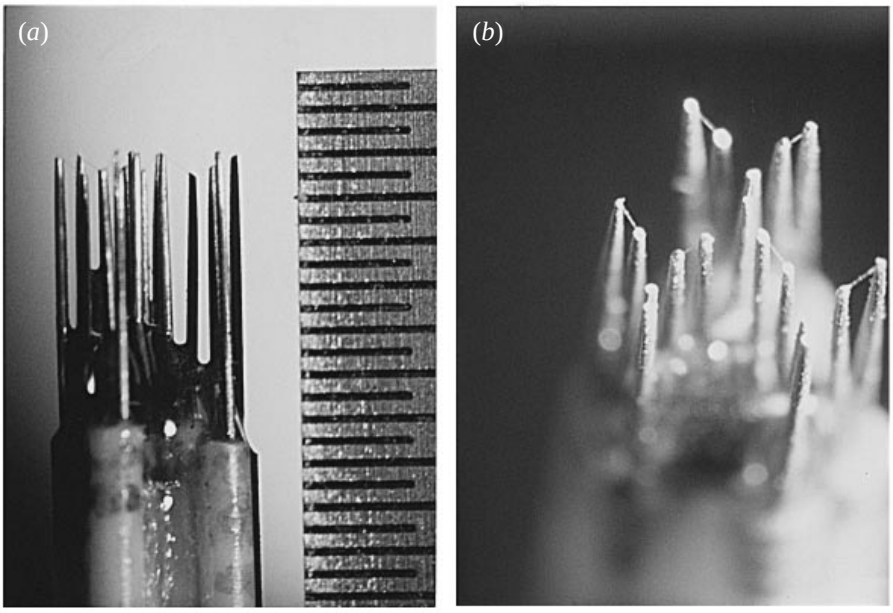

FIGURE 5(*a*, *b*). Photographs of the probe.

The probe required additional prongs to operate each sensor independently, which increased only minimally the blockage effects due to the six extra prongs by about 2.5% over that of Balint *et al*. Note that their probe uses 12 prongs by making one common to a set of three hot wires. The present probe, owing to mutually orthogonal orientation of wires, has a larger 'acceptance cone' when compared to the probe of Balint *et al*. (1991) which has one wire at 45° to the plane of other two orthogonal wires, and therefore the individual triple-wire probe is capable of measuring flows with larger turbulence intensities.

2.4. *Computations of velocity gradients*

In order to compute all three vorticity components, and the six distinct terms of the rate-of-strain tensor, six velocity derivatives need to be evaluated from the three velocity components measured at the three locations which are at the centres of each of the three triple wires. If these velocity vectors are known then the derivatives are evaluated as follows.

If the origin of a coordinate system is fixed at the centroid of the probe as shown in figure 6(*a*) and subscript 0 refers to the centroid of the probe and subscripts 1, 2 and 3 refer to quantities at the centres of the first, second and third triple wires respectively, then Taylor's expansion of the velocity component u at the centroid, neglecting higher-order derivative terms, yields

$$u_{1_1} = u_{1_0} + \left(\frac{\partial u_{1_0}}{\partial x_2}\right)_{x_1=x_2=x_3=0} \Delta x_{2_1} + \left(\frac{\partial u_{1_0}}{\partial x_3}\right)_{x_1=x_2=x_3=0} \Delta x_{3_1}, \tag{2.6}$$

$$u_{1_2} = u_{1_0} + \left(\frac{\partial u_{1_0}}{\partial x_2}\right)_{x_1=x_2=x_3=0} \Delta x_{2_2} + \left(\frac{\partial u_{1_0}}{\partial x_3}\right)_{x_1=x_2=x_3=0} \Delta x_{3_2}, \tag{2.7}$$

$$u_{1_3} = u_{1_0} + \left(\frac{\partial u_{1_0}}{\partial x_2}\right)_{x_1=x_2=x_3=0} \Delta x_{2_3} + \left(\frac{\partial u_{1_0}}{\partial x_3}\right)_{x_1=x_2=x_3=0} \Delta x_{3_3}, \tag{2.8}$$

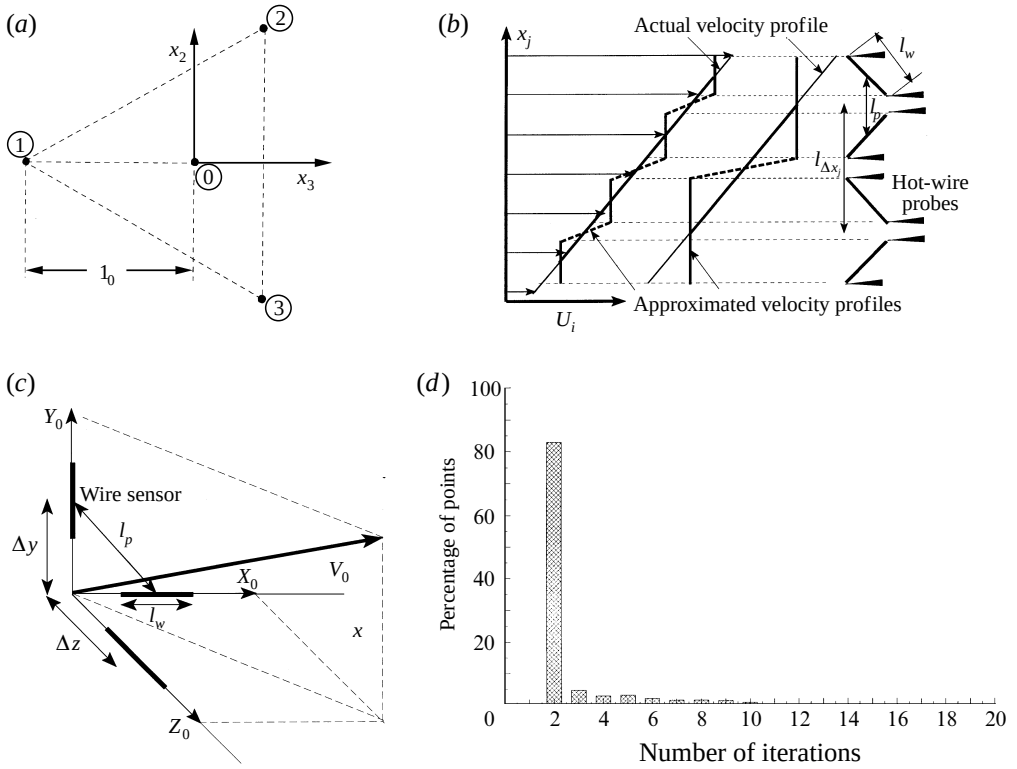

FIGURE 6. (*a*) Coordinate system for vorticity computations. (*b*) Velocity profile approximations. (*c*) Triple-wire sensor arrangement. (*d*) Distribution of the number of iterations required for convergence.

which form the following system of linear equations:

$$\begin{bmatrix} u_{1_1} \\ u_{1_2} \\ u_{1_3} \end{bmatrix} = \begin{bmatrix} 1 & \Delta x_{2_1} & \Delta x_{3_1} \\ 1 & \Delta x_{2_2} & \Delta x_{3_2} \\ 1 & \Delta x_{2_3} & \Delta x_{3_3} \end{bmatrix} \begin{bmatrix} u_{1_0} \\ \dfrac{\partial u_{1_0}}{\partial x_2} \\ \dfrac{\partial u_{1_0}}{\partial x_3} \end{bmatrix}. \tag{2.9}$$

All the elements of the matrix on the right-hand side can be expressed in terms of 1_0 shown in figure 6(*a*). The solution of (2.9) yields the longitudinal velocity u_{1_0} and the two spatial derivatives at the centroid of the probe.

Similar equations can be written for the normal component u_{2_0} and its partial derivatives and for the transverse component u_{3_0} and its partial derivatives. Now the streamwise derivatives are obtained by considering the momentum equation and neglecting pressure and viscous forces gradients, and the final expressions can be written as

$$\frac{\partial u_{1_0}}{\partial t} + u_{1_0}\frac{\partial u_{1_0}}{\partial x_1} + u_{2_0}\frac{\partial u_{1_0}}{\partial x_2} + u_{3_0}\frac{\partial u_{1_0}}{\partial x_3} = 0. \tag{2.10}$$

Thus

$$\frac{\partial u_{1_0}}{\partial x_1} = -\frac{1}{u_{1_0}}\left[\frac{\partial u_{1_0}}{\partial t} + u_{2_0}\frac{\partial u_{1_0}}{\partial x_2} + u_{3_0}\frac{\partial u_{1_0}}{\partial x_3}\right], \tag{2.11}$$

and similarly for the other gradients of the velocity components in the longitudinal direction:

$$\frac{\partial u_{2_0}}{\partial x_1} = -\frac{1}{u_{1_0}}\left[\frac{\partial u_{2_0}}{\partial t} + u_{2_0}\frac{\partial u_{2_0}}{\partial x_2} + u_{3_0}\frac{\partial u_{2_0}}{\partial x_3}\right], \tag{2.12}$$

$$\frac{\partial u_{3_0}}{\partial x_1} = -\frac{1}{u_{1_0}}\left[\frac{\partial u_{3_0}}{\partial t} + u_{2_0}\frac{\partial u_{3_0}}{\partial x_2} + u_{3_0}\frac{\partial u_{3_0}}{\partial x_3}\right], \tag{2.13}$$

which have been obtained by considering the momentum equations for the u_2 and u_3 components respectively.

Finally, the temporal derivatives in (2.11)–(2.13) can easily be evaluated by the difference of two successive velocity values and the sampling frequency f_s which subsequently allows computation of the streamwise derivatives.

Thus the determination of the longitudinal velocity derivatives is not based entirely on the original version of Taylor's hypothesis.

2.5. *The numerical schemes*

The individual velocity vector at the centre of each triple wire was computed by two different methods. In the first, the velocity is assumed to be uniform across each triple-wire probe and change from one triple sensor to the other. Thus the actual velocity profile, which to a first-order approximation in a Taylor's series expansion can be assumed to be linear, is simply segmented into two pieces (three areas in space) of uniform velocity each with a velocity jump across them.

In the second method the velocity across each triple sensor is not assumed to be uniform. Thus each the wires of one triple-wire probe sees different velocity vectors. However, the velocity along each individual wire is assumed to be uniform. In addition, the velocity gradient between two individual wires is assumed to be the same across the entire probe. Under these assumptions the linear velocity profile is segmented into multiple pieces, nine areas in total. Figure 6(*b*) shows schematically how the two different approximations affect the velocity distribution across two triple-wire sensors with only two wires shown on each sensor. It is expected that the second method is more accurate because the distance across each triple sensor, i.e. its size, is very close to the distances between the probes, and thus velocity gradients across each array cannot be ignored. This technique has been successfully used in the work of Balint *et al.* (1991) and it has been suggested by one of the referees.

As will be demonstrated later the two schemes yield results which, in general, are different. Statistical quantities containing cross-stream components of the velocity vector are affected most. An iterative scheme was used to improve the solutions obtained with each iteration. The velocity gradients determined by the finite difference described in the previous section were introduced to correct the velocity distribution across the entire probe.

In the orthogonal coordinate system x, y, z of the j probe ($j = 1, 2, 3$) the components of the velocity vector $\boldsymbol{V}_0$ at the origin are X_{oj}, Y_{oj}, Z_{oj}. The velocity components at the mid-point of each wire can be estimated to a first-order approximation in a Taylor's series expansion. Figure 6(*c*) shows schematically the relative dimensions and the wire sensors arrangement in one individual triple-wire probe. Thus the velocity components at the mid-point $(0, \Delta y, 0)$ of the wire at the oy-axis will be

$$X_{oj} + \frac{\partial X_{oj}}{\partial y}\Delta y, \quad Y_{oj} + \frac{\partial Y_{oj}}{\partial y}\Delta y, \quad Z_{oj} + \frac{\partial Z_{oj}}{\partial y}\Delta y.$$

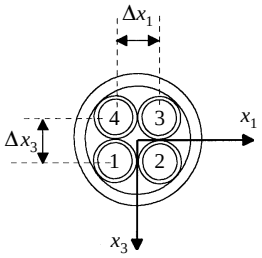

FIGURE 7. Vorticity flux module with pressure transducers.

A typical expression for the effective velocity $U_{eff\,ij}$ of the ith wire ($i = 1, 2, 3$) of the jth probe is as follows:

$$U^2_{eff\,ij} = H^2_{ij}\left(X_{oj} + \frac{\partial X_{oj}}{\partial y}\Delta y\right)^2 + K^2_{ij}\left(Y_{oj} + \frac{\partial Y_{oj}}{\partial y}\Delta y\right)^2 + M^2_{ij}\left(Z_{oj} + \frac{\partial Z_{oj}}{\partial y}\Delta y\right)^2. \quad (2.14)$$

The coefficients H_{ij}, K_{ij} and M_{ij} are determined through calibrations. Each of the gradients $\partial X_{oj}/\partial y$, $\partial Y_{oj}/\partial y$, $\partial Z_{oj}/\partial y$ can be expressed in terms of the velocity gradients in the coordinates of the centroid by simple transformations.

A system of three equations, one for each of the wires of the triple-sensor array, can be solved to provide estimates of the velocity vector (X_{oj}, Y_{oj}, Z_{oj}). The solution procedure is iterative. An initial guess of the velocity components is obtained by assuming that the increments $(\partial X_{oj}/\partial y)\,\Delta y$, $(\partial Y_{oj}/\partial y)\,\Delta y$, $(\partial Z_{oj}/\partial y)\,\Delta y$ are initially zero. Then the velocity vectors at the origin of each of the triple-wire probes can be obtained and subsequently the velocity gradients can be computed by the finite difference scheme described in §2.4. This leads to the first estimates of all partial velocity gradients which can be introduced into the system of equation (2.14) and a second estimate of velocity vectors and velocity gradients can be obtained. The iteration stops when the solutions converge. Usually a small number of iterations is needed. Figure 6(*d*) shows the distribution of the number of iterations needed to satisfy convergence criteria at $x_2^+ = 12.5$. The results of figure 6(*d*) indicate that about 82% of the samples processed converged after two iterations only. The data also show that the number of iterations needed never exceeded 10 for any of the samples considered.

2.6. *Vorticity flux modules*

In the present work the following definition has been used for vorticity flux $\boldsymbol{\sigma}_w$ at the wall beneath a boundary layer flow:

$$\boldsymbol{\sigma}_w = \nu\left[\left(\frac{\partial \omega_1}{\partial x_2}\right)_w \boldsymbol{i} + \left(\frac{\partial \omega_3}{\partial x_2}\right)_w \boldsymbol{k}\right], \quad (2.15)$$

where $\boldsymbol{i}$, $\boldsymbol{j}$ and $\boldsymbol{k}$ are unit vectors in the x_1, x_2 and x_3 directions. Evaluation of the Navier–Stokes equations at the wall (see (1.8)) indicates that time-dependent measurements of the two pressure gradients $(\partial p/\partial x_1)_w$ and $(\partial p/\partial x_3)_w$ can provide a good estimate of vorticity flux.

Four high-frequency-response and high-sensitivity, ultra-miniature pressure transducers supplied by ENTRAN were used to measure simultaneously the two pressure gradients. The sensing area of each of the transducers was 0.5 mm in diameter. This makes the resolution better than that used in the study by Andreopoulos & Agui (1996) where Kulite pressure transducers of slightly greater size were used. The four pressure transducers were epoxied together to form a module as shown in figure 7. The

separation distance between them was 1.4 mm. This module was then placed inside a bolt with one edge machined flat so that the bolt could be securely threaded in place in the boundary layer wall. This module will henceforth be referred to as Entran module for simplicity.

The pressure gradients were computed by the following finite difference scheme:

$$\left(\frac{\partial \omega_3}{\partial x_2}\right)_w = -\frac{1}{\mu}\left(\frac{\partial p}{\partial x_1}\right)_w \approx -\frac{1}{\mu}\left[\frac{p_4(x_1+\Delta x_1)-p_1(x_1)}{\Delta x_1}\right] \tag{2.16}$$

and

$$\left(\frac{\partial \omega_1}{\partial x_2}\right)_w = \frac{1}{\mu}\left(\frac{\partial p}{\partial x_3}\right)_w \approx \frac{1}{\mu}\left[\frac{p_2(x_3+\Delta x_3)-p_1(x_3)}{\Delta x_3}\right]. \tag{2.17}$$

All four Entran pressure transducers were calibrated simultaneously using a calibrator made by Thermo Systems Inc. model 1125 which provided the required range of pressures. The voltage outputs of the transducers were then recorded against the seven different pressures measured by the micro-manometer with a resolution of 0.002 54 mm of water. The calibrations of Entrans demonstrated that the response of each transducer was linear as expected.

2.7. *Instrumentation*

The hot-wire sensors of the vorticity probe were operated by 9-channel constant-temperature anemometers model 56C01/C17 manufactured by Dantec Electronics Inc.

Two analog filters each with 8 input channels and an integrated programmable gain amplifier (model Filter 488/8) made by I0tech were used to low-pass filter the anemometer output voltage signals before digitization.

Data acquisition hardware consisted mainly of two 16-bit (1 part in 60 000)-resolution high-performance analog and digital interfaces model ADC488SA manufactured by I0tech. The board has an a/d conversion rate of 100 000 samples per s. On board simultaneous sample and hold circuitry allowed simultaneous acquisition of all channels of data. The acquisition time was less than 1.8 μs with under 0.25 ns aperture uncertainty between channel. Four software programmable bipolar input ranges enabled flexible resolution of the signals to be obtained.

Yaw and pitch rotations of the probe were required for determining its pitch and yaw response. They were computer controlled by a PC-Motion Interface board supplied by Rogers Lab model ESH-80 and a driver board model ESH 083 which was installed in IBM micromputer. The stepper motor step size was 1.8° and with a setting of five microsteps per full step provided more than adequate resolution of yaw and pitch angle measurements.

2.8. *Calibration of the probe and data collection*

In-situ calibrations of the probe were carried out in the inviscid free stream of the flow, once prior to the data acquisition session and again at the end of the experiment. The probe was placed in the middle of the working section by using a 3 ft slender arm which was a part of a computer-controlled three-dimensional traversing mechanism. Extensive yaw and pitch response measurements for each of the sensors were then obtained by elegant coordination of data acquisition on one microcomputer while performing required yaw or pitch rotations through motion control hardware interfaced to another microcomputer. The range of angles covered was $-30°$ to $+30°$, in steps of 5° for both yaw and pitch for five different free-stream velocities.

Data were collected simultaneously on all nine wires with a sampling rate of 5 kHz per channel for total duration of about 82 s at each point. This was adequate according

to the criteria prescribed by Klewicki & Falco (1990) for statistical convergence of ensemble quantities. Actual tests of convergence of statistical quantities up to the fourth moments also indicated that the total sampling time of 82 s was adequate. The signals were low-pass filtered at 1 kHz before digitization.

3. Probe resolution considerations

The wire length of each sensor, separation distance between each sensor and finally spacing of each of the three triple wires were the most important dimensions to be optimized very carefully in the final configuration of the probe for good spatial resolution. Although these dimensions are apparently independent, they could not be varied independently to improve one performance characteristic without introducing an adverse effect on an other. Wire length for example should be kept as small as possible to resolve finer scales in the flow but too small an aspect ratio (length/diameter) of the sensor increases the heat conduction effects and therefore is likely to result in erroneous data and inaccurate flow quantities. The sensor separation should be as small as possible to satisfy the assumption that velocity is uniform across the measuring area, but then this has to be balanced by the thermal wake effects/cross-talk between the wires. Further, this separation should be less than the Kolmogorov length to capture the smallest structural scales but then this separation should also be greater than the Kolmogorov length according to Wyngaard (1969) so that the gradients are measurable. Both conditions in reality are impossible to satisfy simultaneously. The third dimension of spacing of each of the three triple wires should be short yet finite so that the velocity gradients to be evaluated do not disappear. This spacing, if too small, would result in an unacceptably low signal-to-noise ratio as pointed out by George (1993, personal communication), Antonia, Zhu & Kim (1993) and Wallace & Foss (1995).

The estimates of flow scale resolutions expressed in Kolmogorov microscale units are given in table 2(*a*). Table 2(*b*) contains similar estimates expressed in viscous units. The Kolmogorov length scale $\eta = (\nu^3/\epsilon)^{1/4}$ indicates the smallest turbulent structure encountered in the flow. Determining η, however, requires a good estimate of the turbulent kinetic energy dissipation rate ϵ, which is very difficult to measure directly in the laboratory. Previous studies obtained the value of ϵ by making assumptions to reduce some of the terms in the expression for the dissipation of energy per unit time per unit mass:

$$\epsilon = 2\nu\overline{s_{ij}\,s_{ij}} = \nu\left[\overline{\left(\frac{\partial u_i}{\partial x_j}\frac{\partial u_i}{\partial x_j}\right)} + \overline{\left(\frac{\partial u_i}{\partial x_j}\frac{\partial u_j}{\partial x_i}\right)}\right]. \tag{3.1}$$

The first term on the right-hand side represents contributions from the homogeneous part of the flow while the second one represents contribution from the inhomogeneous part of the flow.

The estimates usually provided for spatial resolution, particularly those based on indirect methods, may be very misleading. An experiment with poor spatial resolution will result in the attenuation of all measured turbulence quantities including the turbulence produced term $\overline{u_i\,u_j}\,\partial\overline{U_i}/\partial x_j$. This eventually results in lower estimates of the dissipation rate when ϵ is determined by difference from the other terms of the transport equations of turbulent kinetic energy and therefore will indicate erroneously high resolution.

The dissipation rate ϵ in the present work has been computed from the measured values of the terms of the velocity gradient tensor by six different methods, all listed in table 1(*a*), which resulted in slightly different wire η_w and probe resolutions η_p and

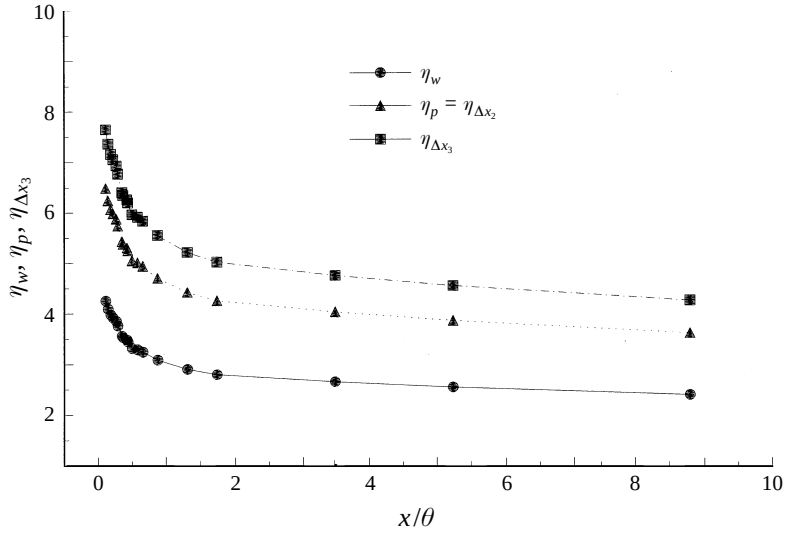

FIGURE 8. Distribution of wire size η_w, individual probe size η_p and probe separation in the x_2-direction $\eta_{\Delta x_3}$, non-dimensionalized by the Kolmogorov length.

(*a*)	Probe resolution		
Method of computation	η_w	η_p / $\eta_{\Delta x_2}$	$\eta_{\Delta x_3}$
1. All terms in dissipation (total dissipation) $\epsilon = 2\nu\overline{s_{ij}s_{ij}} = \nu\left[\overline{\left(\frac{\partial u_i}{\partial x_j}\frac{\partial u_i}{\partial x_j}\right)} + \overline{\left(\frac{\partial u_i}{\partial x_j}\frac{\partial u_j}{\partial x_i}\right)}\right]$	4	6	7
2. Homogeneous dissipation $\epsilon \approx \nu\overline{\left(\frac{\partial u_i}{\partial x_j}\frac{\partial u_i}{\partial x_j}\right)}$	3	5	6
3. Enstrophy-based dissipation $\epsilon \approx \nu\overline{\omega_k\omega_k}$	3	5	6
4. Isotropy $\epsilon = 15\nu\overline{(\partial u/\partial x)^2}$	3	5	6
5. Axisymmetric isotropy (George & Hussein 1991)	3	5	6
6. Production = dissipation	2	4	5
ENTRAN pressure transducers	—	1.5–2.6	3–5.6

(*b*)	Wire length	Probe size/wire separation	Probe separation
Hot-wire probe	$l_w = 0.8$ mm; $l_w^+ = 6$	$l_p = 1.2$ (mm); $l_p^+ = 10$ $l_{\Delta x_2} = 1.2$ (*mm*); $l_{\Delta x_2}^+ = 10$	$l_{\Delta x_3} = 1.44$ (mm); $l_{\Delta x_3}^+ = 12$
Entran pressure transducers	—	$d = 0.5$ (mm); $d^+ = 4.0$	$\Delta d = 1.4$ (mm); $\Delta d^+ = 12$

TABLE 2. (*a*) Probe resolution in Kolmogorov microscale units η at $x_2^+ = 12.5$, (*b*) probe resolution in viscous units.

probe separation distance $\eta_{\Delta x}$. Although the assumptions involved in each method may not be valid at $x_2^+ = 12.5$, which is the closest to the wall measurement location, the resulting resolution is comparable to that of Balint *et al.* (1991) and gets better as the wall normal distance increases. It should be noted that in the work of Antonia *et al.* (1993) the dissipation rate has been estimated under flow homogeneity assumptions which according to the data of table 2(*a*) is about 10% less than that based on all terms of equation (3.1). Figure 8 shows the distribution of the non-dimensional size of the

wire η_w, the individual triple-wire-probe resolutions η_p and the probe separation distance ($\eta_{\Delta x_2}, \eta_{\Delta x_3}$). For $x_2/\theta > 1.0$ all resolutions improve by approximately a factor of 1.5.

The present probe, however, is not immune to spatial attenuation problems caused mainly by the finite spacing of the individual triple-hot-wire probes. The recent work of E. Ewing & W. K. George (1993, personal communication) where estimates are provided of attenuation of the vorticity measurements by probes similar to the present one, suggests that the present measurements of r.m.s. vorticity components may be attenuated by about 8–15% at $x_2^+ = 12.5$. Wyngaard (1969) and Klewicki & Falco (1990) claimed that for adequate resolution it is necessary that the probe size should not exceed three Kolmogorov scales. These authors as well Antonia *et al*. (1993) used a probe consisting of two parallel wires in their effort to quantify the attenuation of measured fluctuations. However, the estimates of attenuation provided by these authors may be questionable because the use of parallel wires precludes using a three-dimensional response of the effective cooling velocity in King's law. Ignoring contributions from the lateral and normal components can cause substantial errors in the measurements of turbulence.

Although the assumptions made in such theoretical or experimental considerations of the attenuation problem are not always satisfied in each particular flow, they are useful in providing an estimate of the uncertainties involved in this type of measurement. It should be noted that the errors involved in calculating normal and spanwise components of vorticity were minimized by more accurate estimates of the velocity gradients in the streamwise direction which are computed using all the terms in Taylor's 'frozen flow' expression (see equations: 2.11–2.13). In addition, as will be shown later, in the limit of vanishing separation between the two probes Δx_j, the r.m.s. of the fluctuations of one velocity gradient $\partial u_i/\partial x_j$ is given by

$$\lim_{\Delta x_j \to 0} \overline{\left[\frac{\Delta u_i}{\Delta x_j}\right]^2} = \frac{\overline{u_i^2}}{\lambda_{ij}^2},$$

where λ_{ij} is Taylor's microscale. Thus λ_{ij} maybe more appropriate than Kolmogorov's viscous length for scaling vorticity statistics.

Determining the spatial resolution of the pressure transducers at the wall is more difficult because dissipation at $x_2^+ = 0$ has never been measured. However, if the available estimate of ϵ at $x_2^+ = 12.5$ is used to extrapolate the distribution of ϵ down to the wall according to the recent work of Jovanović, Ye & Durst (1995) the size of the pressure transducers appears to be between $\eta_{\mathrm{d}} = 1.5$ and 2.6 Kologorov scales.

The separation distance between the two pressure transducers in the vorticity flux module appears to be between $\eta_{\Delta p} = 3$ and 5.6. A detailed analysis of the response characteristics of the vorticity flux probe to turbulent flows with scales smaller than its size is described by Andreopoulos & Agui (1996). This analysis predicts that the attenuation of vorticity flux for scales smaller than the probe size is more pronounced than that of pressure. Correction procedures according to the theory may provide an estimate of the power spectral density in a frequency range over which the probe spatial resolution effects are important. However, no corrections have been applied to the present data because the spatial resolution of the vorticity flux probe is better than that of the hot-wire probe for the measurements of velocity gradients.

4. Physics of the structure function

When the differential $\Delta Q = Q(r+\Delta r) - Q(r)$ of a quantity $Q(r)$ is required to be estimated at a position r, two measurements of the quantity Q at close locations r, $r+\Delta r$, are usually attempted. In the present case Q maybe either the velocity vector or wall pressure. If we consider the average $\overline{\Delta Q^2}$, i.e. the structure function of Q, then

$$\overline{\Delta Q^2} = \overline{[Q(r+\Delta r) - Q(r)]^2} = \overline{Q^2(r)}\,[(1-\rho)^2 + 2\rho(1-R_{\Delta r})],$$

where ρ is the ratio

$$\rho^2 = \frac{\overline{Q^2(r+\Delta r)}}{\overline{Q^2(r)}}$$

and $R_{\Delta r}$ is the cross-correlation coefficient

$$R_{\Delta r} = R_{r,r+\Delta r} = \frac{\overline{Q(r)Q(r-\Delta r)}}{[\overline{Q^2(r)}]^{1/2}[\overline{Q^2(r+\Delta r)}]^{1/2}}.$$

Thus for the r.m.s. we can obtain

$$\left[\left(\frac{\overline{\Delta Q^2}}{\Delta r^2}\right)\right]^{1/2} = \frac{[\overline{Q^2(r)}]^{1/2}}{\Delta r}[(1-\rho)^2 + 2\rho(1-R_{\Delta r})]^{1/2}. \tag{4.1}$$

This indicates that the r.m.s. value of the quantity $\Delta Q/\Delta r$ depends on, among other quantities, $(1-\rho)$ and $(1-R_{\Delta r})$. The first quantity is a measure of the inhomogeneity of the r.m.s. while the second one indicates the uncorrelated part between the two signals at r and $r+\Delta r$. It can be argued that for small separations Δr, $\rho \approx 1$. For instance, if Δr is oriented in the longitudinal direction of the present flow of a two-dimensional flat-plate boundary layer, there is very little change of the r.m.s. of any quantity with Δx_1. Thus $\rho \approx 1$.

For differential changes in the Δx_2 direction normal to the wall there is minor change in r.m.s. within a distance $\Delta x_2^+ \approx 16$ very close to the wall, inside the buffer region. Even in this case $\rho \approx 0.95$ or higher and $R_{\Delta r}$ is about 0.8. Thus the ratio of the two parts of (4.1) $2\rho(1-R_{\Delta r})/(1-\rho)^2$ is about 150. Therefore it is very reasonable to assume that $\rho \approx 1$ or that $2\rho(1-R_{\Delta r}) \gg (1-\rho)^2$ which yields

$$\left[\frac{\overline{\Delta Q^2}}{\Delta r^2}\right]^{1/2} = \frac{[\overline{Q^2(r)}]^{1/2}}{\Delta r}[2\rho(1-R_{\Delta r})]^{1/2}. \tag{4.2}$$

This indicates that most contributions to $\Delta Q/\Delta r$ come from the *uncorrelated* part of the two signals. Thus there are no vorticity flux or velocity gradients between two perfectly correlated pressure or velocity signals respectively. It is known that the existence of small scales in the flow decreases $R_{\Delta r}$. On the other hand two sinusoidal signals with a phase shift will also result in correlation coefficient $R_{\Delta r}$ lower than 1. Thus contributions to $\Delta Q/\Delta r$ may come from the high-wavenumber part of the spectrum or out-of-phase large eddies in the low-wavenumber part. Figure 9 shows the power spectral density of the turbulent kinetic energy $\frac{1}{2}u_i u_i$ and enstrophy $\frac{1}{2}\omega_k \omega_k$ weighted by the wavenumber k_1, as measured in the present investigation. The maxima of the spectra occur at approximately $k_1\delta = 20$ and $k_1\delta = 50$ respectively. This shift of maximum spectral energy towards higher wavenumber clearly suggests that enstrophy fluctuations are mainly a result of a greater proportion of contributions by the smaller scales whereas the kinetic energy in the flow comes from the larger eddies. These results also show that there are contributions from the low-wavenumber part of the spectrum of enstrophy.

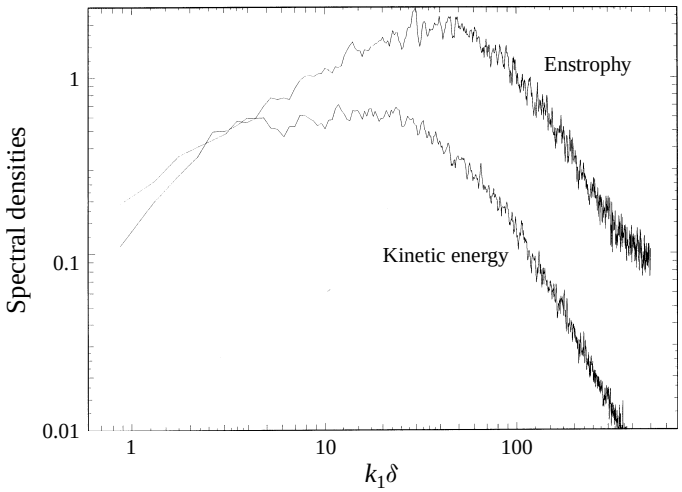

FIGURE 9. Spectral densities of enstrophy and kinetic energy weighted by the wavenumber at $x_2^+ = 12.5$.

The limit of equation (4.1) when Δr approaches zero is also of interest in the present considerations. In this case $R_{\Delta r} \approx 1$, $\rho \approx 1$ and thus the limit appears to become indefinite. After applying the L'Hospital rule, and considering that when Δr approaches zero, $R_{\Delta r} \approx 1$, $\rho \approx 1$, $\partial R/\partial \Delta r \approx 0$ the following relation can be obtained:

$$\lim_{\Delta r \to 0} \overline{\left[\frac{\Delta Q}{\Delta r}\right]^2} \approx -\overline{Q^2}\left[\frac{\partial^2 R}{\partial(\Delta r)^2} + \left[\frac{\partial \rho}{\partial(\Delta r)}\right]^2\right],$$

where $\partial^2 R/\partial(\Delta r)^2$ is the curvature of the cross-correlation function R at the origin. Thus a Taylor microscale λ can be defined as

$$\left[\frac{\partial^2 R}{\partial(\Delta r)^2}\right]_{\Delta r \to 0} = -\frac{1}{\lambda^2}$$

and therefore

$$\overline{\left[\frac{\Delta Q}{\Delta r}\right]^2}_{\Delta r \to 0} = \frac{\overline{Q(r)^2}}{\lambda^2}\left[1 + \lambda^2\left[\frac{\partial \rho}{\partial \Delta r}\right]^2\right]. \tag{4.3}$$

It appears that this limit determines the highest attainable value under an ideal probe resolution. The term $(\partial\rho/\partial\Delta r)^2/(1/\lambda^2)$ depends on the location r, direction Δr and the quantity Q under consideration. In general this ratio is smaller than one and in most cases it can be neglected. For instance in the present flow and for longitudinal pressure and velocity gradients this ratio is of the order of 10^{-2} to 10^{-3} and it can be neglected. For velocity gradients in the normal to the wall direction Δx_2 this ratio is of the order of 10^{-2} for the longitudinal velocity and 10^{-1} for the normal velocity gradient. In the latter case considerable errors will be introduced if the contribution of this term is neglected.

In cases where this term can be omitted than (4.3) becomes

$$\overline{\left[\frac{\Delta Q}{(\Delta r)}\right]^2}_{\Delta r \to 0} = \frac{\overline{Q(r)^2}}{\lambda^2}. \tag{4.4}$$

This relation is also the same as considered as an order of magnitude value for vorticity fluctuations by Tennekes & Lumley (1972). In addition, (4.4) suggests that, most probably, λ plays a role in scaling the r.m.s. of vorticity or vorticity flux.

An attempt has been made to verify (4.3) with experimental data for the case of longitudinal wall pressure and velocity gradients by computing Taylor's microscales λ_{p1} and λ_{11} from autocorrelations of pressure and longitudinal velocity fluctuations respectively, after invoking Taylor's hypothesis. The values obtained were $\lambda_{p1} \approx 3.1$ mm and $\lambda_{11} \approx 3.5$ mm. Thus the right-hand side of (4.3) can be estimated reasonably well and compared to the measured values of the r.m.s. $(\partial p/\partial x_1)'$ at $Re_\theta = 2790$ and $(\partial u_1/\partial x_1)'$ at the closest to the wall location, $y/\delta = 0.0107$, which are shown in figures 10 and 24(*a*) respectively. The ratio of the measured r.m.s. to that obtained from (4.3) was found to be 0.95 for the longitudinal pressure gradient and 0.9 for the longitudinal velocity gradient. It is therefore plausible to assume that, within the uncertainty in estimating λ_{p1} and λ_{11}, relation (4.3) is valid in general. The result of this rather limited verification also indicates that there is not much of the spectral content of scales of pressure or velocity gradient fluctuations unresolved in the longitudinal direction.

5. Results and discussion

The results of the present investigation are illustrated by adopting the scaling factors commonly used by many investigators for comparison which, it should be noted, implies that such scaling would collapse all quantities of turbulence onto a single curve. This notion of the existence of such a universal scaling is neither well established nor well investigated. An experimental attempt by Wei & Willmarth (1989) in turbulent channel flows for a range of Reynolds numbers tried to address this issue. They concluded from their results that (*a*) scaling by inner variables of turbulent quantities, are, at least in the near-wall region, Reynolds-number dependent and (*b*) whereas the power spectra of axial velocity were found to scale with these inner variables, the power spectra of the normal component as well as that of Reynolds shear stress did not.

Further evidence of this strong Reynolds-number dependence in the near-wall region is shown in figure 10 where the r.m.s. of vorticity flux fluctuations at the wall is plotted against Re_θ. All the data were obtained in the same facility with exception the estimates of Lu & Smith (1988) who measured fluctuations of $\partial^2 u_1/\partial x_2^2$ above the wall and extrapolated these values by orthogonal decomposition to the wall. The measurements which were carried out in the present wind tunnel were obtained by three different methods using two different pressure transducers as described by Andreopoulos & Agui (1996). In the work of Andreopoulos & Agui, Kulite pressure transducers were used while in the present investigation Entran pressure transducers were employed because of better spatial resolution. In order to verify the measurements of Andreopoulos & Agui and test the performance of these pressure transducers several experiments at different Re_θ were carried out. The data obtained are directly compared to the previous ones in figure 10. As can be seen from this figure the agreement between the two data sets is very good. The present measurements were also extended to lower and higher Re_θ than before.

The spatial resolution of these measurements also varies with Re_θ. The size of the probe in viscous scale units is four at the lowest Re_θ and reaches a value of 18 at the highest Re_θ. It should be noted that the work of Schewe (1983) established that a transducer size of 19 is adequate for good spatial resolution. Thus the present data, although not quite immune from the spatial resolution problem at high Re_θ, show a genuine strong Re_θ dependence.

The recent view of Gad-el-Hak & Banyopadhyay (1994) indicated that Reynolds number effects are more evident in higher-order statistics of velocity fluctuations,

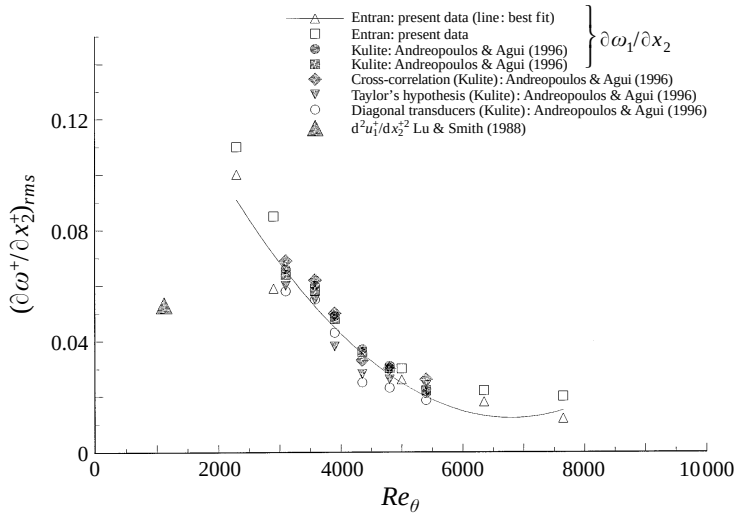

FIGURE 10. R.m.s. of vorticity flux fluctuations at various Reynolds numbers.

	Re_θ or $Re_{d/s}$ or Re_δ	U_∞ (m s^{-1})	δ (mm)	θ (mm)	u_τ (m s^{-1})	Flow type
Present experiment	2790	3.200	140.00	13.60	0.13	Boundary layer
Balint *et al.* (1991)	2685	3.510	125.00	12.10	0.14	Boundary layer, hot wire
Klewicki (1989)	2870	1.750	205.00	24.50	0.07	Boundary layer
Spalart (1988)	1410	—	—	—	—	Boundary layer DNS
Kastrinakis & Eckelmann (1983)	12600	2.000	—	—	0.09	Channel, hot film
Wei & Willmarth (1989)	22776	2.330	—	—	0.07	Channel LDA
Kim *et al.* (1987)	3300	0.639	—	7.00	0.04	Channel DNS
Klebanoff (1954)	78000	—	—	—	—	Boundary layer
Andreopoulos & Agui (1994)	2790	3.200	140.00	13.60	0.13	Boundary layer LAVOR
Andreopoulos *et al.* (1984)	3624	6.33	73.90	8.60	0.25	Boundary layer
Meinhart & Adrian (1995)	930	1.60	75.70	9.10	0.074	Boundary layer,
	2270 (case 2)	3.79	82.80	9.84	0.158	PIV
	6845 (case 3)	10.88	78.03	9.71	0.400	
Lemonis (1995)	6450	6.400	155.00	15.60	0.23	Boundary layer, hot wire
Rajagopalan & Antonia (1993)	1450	2.400	83.00	—	0.10	Boundary layer, hot wire
Bruns *et al.* (1992)	2600–16100	—	—	—	—	Boundary layer, hot wire

TABLE 3. Principal parameters of the existing datasets used in the comparison.

particularly in skewness and flatness. However, the present data on vorticity flux show the strongest Re_θ dependence of any turbulence quantity ever considered. This behaviour may also suggest a possible breakdown of the law of the wall which is similar to the cases examined in the work of Bradshaw & Huang (1995) in which flows were considered where the law of the wall has failed. The work of Andreopoulos & Agui

demonstrated that vorticity flux data show the least Re_θ dependence when scaled with θ and u_τ. According to Bradshaw (1996, personal communication) the anomalous behaviour of the surface gradients may be indicative of Townsend's inactive motion, i.e. outer layer fluctuations which perturbing the flow near the wall in a 'scrubbing' action similar to that suggested by Kasagi *et al*. (1995).

Lastly the boundary layer flows on a flat plate, in a pipe, or in a channel have different characteristics especially at low Reynolds number. The conclusions drawn therefore need to be viewed in the light of the fact that the scaling laws for these flows are yet to be established fully. One type of scaling for all quantities in a particular flow is very unlikely to be entirely satisfactory everywhere in the flow field.

The results of the present investigation are compared with existing data sets by other researchers in table 3.

5.1. *Probe evaluation*

The performance of the present probe and techniques used can be evaluated by comparing the Reynolds shear stress $\rho u_1 u_2$ measured by each of the three sensors arrays. This quantity is rather difficult to measure with adequate accuracy because it is very sensitive to small changes in the experimental conditions and parameters associated with the probe geometry. A small misalignment, for instance, of the probe orientation by no more than 2° can introduce substantial errors in the measured shear stress.

The performance of each of the individual triple-hot-wire probes is demonstrated in figure 11(*a*) where the shear stress $\rho u_1 u_2$ normalized by the mean wall shear stress ρu_τ^2 is plotted against the distance from the wall x_2^+ in inner layer scaling. Three different profiles are shown together with the resultant profile calculated at the centroid of the probe. The lines are best fits through the individual data. It can be seen that the deviation of each of these profiles from each other and from that at the centroid is no more than 8 % which is within the accuracy of the shear stress measurements. The good agreement among the data also indicates that interference effects between the individual sensors and blockage effects in general are relatively minor.

Another indicator of minimal blockage and interference effects is the low values of the stress $\rho u_2 u_3$ measured by the present probe. Strong blockage effects would cause the streamlines to bend around the probe and thus generate substantial lateral shear stress $\rho u_2 u_3$. The fact that the $u_2 u_3^+$ stress never exceeds the value of 0.07 in the near-wall region ($x_2^+ < 50$) and is practically zero everywhere else suggests that blockage or interference effects are very limited.

Also on figure 11(*a*) the values of $u_1 u_2^+$ obtained by the first method of simply segmented velocity profiles without accounting for the velocity gradient across the individual triple wire sensors are shown. It is evident that these data are about 0.10, on average, greater in the near-wall region than those obtained by the second method of multiply segmented velocity profiles. The difference in the results between these two methods diminishes as the distance from the wall increases.

The internal consistency of the data is also demonstrated in figure 11(*b*) where the turbulent kinetic energy $\frac{1}{2}u_i u_i$ across the boundary layer is plotted against x_2^+ as measured by each of the three individual triple-wire sensors. It can be seen that the three different profiles agree with each other quite well.

5.2. *Reynolds shear stress*

The profile of Reynolds shear stress $-\rho u_1 u_2$ across the boundary layer is shown in figure 11(*c*). The r.m.s. values of the shear stress are normalized by the mean shear stress ρu_τ^2 and the wall-normal distance by the other variable δ. The present data agree

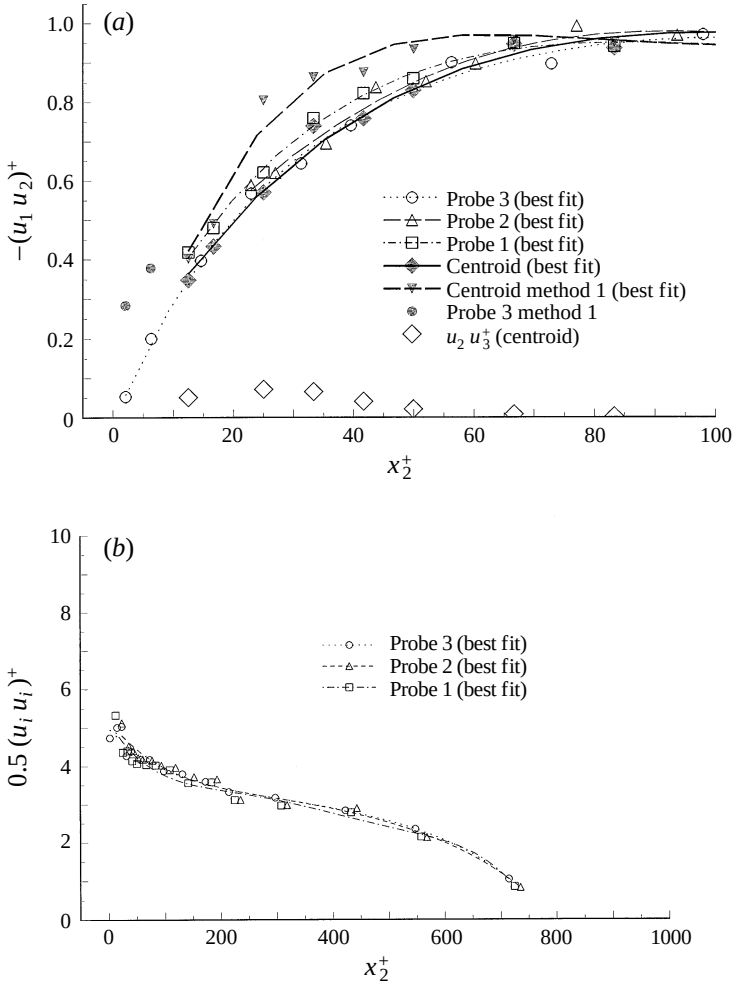

FIGURE 11(*a*, *b*). For caption see facing page.

quite well when compared with that of Balint, Vukoslavčević & Wallace (1991), Spalart (1988) and Klebanoff (1954). The near-wall comparison of the turbulent shear stress shown in figure 11(*d*) also reveals good agreement with the values measured by Balint *et al.* (1991). But the values of Spalart (1988) are higher than both sets of experimental results. When compared with the low-Reynolds-number data of Kim, Moin & Moser (1987), their data appear to be higher than the present results in the buffer region but lower in the region $x_2^+ > 35$. The two data points for $x_2^+ < 12.5$ shown in this figure are from the third triple-wire probe which is closer to the wall since it is below the centroid of the probe. It is important to note that the measurement of the turbulent shear stress is one of the most difficult and critical tasks to carry out because of the relatively large uncertainties involved. As a result, laboratory measured values of the Reynolds shear stress in the near-wall region of a turbulent boundary layer flows show no consistent trend. On the contrary, rather significant scatter of the data is observed regardless of the scaling parameter. The present values are found to be in good agreement with those of Balint *et al.* (1991) in the near-wall zone as well as in the strong-shear zone. Both experimental datasets, however, are considerably lower in the near-wall region than the DNS data of Spalart (1988) or Kim *et al.* (1987) carried out a lower Re_θ.

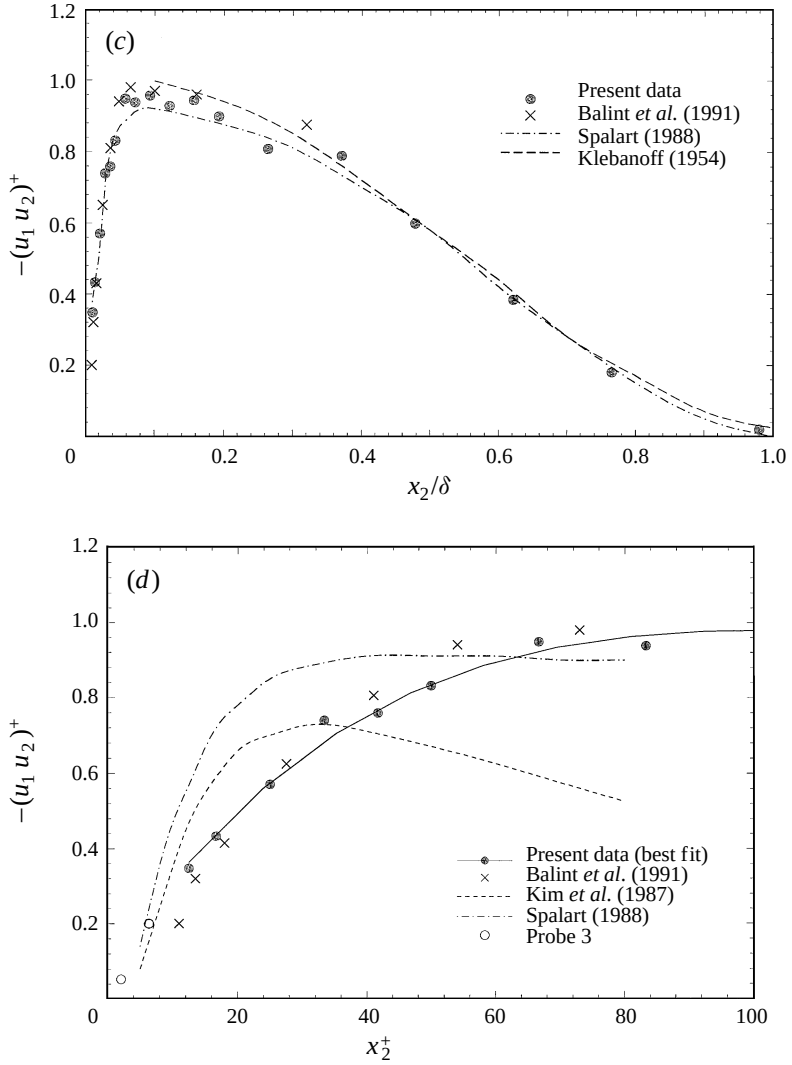

FIGURE 11. (*a*) Normalized shear stress measured by the three individual triple wire sensors. (*b*) Normalized turbulent kinetic energy measured by the three individual triple wire sensors. (*c*) Normalized shear stress $u_1 u_2$ across the boundary layer. (*d*) Normalized shear stress $u_1 u_2$ in the near-wall region.

5.3. *Velocity component statistics*

Figures 12(*a*), 13(*a*) and 14(*a*) show the r.m.s. values of axial, normal and spanwise velocity components normalized by the friction velocity u_τ plotted against the distance normalized by the outer scale δ. For $x_2/\delta > 0.1$ the axial velocity fluctuations agree well with those of Balint *et al.* (1991) but they are lower in the near-wall region $x_2/\delta < 0.1$. The data of Balint *et al.* follow closely the DNS data of Spalart for $Re_\theta = 1450$. The data of Meinhart & Adrian (1995) appear to be slightly higher in the outer-layer region than the rest of the data. The present data show reasonably good agreement with the data of Klebanoff (1954) for $x_2/\delta > 0.04$. Near the wall, however, Klebanoff's data are considerably higher than the present ones. They reach a value of three while the present data indicate a maximum value of 2.33. Although these data have been obtained at Re_θ

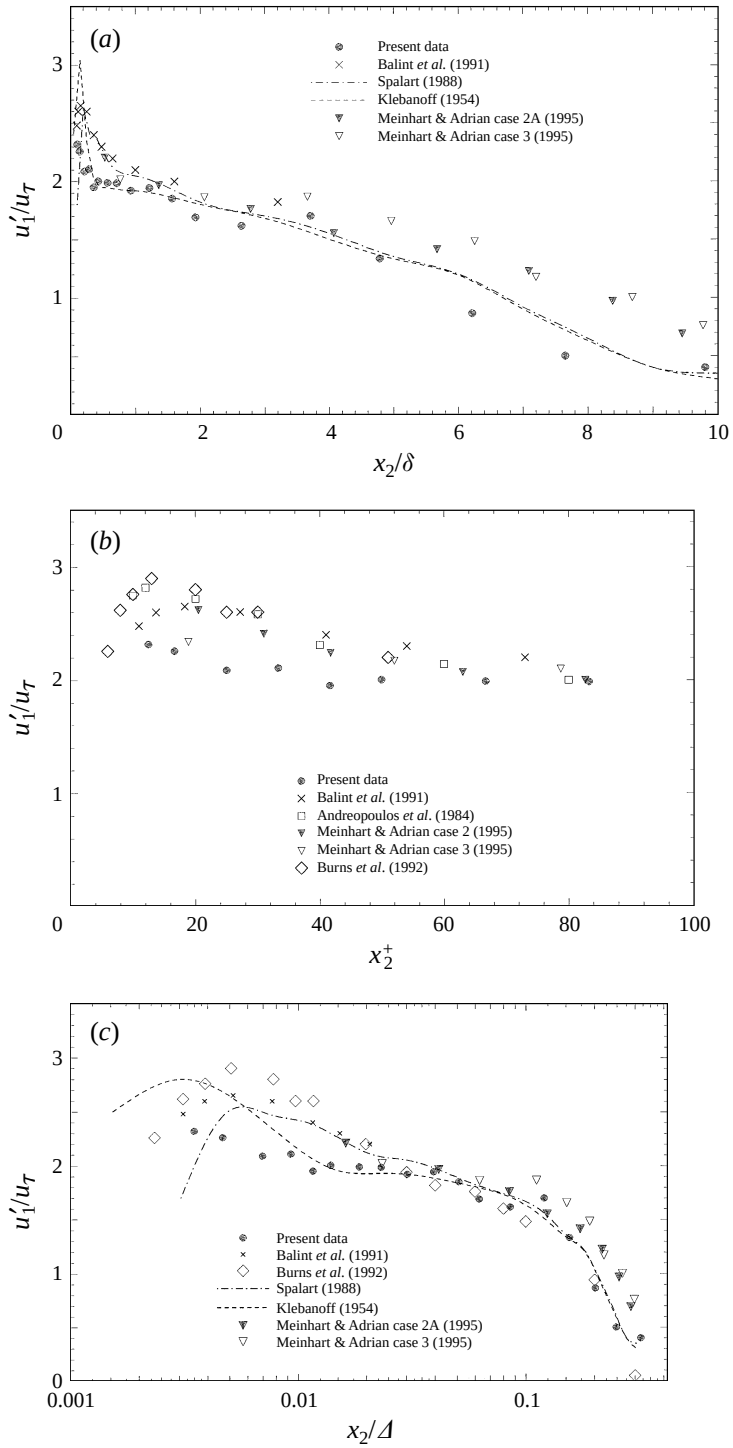

FIGURE 12. (*a*) Measured r.m.s. of axial velocity fluctuations normalized by u_τ and δ. (*b*) Near-wall distribution of measured r.m.s. of axial velocity fluctuations in inner layer scaling. (*c*) Measured r.m.s. of longitudinal velocity fluctuations in outer-layer scaling with u_τ and Rotta's thickness Δ.

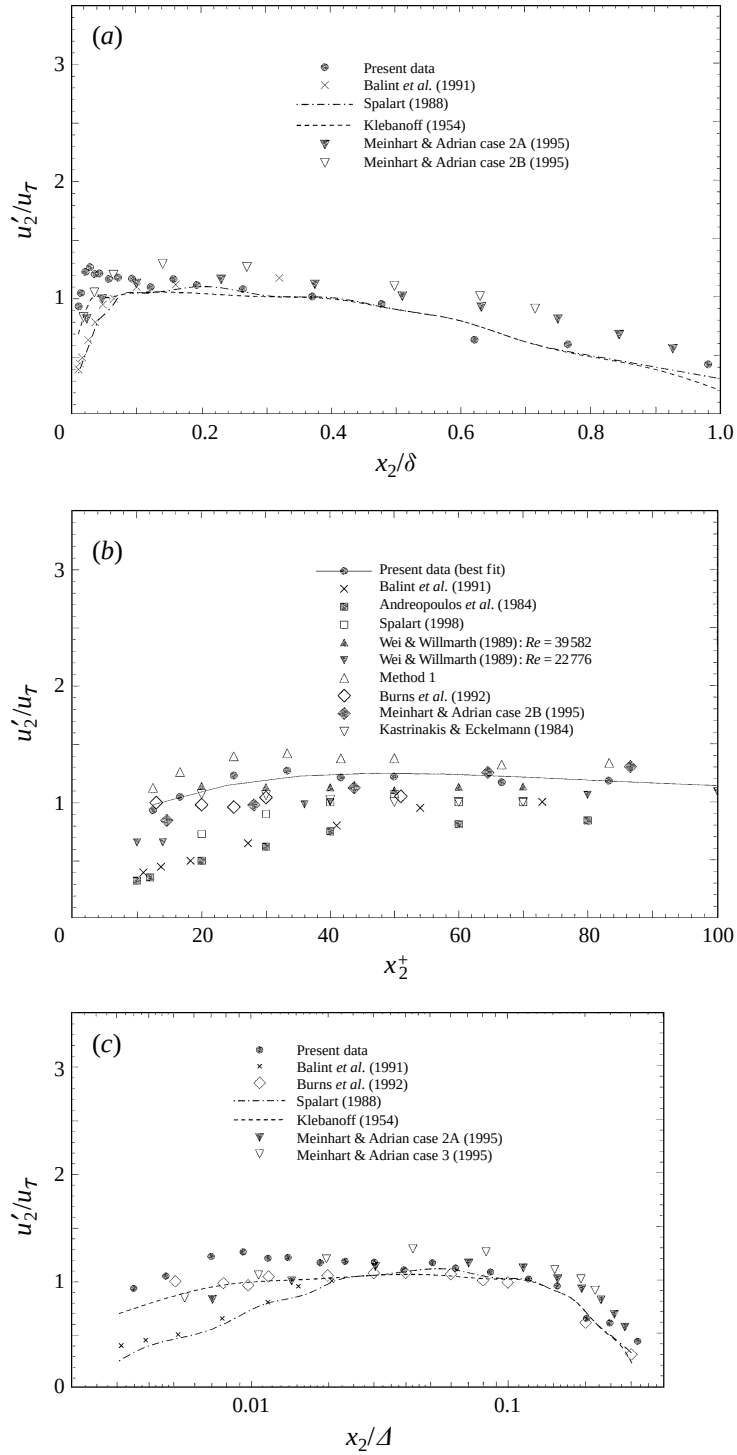

FIGURE 13. As figure 12 but for normal velocity fluctuations.

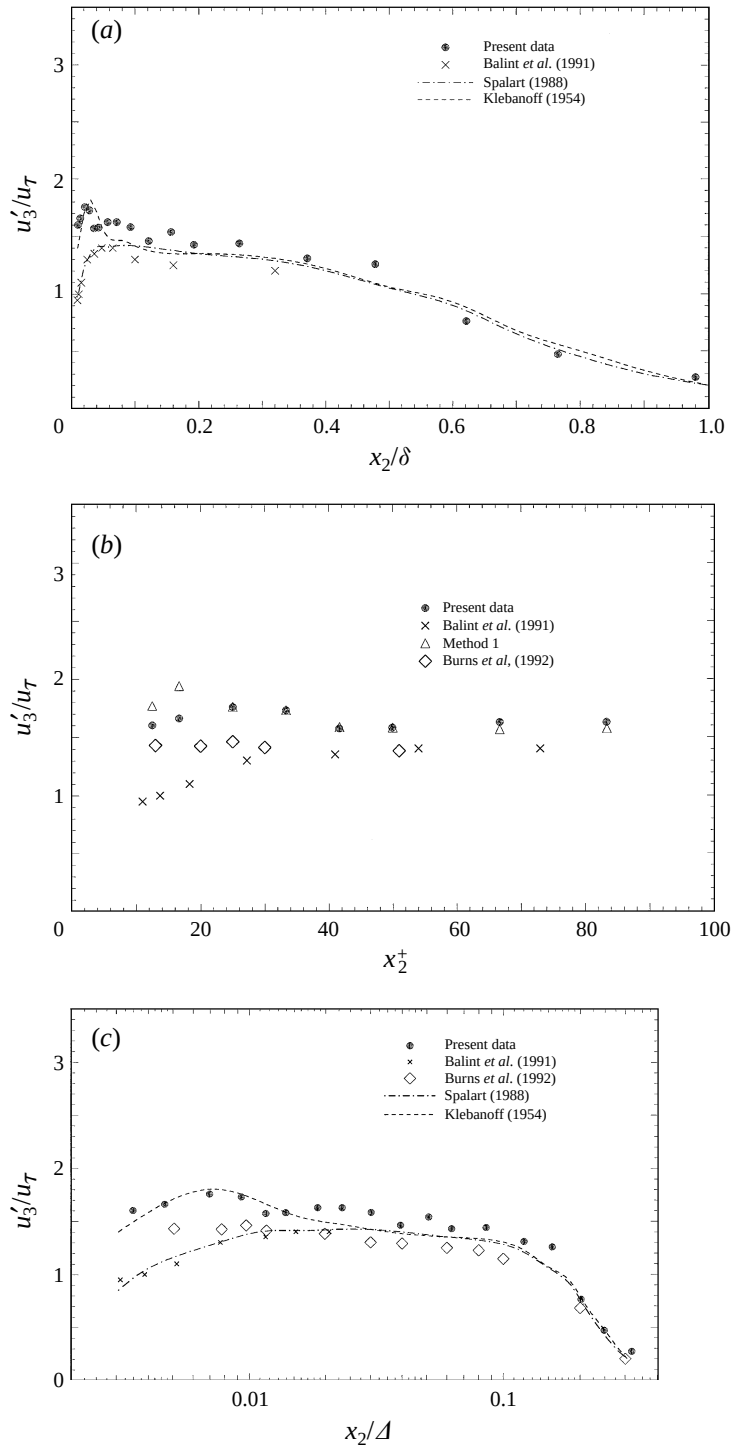

FIGURE 14. As figure 12 but for spanwise velocity fluctuations.

which is about three times higher than the present one they may suffer from non-equilibrium effects caused by a slow relaxation associated with a very long roughness strip used to trip the boundary layer. Thus Klebanoff's boundary layer is similar to that over a step from a rough to a smooth wall. Relaxation after such disturbances is very slow and even for shorter roughness strips it may take more than 50δ for the boundary layer to completely recover (see Andreopoulos & Wood 1982). Thus the large maximum value of Klebanoff's data is not a surprise.

All the data indicate that streamwise velocity fluctuations increase at distances closer to the wall. On the other hand the normal velocity fluctuations show a different trend in the near-wall region but then agreement is quite good with the measurements of Balint *et al.* (1991), Klebanoff (1954) and the simulation results of Spalart (1988) in the rest of the boundary layer. The data of Meinhart & Adrian (1995) are slightly higher in the outer-layer region than the rest of the data. The distribution of the r.m.s. of the spanwise velocity shown in figure 14(*a*) shows a reasonably good agreement with the data of Balint *et al.*, the data of Klebanoff and the simulations of Spalart in the outer part of the flow while differences are evident in the near-wall region. Balint *et al.*'s data follow very closely the simulations of Spalart in the near wall while the present measurements are in agreement with Klebanoff's data.

The same three velocity fluctuations, scaled with inner variables ν and u_τ are plotted in figures 12(*b*), 13(*b*) and 14(*b*) for x_2^+ values up to 100. The streamwise fluctuations u_1' are shown in figure 12(*b*). The present data are consistently lower than the data of Balint *et al.* (1991) by about 10% in the near-wall region. The difference between the two datasets appears to be mainly in the region $40 > x_2^+ > 20$. The data of case 3 of Meinhart & Adrian (1995) are closer to the present measurements. The data of Bruns, Dengel & Fernholz (1992) obtained at $Re_\theta = 2600$ and the data of Andreopoulos *et al.* (1984) obtained at $Re_\theta = 3600$ are also plotted for comparison. These two datasets and the data of Balint *et al.* agree rather well in the region $x_2^+ > 20$ although the corresponding Re_θ and spatial resolution effects are slightly different among them. Most of the differences in the measurements of turbulence statistics, in addition to the Re_θ and spatial resolution effects, can be attributed to the differences in the measurement techniques used, the accuracies associated with each of them and the errors involved in controlling the experimental conditions. In addition, the issue of scaling the data in the overlapping region between the lower edge of the logarithmic layer and the upper end of the buffer zone which corresponds to $40 > x_2^+ > 20$ is not clear yet (see Dussauge *et al.* 1996).

In the boundary layer investigated, the r.m.s. values of the normal velocity component, plotted in figure 13(*b*), are the lowest when compared with the r.m.s. levels of axial and spanwise velocity, as expected. The present results are compared to other data from the works listed in table 2. The effect of accounting for velocity gradients across the individual sensor arrays is also shown in figure 13(*b*). The results obtained with the numerical scheme of method 1 are higher by about 15% than those obtained with method 2. This simply demonstrates the importance of accounting for velocity gradients across each triple-wire probe.

The present data are comparable to those obtained in the LDA experiments of Wei & Willmarth (1989) made with remarkably low spatial resolution in the channel flow. Kastrinakis & Eckelmann's (1983) measurements are slightly lower as are the data of Bruns *et al.* and Meinhart & Adrian. These datasets illustrate the same trend as the current measurements. The data of Balint *et al.* and Andreopoulos *et al.* (1984), however, are considerably lower and show a different trend: they decrease much faster than the rest of the data with decreasing distance from the wall x_2^+.

The r.m.s. of spanwise velocity fluctuations, shown in figure 14(*b*), are in good agreement with Balint *et al.* (1991) for $x_2^+ > 40$. But near the wall these values deviate by a significant amount although the data compared used the same wall variables. Wei & Willmarth (1989) have shown that the turbulence intensities lack similarity with this scaling. Spalart (1988) and Kim *et al.* (1987) have also pointed out that these quantities are Reynolds-number dependent. The data of Bruns *et al.* are lower than the present ones and higher than those of Balint *et al.* Further discussion and comparison of higher-order moments of velocity fluctuations with the existing datasets can be found in the thesis by Honkan (1994).

It has been recently suggested by Dussauge *et al.* (1996) that the displacement thickness δ^* in its normalized form known as Rotta's thickness and defined as

$$\Delta = \int_0^\infty \frac{U_e - U}{u_\tau} \mathrm{d}x_2 = \delta^* \frac{U_e}{u_\tau}$$

could be used as outer layer length scale. This type of scaling has been shown in the work of Dussauge *et al.* to satisfactorily collapse the turbulent Reynolds stresses in the outer part of the boundary layer at various Re_θ. Figures 12(*c*), 13(*c*) and 14(*c*) show plots of the data considered in the present work by using Δ as length scale. The various data under consideration do not entirely collapse on one curve but show less scatter in the outer region of the boundary layer than in the case of figures 12(*a*), 13(*a*) and 14(*a*) where δ was used as a length scale. The present data agree rather well with the data of Spalart (1988) and Klebanoff (1954) and reasonably well with the data of Bruns *et al.* (1992) and Meinhart & Adrian (1995). As expected, large differences among the data exist in the near-wall region.

Among the previous experimental studies of two-dimensional zero-pressure-gradient turbulent boundary layers, the present work and that of Balint *et al.* are quite similar in terms of bulk flow parameters and techniques used. The present r.m.s. values of the normal and spanwise velocity fluctuations agree remarkably well with Balint *et al.* (1991) for $x_2^+ > 40$ but are higher closer to the wall. Since the drop out rate during the data reduction of samples closer to the wall was not higher than that in the outer region of the boundary layer, the noticeable difference could possibly be attributed to a greater number of velocity vectors being validated as a result of a larger acceptance cone as mentioned before. Physically, the present results suggest that the 'splash' effect of a turbulent fluid approaching the wall, which is associated with a reduction in normal fluctuations and an increase in lateral and longitudinal velocity fluctuations as well as in pressure fluctuations, starts to take place closer to the wall than previously thought.

In order to investigate how large the excursions of the velocity vector are and to verify if they are within the 'acceptance cone' of the probe, the statistics of two flow pitch and yaw angles θ_f and ϕ_t are computed. These two flow angles defined as

$$\theta_f = \sin^{-1}\left(\frac{u_1}{(u_1^2+u_2^2)^{1/2}}\right) \quad \text{and} \quad \phi_f = \sin^{-1}\left(\frac{u_3}{(u_1^2+u_3^2)^{1/2}}\right)$$

together describe the velocity vector orientation completely in space. The r.m.s. values of both these angles are shown in figure 15(*a*) as a function of normalized distance x_2^+ in the range up to 100. These values have been measured at the centre of the third triple wire. The peak r.m.s. value for flow pitch angle θ_f is about 7° and that of flow yaw angle ϕ_f is about 9°. This implies that instantaneous velocity signatures can vary from -3 r.m.s. to $+3$ r.m.s., which suggests a 6 r.m.s. $\approx 42°$ to 54° range of variation. This

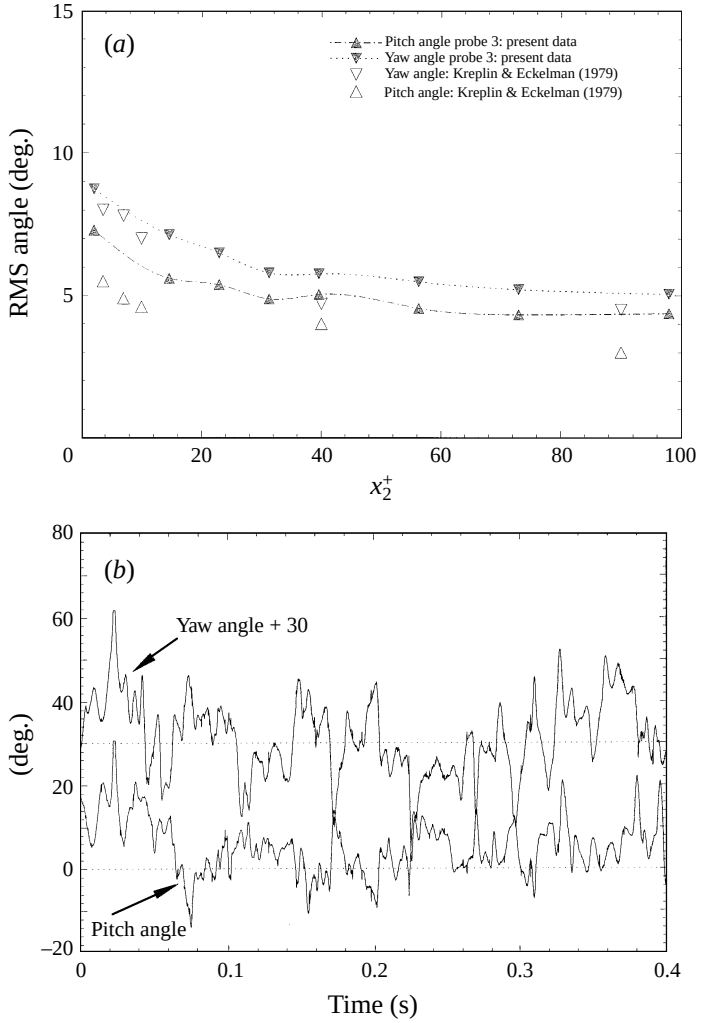

FIGURE 15. (*a*) Measured distribution of r.m.s. of pitch and yaw angles of velocity vectors in the near-wall region. (*b*) Typical time series records of pitch and yaw angles of velocity vectors at $x_2^+ = 12.5$.

is demonstrated in figure 15(*b*) where typical instantaneous signatures of both flow angles θ_f and ϕ_f are plotted. The time series for flow yaw angle ϕ_f is shifted by 30 units for clarity.

On figure 15(*a*), the present estimates of the r.m.s. of the velocity vector orientation angles are compared to those of Kreplin & Eckelman (1979). The data of Kreplin & Eckelman were obtained by integrating the distributions of the p.d.f.s of these angles which are available in their publication: an uncertainty of the order of 2° may be associated with this process. The yaw angle r.m.s. values agree very well with those of Kreplin & Eckelman while the pitch angle r.m.s. is about 1.5° lower. The maximum yaw angle measured by Kreplin & Eckelman is 30°. An inspection of the signal in figure 15(*b*) reveals that the maximum of this sample is also 30°, occurring at about $t = 0.025$ s. The minimum value of the pitch angle cited in their paper is 10° which also agrees with the present observations. However, the maximum value of the pitch angle measured in their work is only 16°, while the present estimates indicate that the

pitch angle can reach values as high as 30°. This suggests that the motions away from the wall (pitch angle positive, $\theta_f > 0$) are more violent in the present boundary layer than in their channel flow of rather low $Re_\theta = 770$.

The present data were further analysed by computing the probability distribution functions of these angles as measured by the first sensor triplet of the probe. The probability density distribution of flow angle θ_f is shown as a function of the r.m.s. normalized angle in figure 16(*a*). This distribution is skewed to the left, indicating that frequently occurring low-amplitude fluctuations are countered by rare but strong positive fluctuations. This however is not the case for the flow yaw angle ϕ_f, since its distribution is quite symmetric in that positive fluctuations are as likely as negative ones and that the tails are also symmetrically distributed. High-amplitude fluctuations of over four times the r.m.s. value of 7°, although less frequent, are observed in figure 16(*b*), which shows the probability distribution values of flow yaw angle ϕ_f against the angle expressed in terms of its r.m.s. value. It is therefore plausible, in the context of probe performance, that the probe of Balint *et al.* (1991) because of its geometry may not be able to capture these high fluctuations in magnitude and direction of the velocity vector.

5.4 *Production/dissipation of turbulent kinetic energy*

The rate of production of turbulent kinetic energy from the mean motion is given by $-\overline{u_i u_j}\,\partial\overline{U_i}/\partial x_j$ and the rate of dissipation of turbulent kinetic energy to heat is given by expression (3.1).

The distributions of production and dissipation rates of turbulent kinetic energy in the boundary layer flow at two Reynolds numbers, normalized by inner variables ν/u_τ^4 are plotted in figure 17 as a function of x_2^+. The dissipation rates have been computed by considering all the terms in expression (3.1) for ϵ because the flow near the wall clearly being anisotropic, the cross-products of the velocity derivatives may be just as important as the other terms. On this plot the DNS data of Spalart (1988) and Mansour, Kim & Moin (1988) and the experimental data Balint *et al.* (1991) and Wei & Willmarth (1989) are also superimposed. For reference the relation, $\epsilon^+ = 1/kx_2^+$ (where k is the Kármán constant) obtained by assuming both rates to be equal in the logarithmic region, is also plotted. The present values of dissipation rate at both Reynolds numbers are slightly higher than those of Balint *et al.* (1991) and the simulation data of Mansour *et al.* (1988) but compare well with values of Spalart (1988). The production rate values also agree quite well with Balint *et al.* (1991) for the lower and higher Re_θ. These values compare particularly well with Spalart's (1988) simulations for $x_2^+ > 25$ and agree with Wei & Willmarth's (1989) for $x_2^+ < 25$.

The overall assessment of the probe performance in the measurement of velocity fluctuations appears to be very satisfactory. Accounting for velocity gradients across the individual triple-wire sensors improved substantially the measurement of shear stress and the two lateral stresses in the near-wall region. Mutual interference among the hot-wire sensors is minimal and the shear stress measurements as well as those of turbulent kinetic energy production and dissipation rates agree quite well with the data of Balint *et al.* (1991) and the simulations of Spalart (1981) and Mansour *et al.* (1981). The probe seems to, possibly, underestimate by 10% the r.m.s. value of the longitudinal velocity fluctuations in the upper edge of the buffer-layer region where most of the existing data disagree and where inner-layer viscous scaling may not be the proper scale to normalize the data. The use of Rotta's thickness Δ to scale the statistical results in the outer layer appears to reduce the scatter of the data considerably.

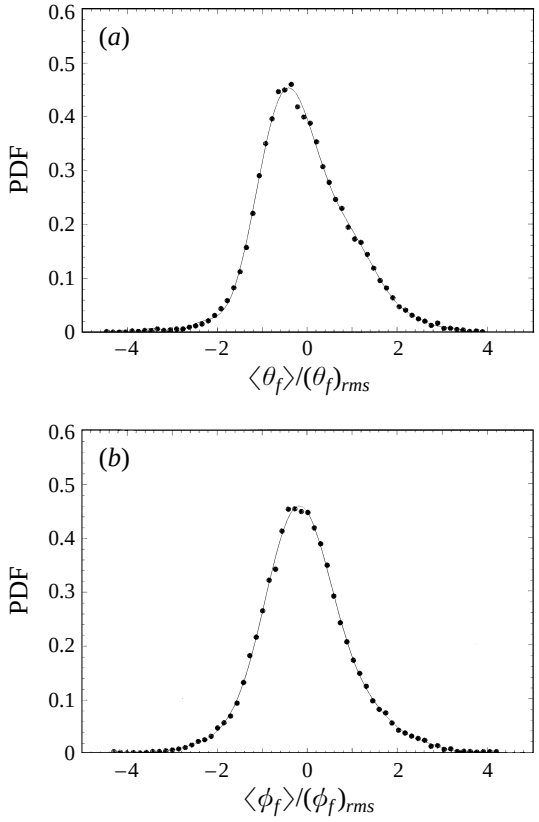

FIGURE 16. Probability density function of flow angles: (*a*) θ_f, (*b*) ϕ_f.

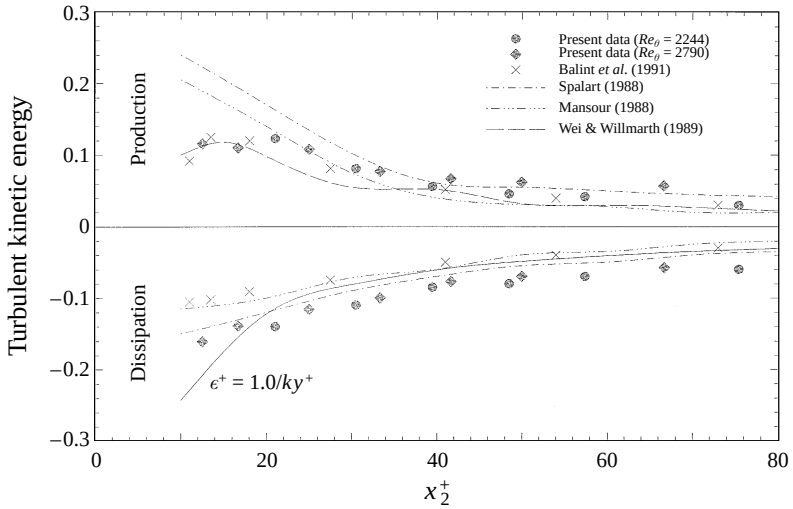

FIGURE 17. Computed production and dissipation rates of turbulent kinetic energy in inner-layer scaling.

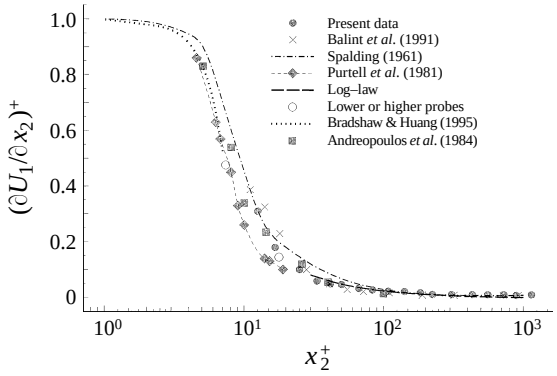

FIGURE 18. Mean velocity gradient $\partial U_1 \partial x_2$ across the boundary layer.

5.5. *Accuracy estimates of velocity gradient measurements*

A comparison between the mean velocity gradient $\overline{(\partial U_1/\partial x_2)}$ and the derivative of the mean velocity profile $(\partial \overline{U_1}/\partial x_2)$ is a good indicator of the probe's ability to measure at least one velocity gradient with sufficient accuracy. Figure 18 shows the distribution of the mean velocity gradient $\overline{(\partial U_1/\partial x_2)}$ across the boundary layer as measured at the centroid of the nine-wire probe by time-averaging its instantaneous values. On the same figure data of the mean velocity derivative are plotted which have been obtained by differentiating Spalding's (1961) formula of mean velocity distribution in the near-wall region including the buffer zone and the logarithmic region. In addition, the data of the mean velocity derivative in the logarithmic region, $1/\kappa x_2^+$, where κ is von Kármán's constant, are also plotted for comparison. The data obtained by differentiating the near-wall velocity measurements of Purtell, Klebanoff & Buckley (1981) and Andreopoulos *et al.* (1984) have also been plotted in the same figure. Purtell *et al.*'s mean velocity data show no Re_θ effect in the near-wall region and therefore the deduced mean velocity gradient data are independent of Re_θ. The data of Andreopoulos *et al.* correspond to $Re_\theta = 3624$.

The present data are also compared with those of Balint *et al.* (1991). It appears that the agreement of the present data with those of Balint *et al.* and with Spalding's formula in the buffer region is very satisfactory. Both datasets are also in very good agreement with the data obtained from the relation of the logarithmic law in the region of its validity. The data of Purtell *et al.* are lower than those predicted by Spalding's correlation while the data of Andreopoulos *et al.* are closer to Spalding's prediction in the upper edge of the buffer layer and close to Purtell's data at the upper edge of the viscous sublayer. However, if one considers that the uncertainty introduced in deducing these data and the uncertainty band associated with Spalding's formula, which originates from a modest 5% uncertainty in the initial mean velocity measurements, the agreement of the present measurements with existing data and correlations is quite satisfactory. It should be also pointed out that Spalding's relation should be reconsidered in light of recent demonstrations of limitations of the classical law-of-the-wall for the viscous sublayer. Bradshaw & Huang (1995), for instance, have shown that integration of the total shear stress expression yields

$$\frac{\partial \overline{U_1}}{\partial x_2^+} = 1 - A(x_2^+)^3 \quad \text{where} \quad A = \overline{\frac{\partial u_1}{\partial x_2}\frac{\partial p}{\partial x_2}}.$$

The value of this coefficient, as suggested by Mansour *et al.* (1988), is 1.4×10^{-3} and

the whole subtracting term represents the contribution of the turbulent part of the total shear stress if the later is independent of the wall distance in the viscous sublayer. Based on this relation the velocity gradient appears to be lower than what is calculated from Spalding's formula (see figure 18).

Two additional points are plotted in figure 18 which have been obtained by differentiating the measured mean velocity data at $x_2^+ = 7.33$ and $x_2^+ = 17.7$ when the centroid of the probe is located at $x_2^+ = 12.5$. This has been accomplished by considering the finite difference of mean velocities measured by the lower pair of triple-sensor probes for data at $x_2^+ = 7.33$, and by the upper pair of triple-sensor probes for data at $x_2^+ = 17.7$. The average of these two values is almost exactly the value plotted for the velocity gradient at $x_2^+ = 12.5$. The value of the velocity gradient at the nearest to the wall location falls below Spalding's prediction but compares very well with Purtell *et al.*'s data. Thus, it appears that the probe is capable of measuring mean velocity gradients within about 12% in the near-wall region. Given the uncertainties involved in deducing Spalding's formula this uncertainty can be considered as very satisfactory. Another indicator of the accuracy involved in the measurements of velocity gradients is the residual value of the average value of velocity gradient and its r.m.s. in the free stream: 1.1% and 0.5% of its mean value at the wall, respectively. In terms of vorticity the residual value of the average vorticity in the free stream is about 1.3% of the mean wall value while the residual r.m.s. of vorticity is about 1/40 of the measured maximum r.m.s. values in the near-wall region.

Estimates of the uncertainties associated with the measurements of velocity gradients can also be obtained by considering the propagation of the uncertainties in the measurement of each quantity involved in the process. A typical velocity gradient is measured through the following approximation:

$$\frac{\partial U_i}{\partial x_j} \simeq \frac{U_2 - U_1}{l_p} P = F,$$

where U_2 and U_1 are the velocities at two nearby locations, l_p is the distance between these locations and P is the scaling parameter which may be δ/U_e in the case of outer-layer scaling or ν/u_τ^2 if inner layer scaling is used. If the uncertainties in the measurements of U_2 and U_1 are the same, $\Delta U_1 = \Delta U_2 = \Delta U$, and l_p is determined accurately, then the relative uncertainty $\Delta F/F$ will be given by

$$\frac{\Delta F}{F} = \left(2\left(\frac{\Delta U}{U_2 - U_1}\right)^2 + \left(\frac{\Delta \delta}{\delta}\right)^2 + \left(\frac{\Delta U}{U_e}\right)^2\right)^{1/2}$$

for the case of outer laying scaling and

$$\frac{\Delta F}{F} = \left(2\left(\frac{\Delta U}{U_2 - U_1}\right)^2 + 4\left(\frac{\Delta u_\tau}{u_\tau}\right)^2\right)^{1/2}$$

for the case of inner-layer scaling. A typical ΔU is 1%, which corresponds to about 0.01 m s^{-1}, while typical velocity differences $U_2 - U_1$ can be estimated from the mean velocity differences at three locations in the boundary layer:

(i) inside the viscous sublayer $\overline{U_2} - \overline{U_1} = u_\tau \Delta x_2^+ = 1.3$ m s^{-1} where $\Delta x_2^+ = l_p = 10$ (probe size);

(ii) inside the buffer layer $\overline{U_2} - \overline{U_1} = 0.3 u_\tau \Delta x_2^+ = 0.39$ m s^{-1} where 0.3 is obtained from figure 18;

(iii) Inside the logarithmic region at $x_2^+ = 40$ $\overline{U_2} - \overline{U_1} = u_\tau \Delta x_2^+ / k x_2^+ = 0.08$ m s^{-1}. If typical uncertainties of 3% and 5% are assumed in determining δ and u_τ respectively,

then the uncertainty $\Delta F/F$ appears to be 10% in the viscous sublayer and buffer region and 20% in the logarithmic region in the case of inner-layer scaling. If outer-layer scaling is used the relative uncertainty is 5% in the viscous sublayer, 6% in the buffer region and 18% in the logarithmic region. Although the way errors propagate through the data is not always what is described by the square root of mean-squared partial errors used above, this analysis clearly demonstrates that the uncertainty of the measured velocity gradient in the near-wall region is higher when inner layer scaling is used. The relative uncertainty $\Delta F/F$ increases as the distance away from the wall increases because the absolute value of F decreases. However, the difference between the estimates of uncertainties in the two different scalings decreases with increasing distance from the wall.

5.6. *Vorticity statistics*

If the transport equation of vorticity (1.2) is multiplied by ω_i the transport equation for the instantaneous enstrophy $\frac{1}{2}\omega_i^2$ can be obtained:

$$\frac{\mathrm{D}(\frac{1}{2}\omega_i\,\omega_i)}{\mathrm{D}t} = s_{ik}\,\omega_k\,\omega_i + \nu\frac{\partial^2(\frac{1}{2}\omega_i\,\omega_i)}{\partial x_k\,\partial x_k} - \nu\left(\frac{\partial\omega_i}{\partial x_k}\right)\left(\frac{\partial\omega_i}{\partial x_k}\right). \tag{5.1}$$

It should be also mentioned that the instantaneous enstrophy is the second invariant of the strain-rate matrix s_{ij} (see Soria *et al.* 1994). The first term on the right-hand side, $\omega_k\,\omega_i\,s_{ik}$, is a source/sink term describing the generation or destruction of enstrophy by the strain s_{ik} through rotation and stretching or compression of vortex lines. The time-average value of this very important quantity in the dynamics of turbulent flows was found by Tsinober *et al.* (1992) to be always positive in grid-generated turbulence, indicating the prevalence of vortex stretching over compression.

The r.m.s. fluctuations of the three components of vorticity across the boundary layer have been scaled by the boundary-layer thickness δ and friction velocity u_τ and plotted in figures 19(*a*), 19(*b*) and 19(*c*). The values are then compared with the results of Spalart (1988), Balint *et al.* (1991) and Lemonis (1995) for ω_1, ω_2 and ω_3. Additionally the measurements of Klewicki (1989) and Meinhart & Adrian (1995) are also indicated on the plots for ω_3. In order to demonstrate the effect of accounting for the velocity gradients across the individual probes on the vorticity data the data obtained with method (i) are also plotted for comparison. It can be seen that a 5% reduction in the r.m.s. of longitudinal vorticity fluctuations in the near-wall region can be attributed to this effect. At distances greater than 0.1 δ this effect is not noticeable. It should also be mentioned that this effect is most pronounced in the statistical quantities of the longitudinal vorticity component. This is not surprising because ω_1 is based on the velocity gradients of the lateral and normal velocity components which have been reduced the most by this effect.

Very near to the wall, Balint *et al.*'s (1991) data for ω_1 are considerably lower than present data. Spalart's (1988) data are noted to be lower than both the experimental measurements. The data provided by Lemonis are very close to the present ones for $x_2/\delta > 0.1$ and close to those of Balint *et al.* (1991) in the near-wall region. The present values of normal vorticity fluctuations ω_2' collapse well with Balint *et al.* (1991) in the near-wall region but decrease much more gradually in the rest of the boundary layer. They agree rather well with the data of Lemonis in the outer region. The fluctuations of the dominant spanwise component of vorticity ω_3' as measured by this probe compare very well with the data of Lemonis and the results of Balint *et al.* (1991). The PIV result of Meinhart & Adrian (1995) are closer to the simulation data of Spalart

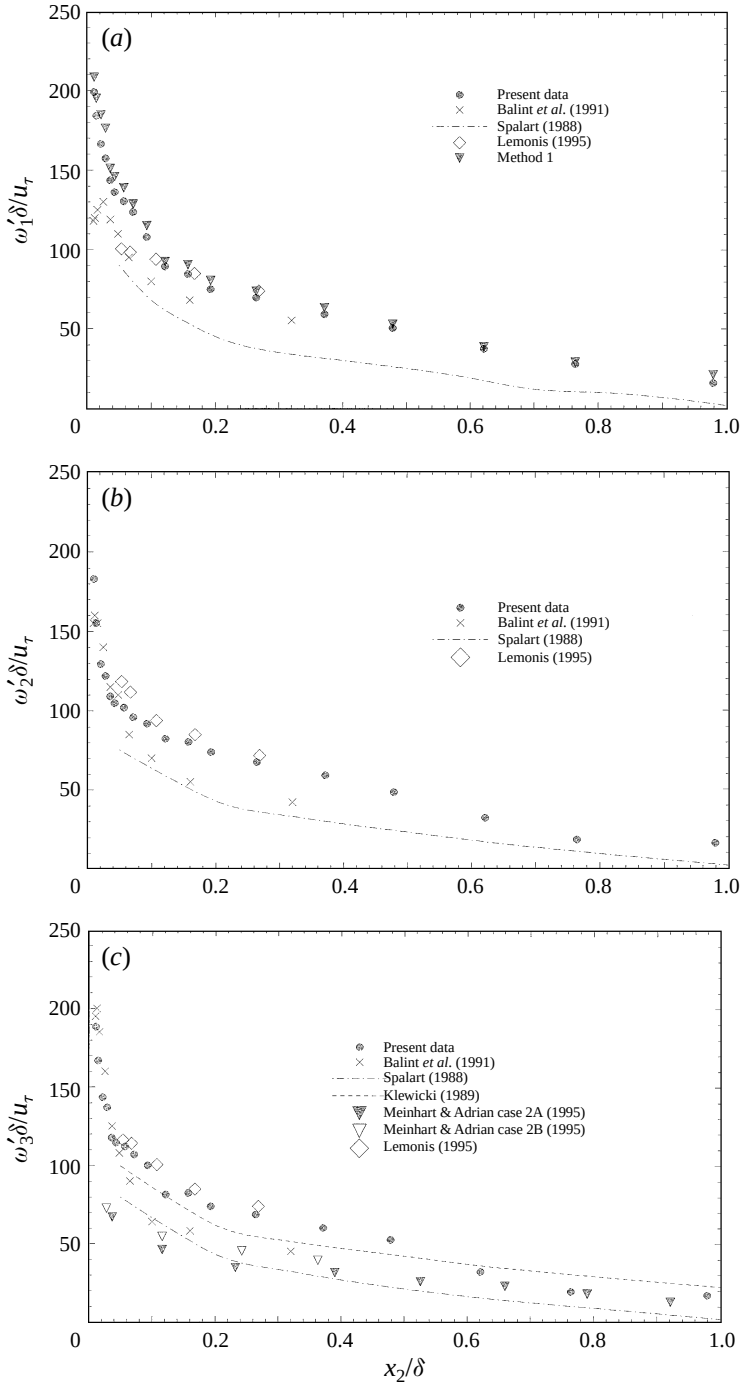

FIGURE 19. R.m.s. of (*a*) axial, (*b*) normal and (*c*) spanwise vorticity fluctuations normalized by outer variables u_τ and δ.

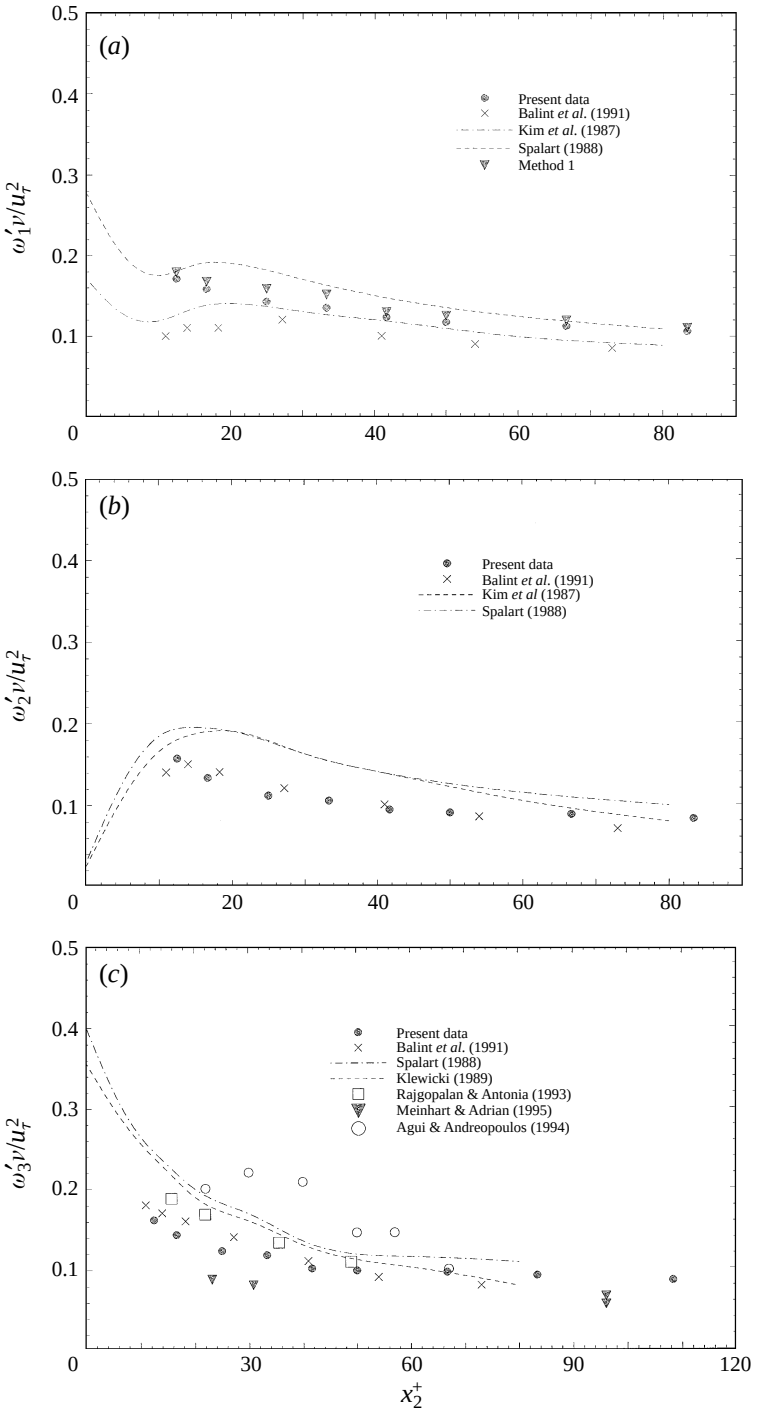

FIGURE 20. R.m.s. of (*a*) axial, (*b*) normal and (*c*) spanwise vorticity fluctuations normalized by inner variables u_τ and ν.

(1988) but are considerably smaller than the rest of experimental data in the near-wall region. Case 2*b* of Meinhart & Adrian's data correspond to a spatial resolution of $\Delta x_1^+ = \Delta x_2^+ = 20$ while the data of case 2*a* have been obtained with a spatial resolution of 14 expressed in viscous units.

The same three vorticity components when normalized by the boundary-layer thickness δ and free-stream velocity U_∞ exhibit similar properties but the differences observed in the previous scaling are not as large. It is expected that in the near-wall region, inner variables ν and u_τ will be appropriate scales. The results, normalized by the inner variables u_τ and ν are shown in figures 20(*a*), 20(*b*) and 20(*c*). As was demonstrated earlier, the uncertainties involved in the data on vorticity are considerably higher when inner-layer scaling is used because it involves u_τ^2. Thus r.m.s. values of vorticity component fluctuations, when scaled with u_τ and ν, are subject to large variations when comparisons are made of values obtained from different types of measurement techniques and simulations. The apparently excessive differences in the near-wall values of ω_1 appear to be within the normal experimental variations and in fact the results are comparable to those of Spalart (1988) although at a much lower Reynolds number and only slightly larger than the simulated results of Kim *et al.* (1987). Balint *et al.* (1991) attribute their attenuated values to the problems associated with the convergence of the solutions to the equations for the hot-wire outputs. The present values of the r.m.s. of ω_1 lie between the two simulation results of Kim *et al.* (1987) and Spalart (1988). The values of ω_2 are in good agreement with the results of Balint *et al.* (1991) but both results are lower than the data of Kim (1987) and Spalart (1988) for $x_2^+ < 50$. The spanwise component, ω_3 is in close agreement with Balint *et al.* (1991) but again, like the normal component, results of Spalart (1988) and Kim *et al.* (1987) as well as those of Klewicki (1989) are found to be relatively higher. The data of Meinhart & Adrian are still lower than the present ones. The LDA results of Agui & Andreopoulos (1994) have been obtained in the same facility as the present data under the same conditions. Although these data are in the process of another verification by different optical techniques, they appear to be genuinely higher than all hot-wire data, most probably because of better spatial resolution. The LDA measurements at the point closest to the wall do not follow the general trend, most probably because of distortions of the probe volume by the nearby wall.

One characteristic feature of vorticity fluctuations is that their magnitude is of the same order of magnitude or greater than the corresponding mean vorticity. In the buffer region away from the viscous sublayer the r.m.s. of vorticity fluctuations is about 0.2 in inner wall units while the mean vorticity as shown in figure 18 is about 0.3. If the intensity of vorticity fluctuations is defined as the ratio of its r.m.s. to the mean vorticity value then it will reach values of the order of 60% in this region. In the log–law region the r.m.s. is about 0.1 while mean vorticity is about 0.02. Thus the intensity of vorticity fluctuations can be close to 500%.

The skewness values of the present measurements are shown in figures 21(*a*), 21(*b*) and 21(*c*). The skewness of the axial vorticity component is close to zero while that of the normal component is more negative when compared to Balint *et al.* (1991). The expected all negative variation of skewness in the spanwise component is well reproduced although numerically much less than that of Spalart (1988) and Klewicki (1989) in the region $x_2^+ < 80$. The negative values for skewness for ω_3 indicates that rather large positive fluctuations of spanwise vorticity are less likely than the negative fluctuations of comparable magnitude, which in turn can be interpreted as stretching of spanwise component occurring more often than compression or the passage of vortical eddies.

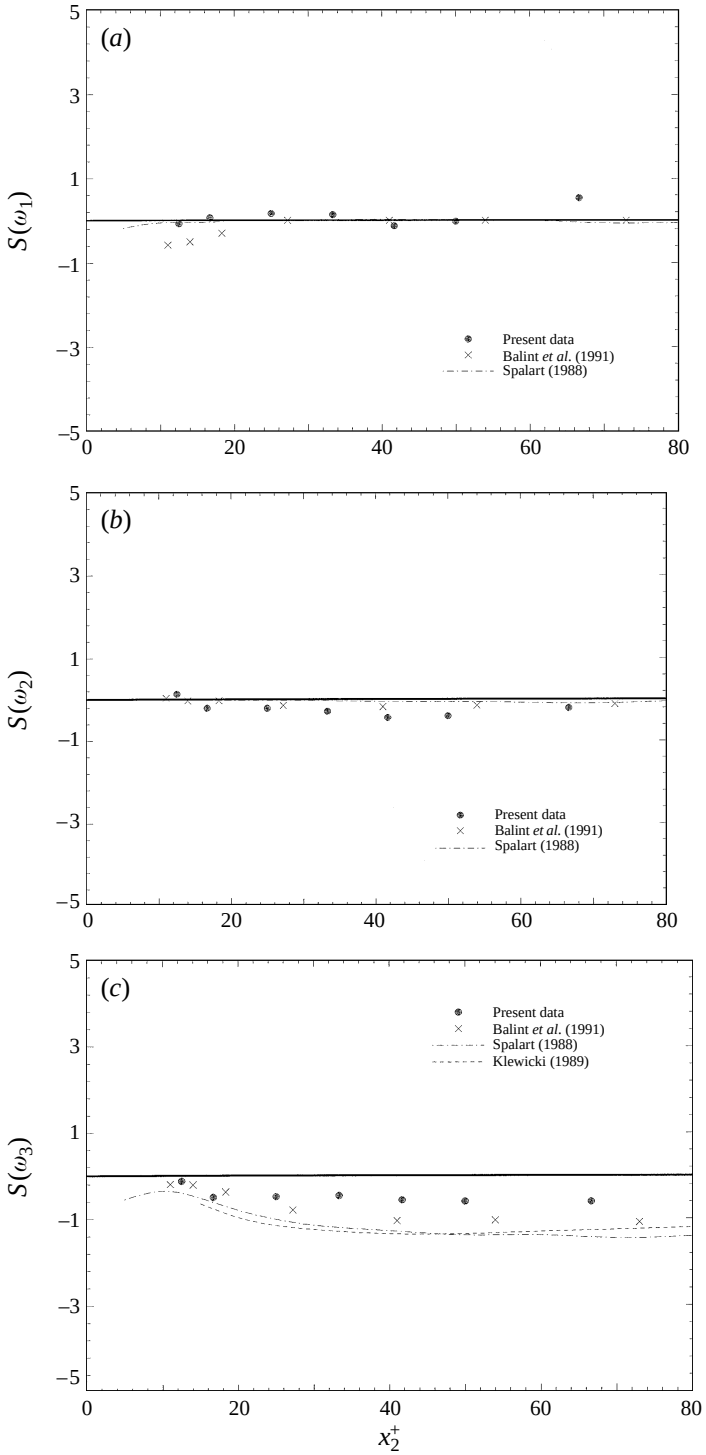

FIGURE 21. Skewness of (*a*) longitudinal, (*b*) normal and (*c*) spanwise vorticity fluctuations.

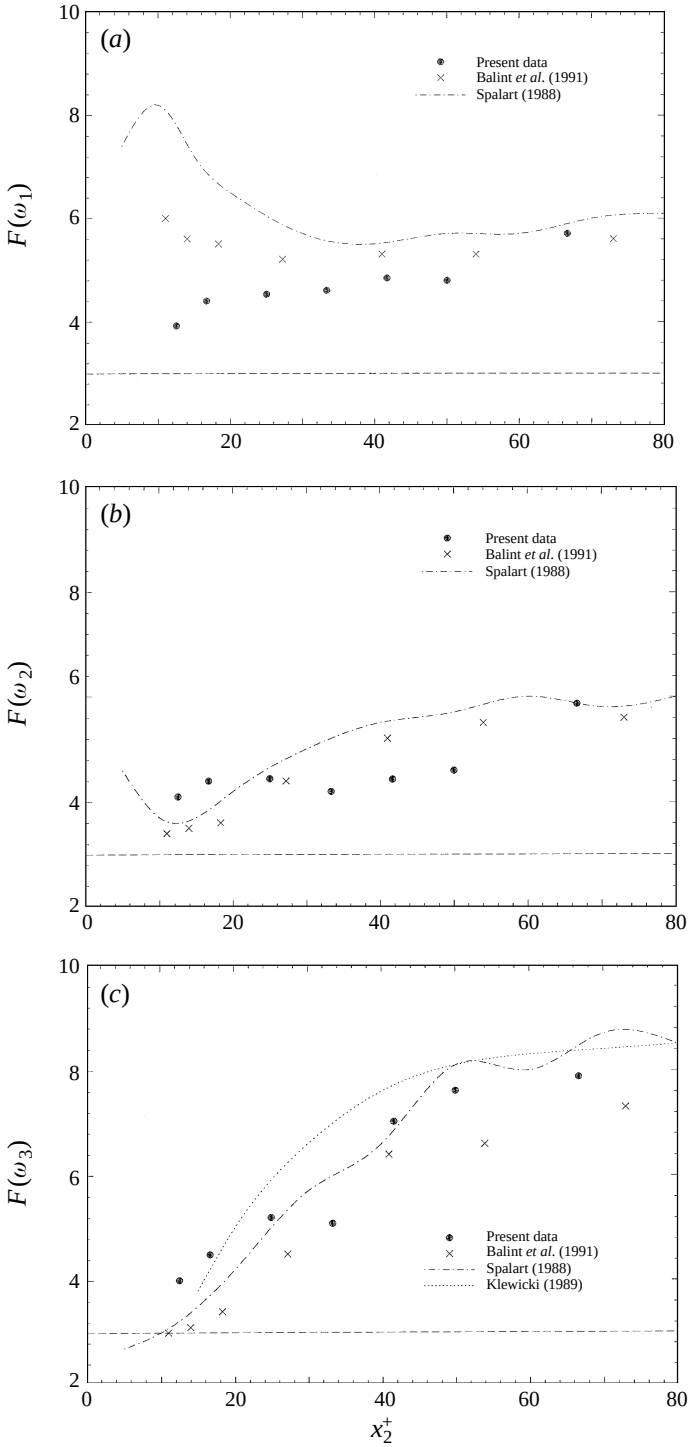

FIGURE 22. Flatness of (*a*) longitudinal, (*b*) normal and (*c*) spanwise vorticity fluctuations.

The flatness values for the three vorticity components $F(\omega_1)$, $F(\omega_2)$ and $F(\omega_3)$ are shown in figures 22(*a*), 22(*b*) and 22(*c*). A value of 3 corresponding to a Gaussian distribution is also shown for reference. Numerically simulated values of Spalart (1988) for ω_1 are quite large, especially in the region $x_2^+ < 20$. For $x_2^+ > 20$ the present values agree fairly well with Balint *et al.*'s (1991). The experimental results of Klewicki (1989) for ω_3 conform to the present data except for the fourth point. Flatness values of Balint *et al.* (1991), in comparison, are found to be the lowest throughout the region displayed. For distances away from the wall, the significant increase in the flatness factors of the ω_1 and ω_3 components reflects the intermittent character of the flow with sporadic occurrence of streamwise vortices.

By Reynolds averaging equation (5.1) it is possible to obtain a transport equation for the time-averaged enstrophy $\frac{1}{2}\overline{\omega_i\,\omega_i}$. Balint *et al.* (1988) produced a balance of all terms of this equation which indicated that the term $\overline{\omega_k'\,\omega_i'\,s_{ik}} = \overline{\omega_1'\,\omega_2'\,s_{12}}$ is the largest contributor as a source in the total balance. This term reaches very large values near the wall where $\overline{s_{12}}$ is maximum. Symmetry considerations and invariance in the spanwise direction of all average quantities suggest that the cross-correlation $\overline{\omega_1'\,\omega_2'}$ is the only non-zero correlation between the fluctuating vorticity components. In fact the present measurements at $x_2^+ = 12.5$ indicate the following correlation coefficients $r_{ij} = \overline{\omega_i'\,\omega_j'}/[\omega_{i,rms}\,\omega_{j,rms}]$: $r_{12} = 0.25$, $r_{13} = 0.06$ and $r_{23} = 0.025$.

5.7. *Rate-of strain statistics*

Understanding the dynamically significant processes in the near-wall region requires consideration of the transport equation for $2s_{ij}\,s_{ij}$ which is related to the total dissipation. This is accomplished by taking

$$2s_{ij}\,s_{ij} = \left[\left(\frac{\partial u_i}{\partial x_j}\frac{\partial u_i}{\partial x_j}\right) + \left(\frac{\partial u_i}{\partial x_j}\frac{\partial u_j}{\partial x_i}\right)\right] \tag{5.2}$$

and obtaining a transport equation for each of the right-hand-side terms of this relation. This equation yields

$$\frac{\mathrm{D}(2s_{ij}\,s_{ij})}{\mathrm{D}t} = -4s_{ik}\,s_{kj}\,s_{ij} - \omega_i\,\omega_j\,s_{ij} - 4s_{ij}\frac{1}{\rho}\frac{\partial^2 p}{\partial x_i\,\partial x_j} + \nu\frac{\partial^2(2s_{ij}\,s_{ij})}{\partial x_k\,\partial x_k} - 4\nu\left(\frac{\partial s_{ij}}{\partial x_k}\right)\left(\frac{\partial s_{ij}}{\partial x_k}\right). \tag{5.3}$$

The term on the left-hand side can be interpreted as the advection of the instantaneous $2s_{ij}\,s_{ij}$ while the first four terms on the right-hand side are source/sink terms representing complex nonlinear interactions among the various components of the strain tensor, rotation and stretching/compression of vorticity and an interaction of the pressure hessian with the s_{ij}. It should be noted that the term $-\omega_i\,\omega_j\,s_{ij}$ present in (5.3) is also present in (5.1) with an opposite sign. If it is positive in (5.1), i.e. is generating enstrophy, then it attenuates fluctuations in the balance of $2s_{ij}\,s_{ij}$.

The r.m.s. fluctuations of three off-diagonal components of the rate-of-strain tensor s_{12}, s_{13} and s_{23} across the boundary layer scaled by δ and u_τ are shown in figure 23(*a*). They reach maximum values close to the wall and their distribution is similar to that of the individual components of enstrophy. It should be noted that the r.m.s. values between s_{ij} and ω_k are related through

$$\overline{s_{ij}^2} - \tfrac{1}{4}\overline{\omega_k^2} = \overline{\frac{\partial u_i}{\partial x_j}\frac{\partial u_j}{\partial x_i}} \tag{5.4}$$

(no summation convention is assumed over i, j or k). Symmetry considerations of the

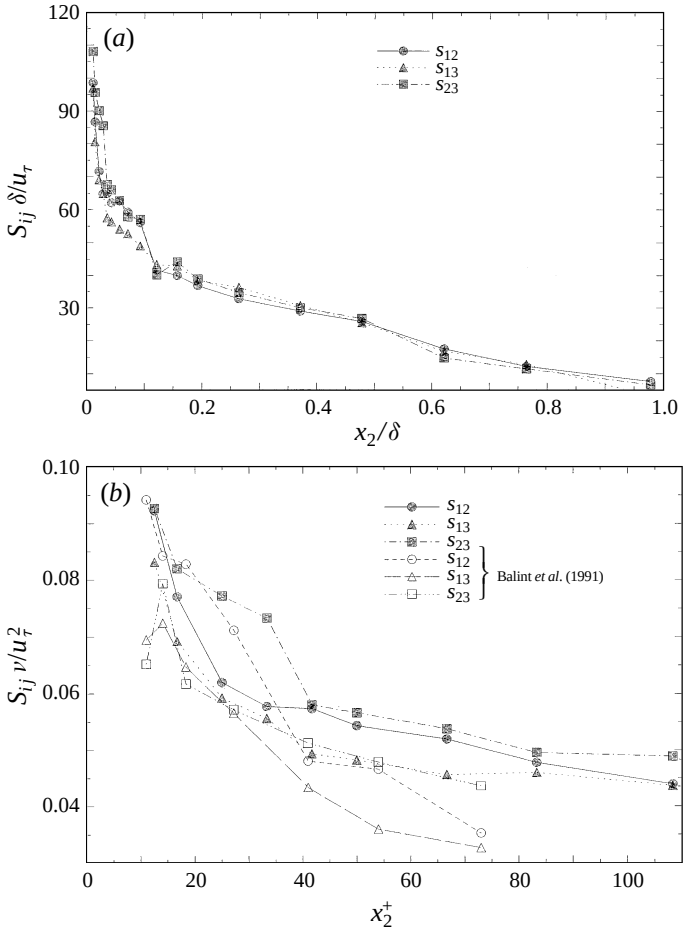

FIGURE 23. R.m.s. of fluctuations of the three off-diagonal components of the rate-of-strain tensor, (*a*) across the boundary layer, and (*b*) in the near-wall region.

present two-dimensional flow suggest that the right-hand side of this relation is always non-zero, which precludes the ratio of the two r.m.s. from being $\frac{1}{2}$. If this term is neglected by assuming a zero value than the dissipation rate appears to be

$$\epsilon = 2\nu\,\overline{s_{ij}\,s_{ij}} \cong \nu\,\overline{\omega_k\,\omega_k} \cong \nu\,\overline{\frac{\partial u_i}{\partial x_j}\frac{\partial u_i}{\partial x_j}}, \tag{5.5}$$

which is strictly valid only for homogeneous flows. It should be mentioned that the transport equation (5.3) contains contributions from the homogeneous part as well as from the inhomogeneous part of (5.2).

Figure 23(*b*) shows the same data scaled by inner wall variables together with the data of Balint *et al.* (1991) for a direct comparison. The latter have been computed from the relation

$$\overline{s_{ij}^2} + \tfrac{1}{4}\overline{\omega_k^2} = \frac{1}{2}\overline{\left(\frac{\partial u_i}{\partial x_j}\right)^2} + \frac{1}{2}\overline{\left(\frac{\partial u_j}{\partial x_i}\right)^2} \tag{5.6}$$

(no summation convention is assumed over i, j or k) and the available r.m.s. values of vorticity components and velocity gradients. It should be mentioned that the present data for s_{ij} obtained directly by time averaging the time-dependent data and those

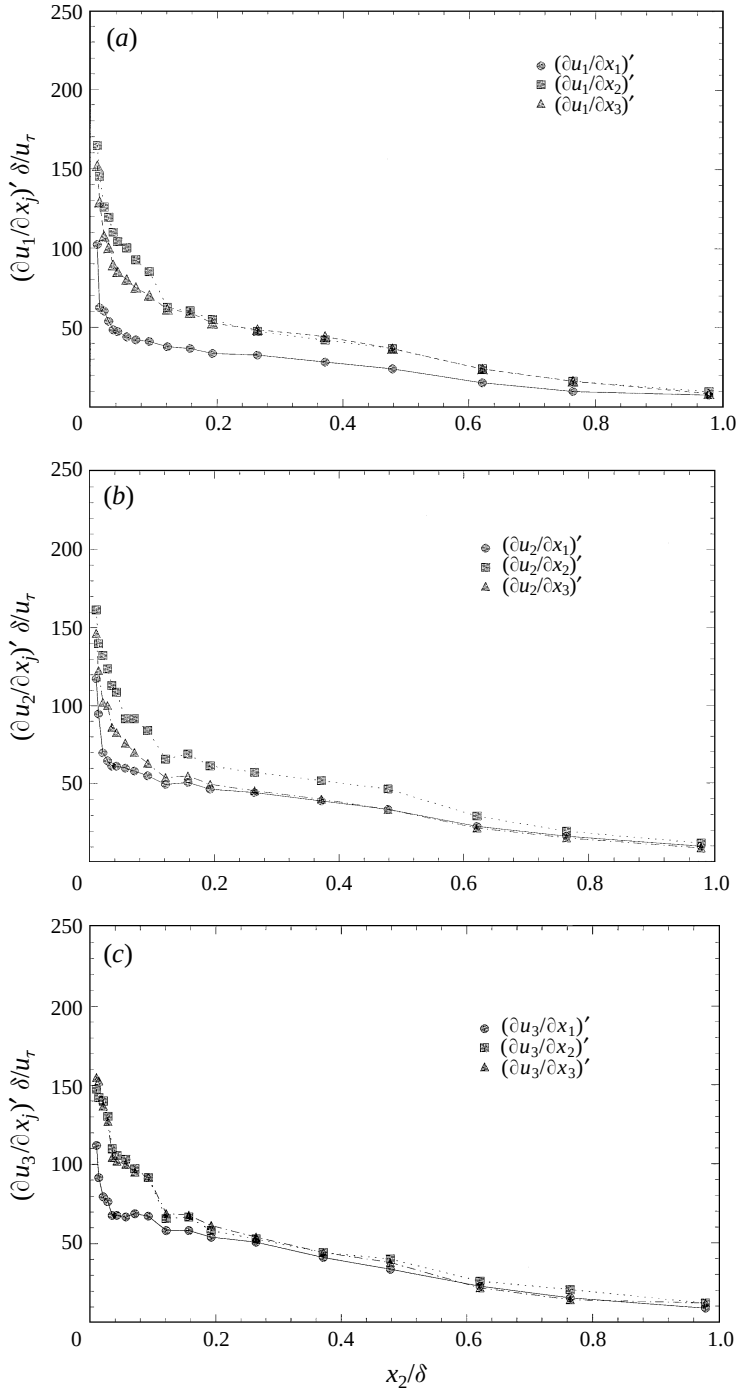

FIGURE 24. R.m.s. of fluctuations of spatial derivatives of velocity normalized by outer variables.

deduced from equation (5.6) by using existing r.m.s. values of the quantities involved are identical. This is another indication of the internal consistency of the data.

It appears that the present values are higher than those of Balint *et al.* (1991) most probably for the same reasons discussed before, in the previous section, §5.3.

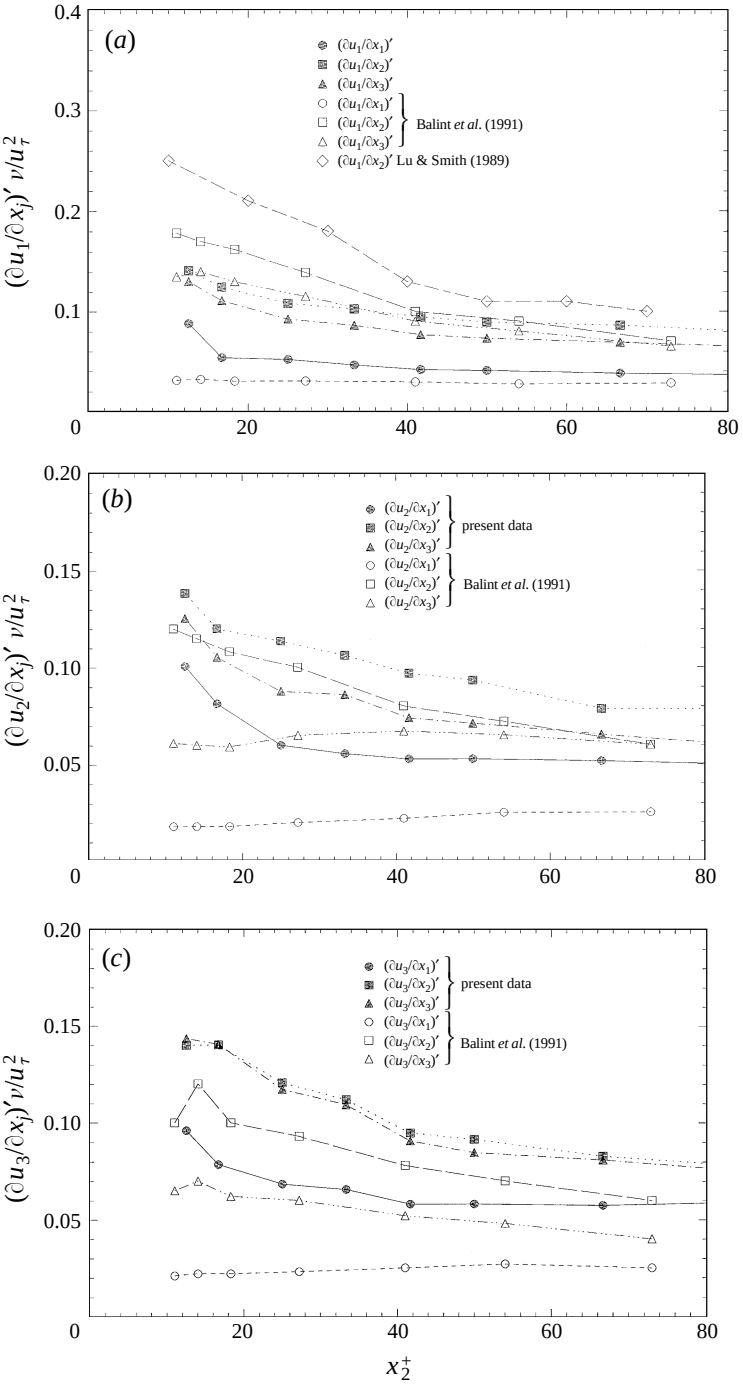

FIGURE 25. R.m.s. of fluctuations of spatial derivatives of velocity normalized by inner variables.

5.8. *Velocity gradient statistics*

Computed r.m.s. values of all three spatial derivatives of u_i, normalized by outer variables δ and u_τ are plotted in figures 24(*a*), 24(*b*) and 24(*c*). The streamwise derivatives of all three velocity components are observed to be much lower in the entire

boundary layer than those in the wall-normal and spanwise directions, which themselves are noticeably approximately equal.

For closer comparison these derivatives are normalized by the inner variables and the plots are shown in figures 25(*a*), 25(*b*) and 25(*c*). R.m.s. values of $\partial u_1/\partial x_3$ and $\partial u_1/\partial x_2$ are slightly lower than those of Balint *et al.* (1991); however, $\partial u_1/\partial x_1$ values are higher. The same trend is seen in the streamwise derivatives of u_2 and u_3 components, which can be explained in terms of how these derivatives are evaluated. The present data take into consideration not only the time derivative but also the other two derivatives in spanwise and normal directions ((2.11), (2.12) and (2.13)). The $\partial u_1/\partial x_2$ data of Lu & Smith (1988) are much higher than all the other results. The data of Balint *et al.* (1991) for $\partial u_2/\partial x_1$ and $\partial u_2/\partial x_3$ are considerably lower; however, $\partial u_2/\partial x_2$ values agree fairly well in the region $x_2^+ < 30$. Similar differences are noted for $\partial u_3/\partial x_1$ and $\partial u_3/\partial x_3$. The relatively large differences in $\partial u_3/\partial x_2$ and $\partial u_2/\partial x_3$ values when compared with those of Balint *et al.* (1991) are similar to those observed in the r.m.s. values of the streamwise component of vorticity fluctuations. This may be attributed to the larger acceptance cone of the probe which allows higher fluctuations of velocity components in the spanwise and normal directions to be validated which, subsequently, may lead to higher gradients of these velocity components.

5.9. *Spectra of velocity and vorticity components*

In order to analyse the distributions of fluctuating velocity and vorticity over the range of frequencies in the flow, the spectra of the three velocity and the three vorticity components are computed from the respective instantaneous data. The power spectral density (p.s.d.) plots of the three velocity components at the centre of the probe as a function of the streamwise wavenumber k_1 non-dimensionalized by the outer scale δ are shown in figure 26(*a*), 26(*b*) and 26(*c*). The streamwise wavenumber $k_1 = 2\pi f/U$ is computed with local axial mean velocity value as the convection velocity (Taylor's hypothesis). The data of Balint *et al.* (1991) are compared in these graphs for the wavenumber range of 10–250. The present data show good agreement, particularly for the u_3 component but are lower for u_2 and higher for u_1 in this range of wavenumbers. The higher spectral values of Balint *et al.* (1991) for the normal velocity component u_2 indicates that its r.m.s. value is significantly higher than that of the present experiment. This however is not the case, as the present r.m.s. values of u_2 are higher as seen in figure 13(*b*). Their results therefore seem to be inconsistent and hence it is difficult to explain significant disagreements between the two results for the u_2 component although both are normalized by the same scales. The slopes of the two spectra however, are approximately equal, which suggests that the present probe gives as good a resolution if not better for the smallest scales of turbulence near the wall. It appears that the spectra of axial and spanwise velocity fluctuations seem to collapse with the outer scale δ.

Figures 27(*a*), (27(*b*) and 27(*c*) show one-dimensional power spectra of the three vorticity components at the same wall-normal location of $x_2^+ = 12.5$ against the non-dimensional wavenumber on a log–log scale. The spectra of Balint *et al.* (1991) for the respective vorticity components but at $x_2^+ = 18$ are also superimposed. The slopes of the spectra of the streamwise and spanwise vorticity components seem to agree with those of Balint *et al.* (1991) although differences exist in the content of the spectra. The agreement is good in the wavenumber range 10–50 for the ω_2 but then their spectra drops off sharply for higher wavenumbers. For both axial and spanwise components the present values show much larger energy content, probably because the probe validates more velocity vectors at high pitch or yaw angles.

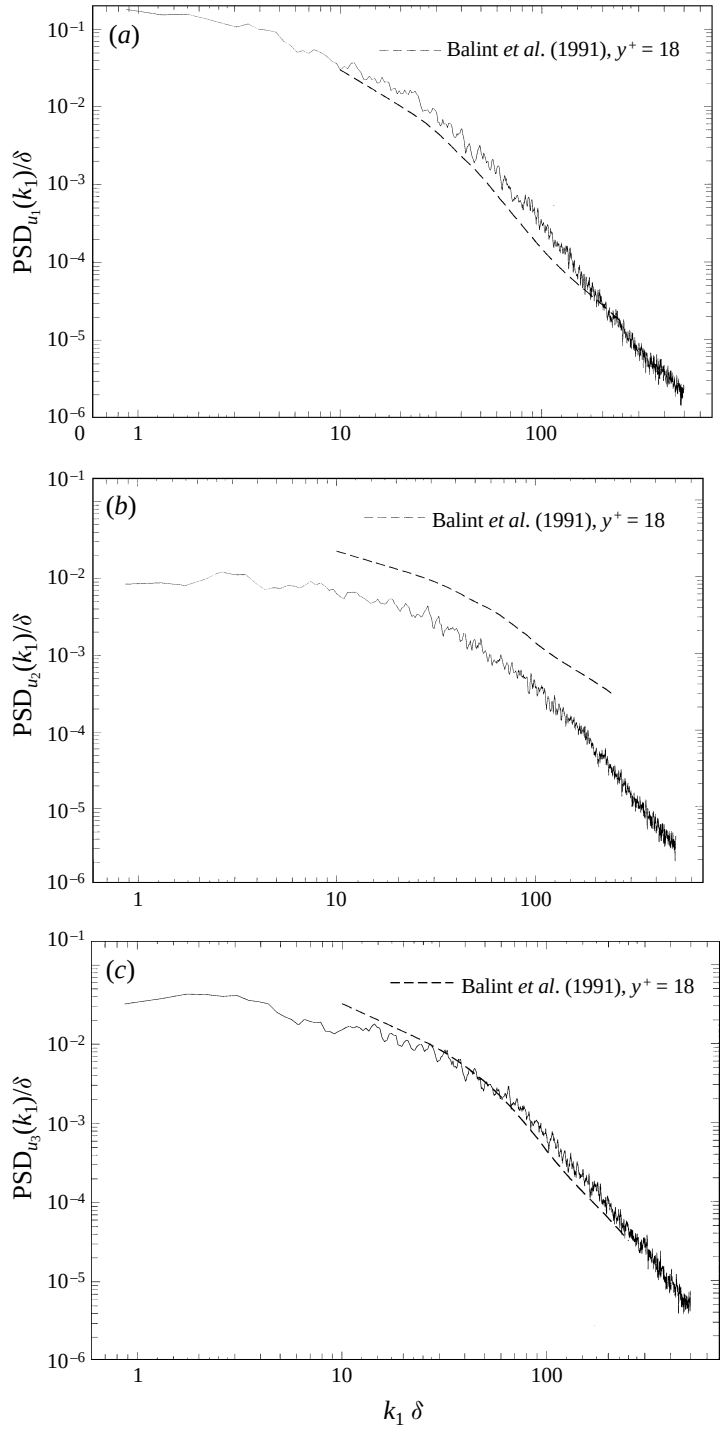

FIGURE 26. Power spectral density of (*a*) longitudinal, (*b*) normal and (*c*) spanwise velocity components at $x_2^+ = 12.5$.

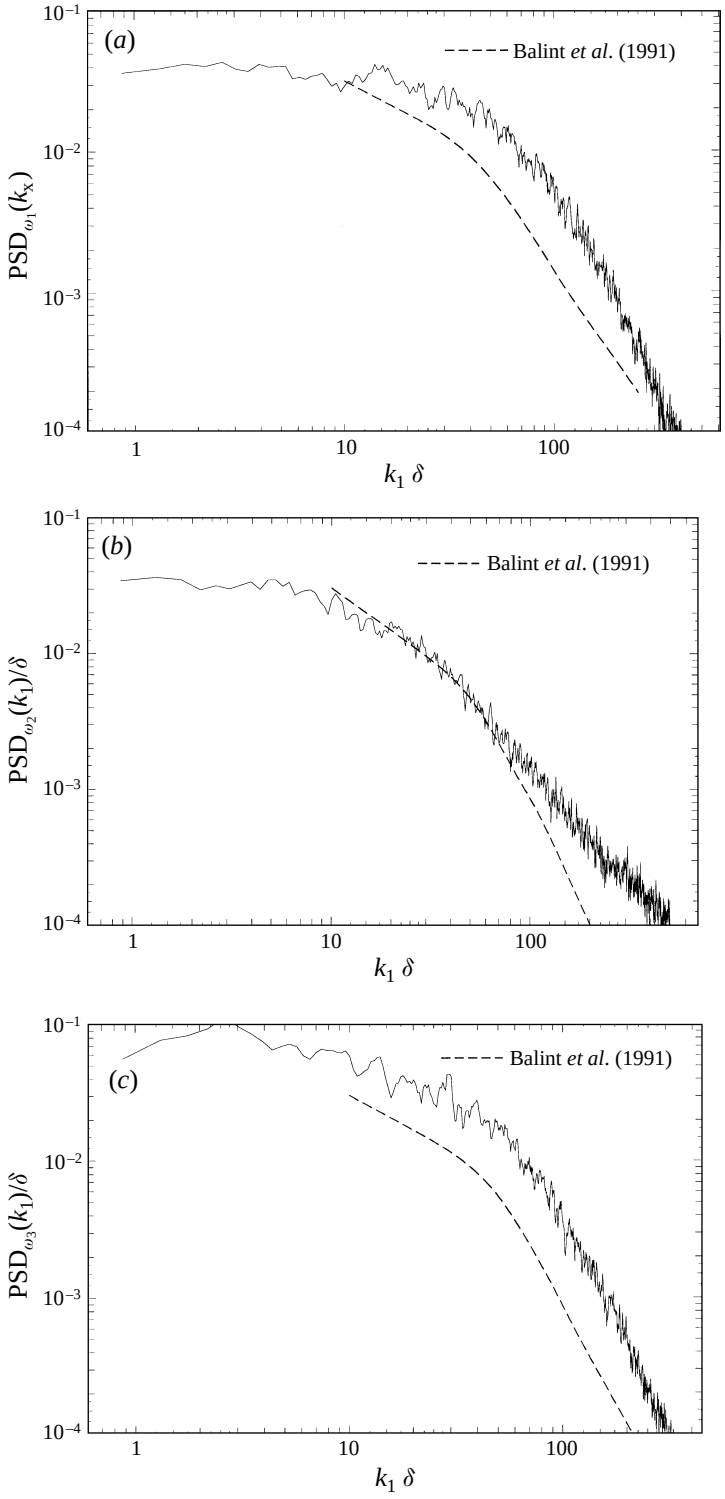

FIGURE 27. Power spectral density of (*a*) longitudinal, (*b*) spanwise and (*c*) components at $x_2^+ = 12.5$.

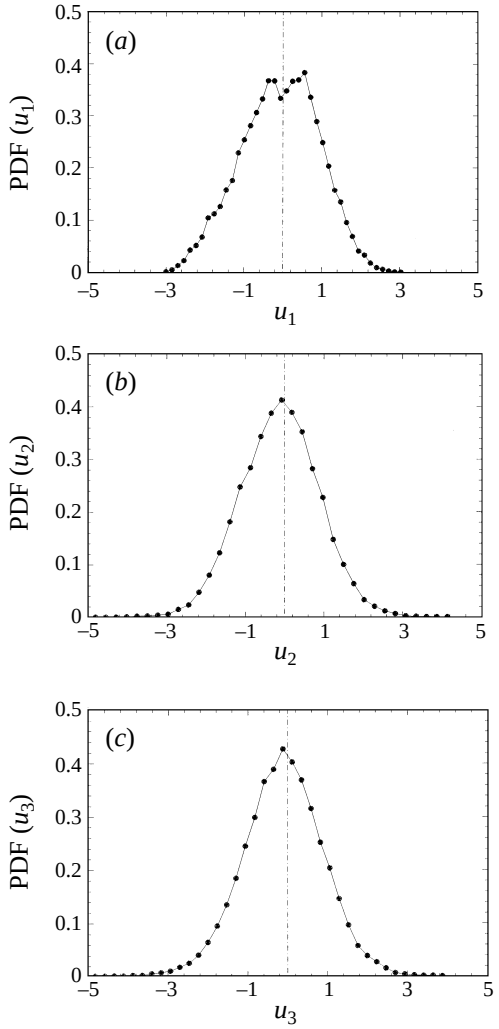

FIGURE 28(*a–c*). Probability density functions of velocity fluctuations at $x_2^+ = 12.5$. Abscissa in r.m.s. units.

5.10. *PDF distributions*

The probability distribution functions for axial, wall-normal and spanwise velocity components at the centroid of the probe are shown in figures 28(*a*), 28(*b*) and 28(*c*) at $x_2^+ = 12.5$. The abscissa values are expressed in terms of the corresponding r.m.s. values.

The *u*-component p.d.f. is more symmetric near the wall, which is reflected in its flatness factor, and the bimodal behaviour suggests a possible periodicity in the flow. The work of Andreopoulos *et al.* (1984) has also suggested a bimodal distribution of longitudinal velocity fluctuations in the near-wall region. A weak bimodality can be also observed in the p.d.f.s of Eckelmann (1974) at locations close to the edge of the viscous sublayer or just outside of it. Intermittent phenomena in the viscous sublayer which affect the buffer region may be responsible for this behaviour of the p.d.f.s.

Similarly, the normal component deviates from the Gaussian distribution and shows intense negative fluctuations, to the extent of five times its r.m.s. value, to occur

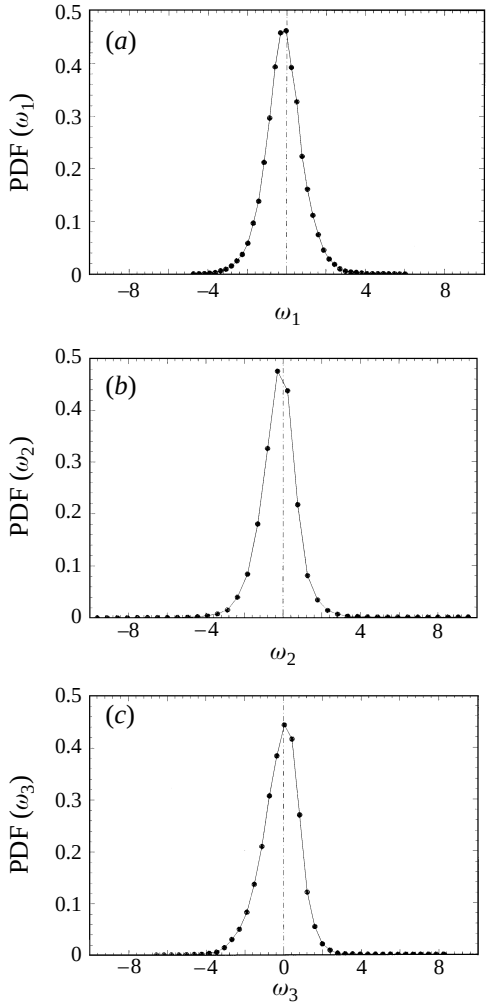

FIGURE 29(*a–c*). Probability density function of vorticity fluctuations at $x_2^+ = 12.5$. Abscissa in r.m.s. units.

although these events associated with intermittency are less frequent. The p.d.f. of the spanwise component indicates that positive events are as likely as negative ones and the close to zero value for the skewness of u_3 reflects the two-dimensional nature of the flow.

The probability distributions of all three vorticity components, as computed at the $x_2^+ = 12.5$ location are shown in figures 29(*a*), 29(*b*) and 29(*c*). It is evident that the dominant spanwise component is non-Gaussian as it is skewed to the negative while the axial component shows more random characteristics, with approximately zero skewness value, as seen in figure 29(*a*). The tails of p.d.f.s of ω_2 and ω_3 are noticeably longer than those of ω_1. It is intriguing to note, as these tails indicate, very large-amplitude deviations from the mean: as much as 8–10 times the respective r.m.s. values in wall-normal and spanwise vorticity occur in the viscous sublayer. The probability however of the occurrence of such violent eruptions is very small. Balint *et al.* (1991), however, found erroneous negative skewness for this ω_1 component as a result of positive bias of low-amplitude fluctuations. The normal component of vorticity is

observed to be skewed slightly towards negative but very large fluctuations of both positive as well as negative amplitude are equally likely to occur and contribute significantly to the high r.m.s. value at this location.

5.11. *Conditional sampling techniques*

To obtain further insight into the structural characteristics of the two predominant events, namely ejections and sweeps, which are associated with the near-wall turbulence, the time-dependent signals of all three vorticity components are interrogated using the conditional sampling technique as a tool for identifying these events. The projection θ_v of vorticity vector in the (x_1, x_2)-plane is investigated in particular first. This angle θ_v is defined as $\theta_v = \tan^{-1}(\omega_2/\omega_1)$ and is positive counterclockwise from the positive x_1-axis (see figure 30*a*). The detection of an event associated with the passage of a structure is triggered when the absolute value of the amplitude of the time series of ω_2 is above a pre-determined threshold level $k(\omega_2)_{rms}$ and the absolute value of the amplitude of the time series of ω_1 is above a pre-determined threshold level $k(\omega_1)_{rms}$. The probability distributions of these events conditioned with the threshold levels of 0, 50 and 100% of the r.m.s. value of ω_1 and ω_2 are shown in figure 30(*b*). They have been computed from the data obtained at $x_2^+ = 12.5$. The case with a value of $k = 0$ corresponds to unconditioned data. The first peak in the distribution of the p.d.f. appears to be at about $\theta_v = 10°$ while a second peak occurs at $\theta_v = -170°$. The distributions shown in this figure also demonstrate a periodicity with 180° period which is a result of the expected invariance of the results with respect to reflection of the spanwise axis x_3.

Moin & Kim (1985) carried out a similar analysis of the preferred angles of the vorticity vector in a large eddy simulation (LES) of a turbulent channel flow. Although in these simulations the effect of small-scale eddies which dominate the near wear-wall region is modelled, and therefore not directly calculated, their results also indicate a vortex line inclination at about 10° and $-170°$ in the near-wall, region.

Four distinct orientations with much higher probability can be noticed after conditioning the present data, which are otherwise obscured. The p.d.f.s show two primary peaks approximately at 35° and $-140°$, which are approximately 180° apart and two secondary peaks at $-35°$ and 140°. The primary peaks in the first ($0° < \theta_v < 90°$) and third ($-180° < \theta_v < -90°$) quadrants are associated with structures carrying either positive ω_1 or negative ω_1. It is very interesting to observe how the application of a minor threshold to the data changed the most probable inclination from 10° to 35°.

A similar analysis has been carried out for the projection of the vorticity vector on the (x_1, x_3)-plane. This angle ϕ_v is defined as $\phi_v = \tan^{-1}(\omega_3/\omega_1)$ and is positive in the clockwise direction from the positive x_1 axis towards the positive x_3 axis as shown in figure 30(*a*). The results are shown in figure 30(*c*). It should be noted that in this analysis the instantaneous values of all three components of vorticity were used, which for the case of ω_3, included the mean value. Thus the result of figure 30(*c*) for the unconditioned case with $k = 0$, which indicates that the most probable value of the vorticity inclination on the horizontal plane is about $-90°$ to the x_1 axis, is not a surprise. The conditional distributions, however, reveal two peaks in the third ($-180° < \phi_v < -90°$) and fourth ($-90° < \phi_v < 0°$) quadrants which suggest that the vector on this plane is orientated at $\phi_v = -135°$ and $\phi_v = -45°$. A typical hairpin or horseshoe vortex has one leg oriented at $-45°$ and a second one oriented at $-135°$. In order to investigate whether the results of figures 30(*b*) and 30(*c*) indicate the same structure, the distribution of the joint probability density function (j.p.d.f.) of the two inclinations ϕ_v and θ_v has been also considered. Figure 31(*a*) shows iso-probability

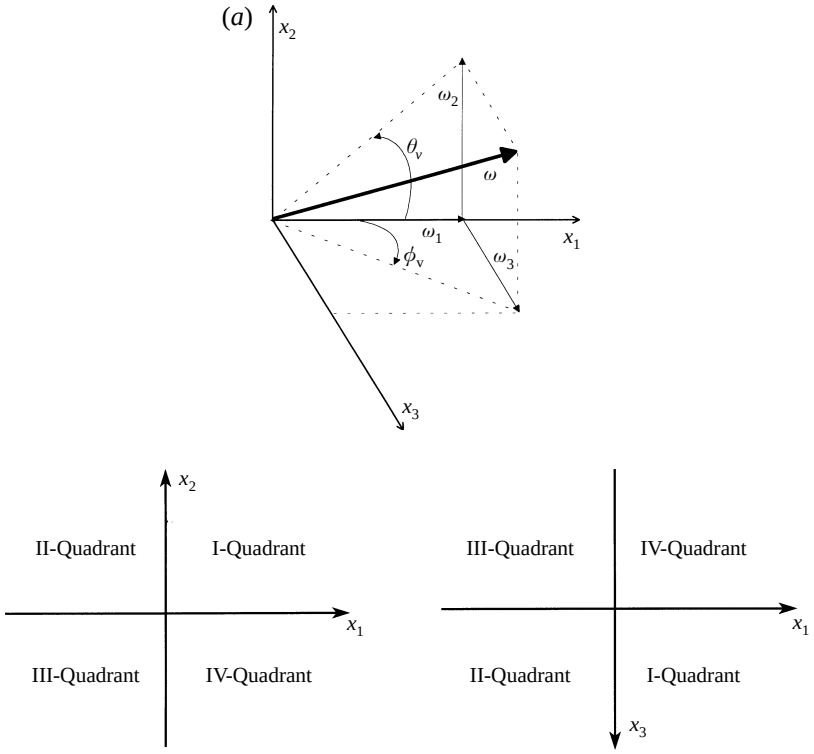

FIGURE 30(*a*). For caption see facing page.

contours of the j.p.d.f. of the unconditioned data. The ranges of these two angles were $-180° \leqslant \phi_v \leqslant 180°$ and $-90° \leqslant \theta_v \leqslant 90°$. These variations cover the entire domain uniquely and also determine the ranges of the eight octants which are also indicated in figure 31(*a*). It should be noted that the range of the independent variable θ_v has been reduced from the $-180° \leqslant \theta_v \leqslant 180°$ shown in figure 30(*b*) to $-90° \leqslant \theta_v \leqslant 90°$, which is the appropriate range to define the vorticity vector orientation in spherical coordinates. The upper four octants are characterized by $0° \leqslant \theta_v \leqslant 90°$ while the four lower octants correspond to $-90° \leqslant \theta_v \leqslant 0°$.

The results of figure 31(*a*) show that the domain with $-180° \leqslant \phi_v \leqslant 0°$, which represents all the data with $\omega_3 < 0$, contains regions of higher j.p.d.f. than any other region. In fact events with ($\theta_v \approx -90°$, $\phi_v \approx -90°$) and ($\theta_v \approx 90°$, $\phi_v \approx -90°$) show the highest probability of occurrence. Although the data of figure 30(*b*) show the first evidence that events with $\phi_v \approx -90°$ have very high probability of occurrence, the results of figure 30(*b*) do not directly reveal that events with $\theta_v \approx 90°$ or $-90°$ are of importance. Thus the j.p.d.f. provides more information and therefore it is more useful than the single-variable p.d.f. The peaks at $\pm 90°$ clearly demonstrate that these structures carry no longitudinal vorticity.

Secondary peaks in the distribution of j.p.d.f. can be observed in the regions with ($\theta_v \approx -30°$, $\phi_v \approx -135°$) and ($\theta_v \approx 20°$, $\phi_v \approx -45°$), in the VII and III octants respectively, which may be indicative of hairpin vortices inclined at about 20° to 30° to the wall.

The application of a conditioning threshold on all three components ω_1, ω_2 and ω_3, reveals some additional information. Figure 31(*b*) shows the j.p.d.f. of the conditioned data. The major characteristic is the appearance of rather narrow regions of relatively

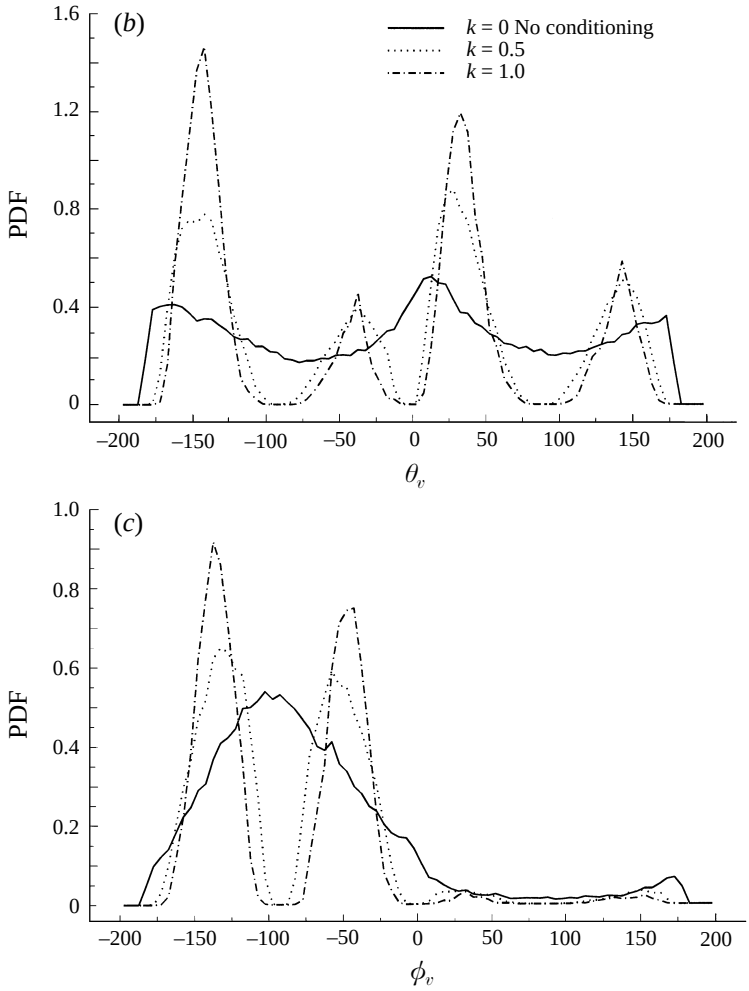

FIGURE 30. (*a*). Angular orientation of vorticity vector and definition of quadrants on vertical and horizontal planes. (*b*) Probability density function of vorticity vector orientation angle θ_v in the (x_1, x_2)-plane at $x_2^+ = 12.5$, for threshold levels 0, 0.5 and 1. r.m.s. of ω_1 and for ω_2. (*c*) Probability density function of vorticity vector orientation angle ϕ_v in the (x_1, x_3)-plane at $x_2^+ = 12.5$, for threshold levels 0, 0.5 and 1 r.m.s. of ω_1 and ω_3.

high probability indicating specific preferential directions of the vorticity vector during some violent events. Most notable are the regions defined by $-60° < \theta_v < -20°$ and $-180° < \phi_v < -120°$ in the VII octant and $20° < \theta_v < 60°$ and $-60° < \phi_v < 60°$ in the IV/I octants. Most of these activities are associated with $\phi_v < 0°$ which suggests that negative spanwise vorticity dominates these events.

Morrison *et al.* (1992) investigated the bursting mechanism in high-Reynolds-number turbulent boundary layer flows. They report that negative spanwise vorticity dominates ejections while positive vorticity is at least larger than that in ejections and it is associated with sweeps. In the light of this conjecture the primary peaks observed above may be associated with the burst/sweep sequence.

Other flow structures, however, may also have orientations similar to the preferred ones shown in figures 30 and 31. 'Hair-pin' or 'arch-like' vortices, for instance, are

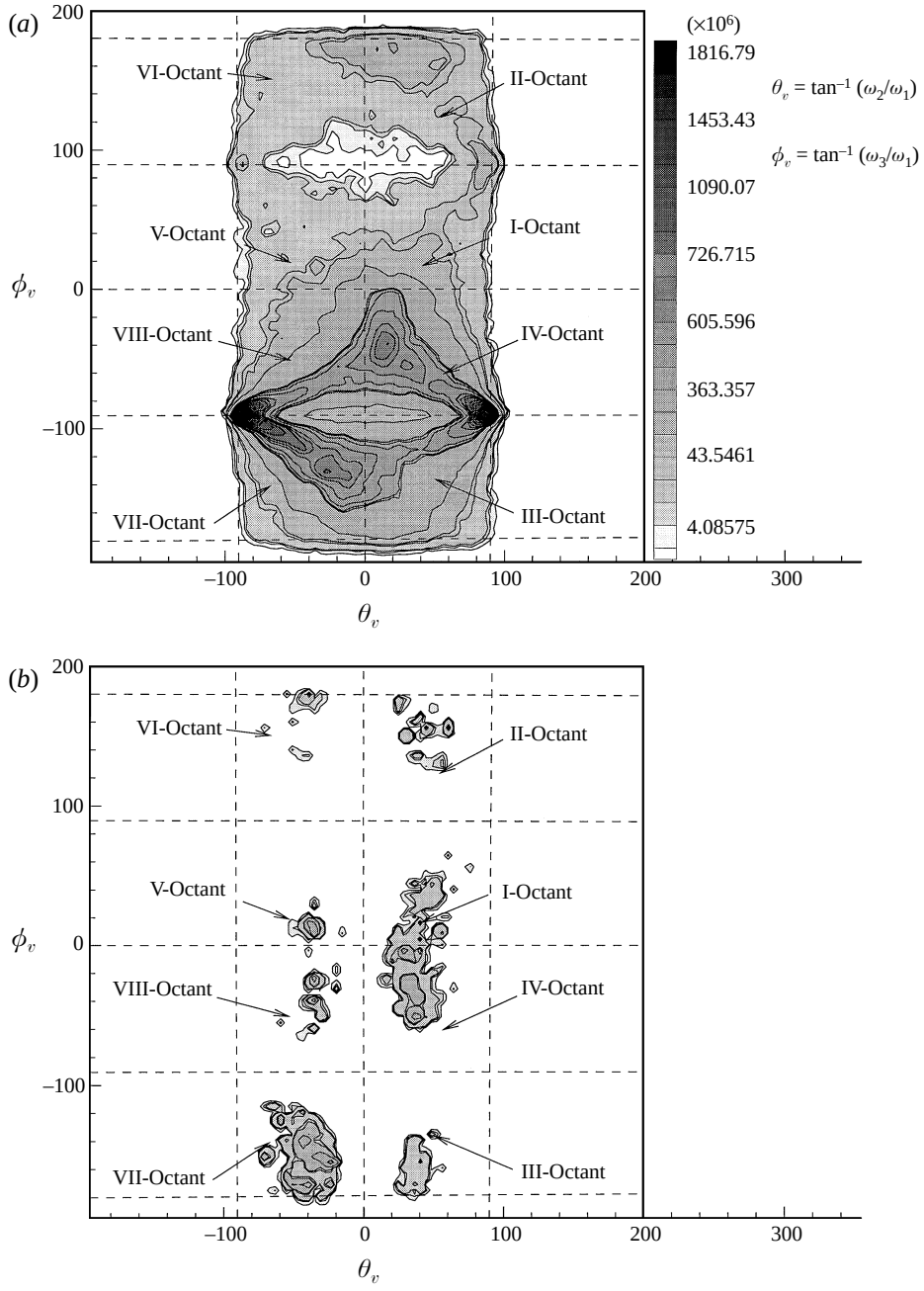

FIGURE 31. Joint probability of vorticity vector orientation angles. (*a*) Threshold level $k = 0$; (*b*) threshold level $k = 2$, ω_1, ω_2 and ω_3 components.

characterized by negative ω_3 everywhere in the vortex and positive ω_1 and ω_2 in one leg and negative ω_1 and ω_2 in the other. The peak at $\theta_v = 35°$ of figure 30(*b*) and the peak at $\theta_v = -35°$ of the same figure provide evidence in support of this notion. The flow visualization observations of Head & Bandyopadhyay (1981) also support the present findings. Single-point measurements of velocity or two-point correlations of velocity

made by other investigators have provided evidence that the structures are inclined at 10°. Our analysis of the unconditioned data has also indicated that there is a high probability of observing this inclination. However, as observed by Haidari & Smith (1994) and described by Smith & Walker (1995) the inclination of a hairpin vortex can vary from 10° in the most upstream part of the legs to 45° in the lifted part of the legs or to more than 45° at the tip of the vortex. The recent DNS data of Crawford & Karniadakis (1996), although at lower Reynolds number, also indicated a preferential direction of vorticity in the near-wall region of a developing asymmetric channel flow. Thus the vorticity vector inclinations measured in the present study are consistent with previous experimental observations and DNS results. The new information provided by the present results suggests that these orientation angles of the vorticity vectors are tied with those of hairpin vortex structures.

5.12. *Vorticity and rate-of-strain correlations*

Wallace, Balint & Ong (1992) in their analysis of the properties of helicity density with good spatial resolution $h = (\boldsymbol{V}\cdot\boldsymbol{\omega})/|\boldsymbol{V}||\boldsymbol{\omega}|$, $\boldsymbol{V}$ and $\boldsymbol{\omega}$ being velocity and vorticity vectors respectively, in turbulent boundary layer flow at $Re_\theta = 2685$ found that in the regions of high dissipation rate, e.g. near the boundaries, the velocity and vorticity vectors were nearly orthogonal and as the dissipation rate dropped the probability of these two vectors aligning increased significantly. Ashurst *et al.* (1987), on the other hand examined the coupling of vorticity and the three eigenvectors of the strain rate tensor for isotropic and homogeneous shear flows by numerical simulations. The matrix of strain rate tensor s_{ij}, being symmetric, has its eigenvectors orthonormal to each other and under incompressibility conditions the sum of all three eigenvalues is zero, satisfying the continuity. Their results indicated that vorticity pointed in the direction of intermediate extensive strain (corresponding to the middle positive eigenvalue of the strain rate matrix) which they attributed to the conservation principle of angular momentum. The present data at $x_2^+ = 12.5$ (where the flow is considered to be highly inhomogeneous and slightly anisotropic) was searched to identify if any such linkage between the eigenvectors and the vorticity vectors exists. Figure 32 shows the plot of the p.d.f. of the alignment of the vorticity vector with each of the three eigenvectors of the strain rate matrix obtained by computing all the terms through the spatial derivatives of velocity components. In this plot α_s, β_s and γ_s are the three eigenvectors associated with three real eigenvalues of the matrix formed by the strain tensor s_{ij}. The absolute value of the dot product of the unit vectors was used to determine the direction which varies from 90° to 0°. This graph shows the higher probability of the vorticity vector aligning with the middle eigenvector β_s and least it is likely to point in the direction of the most compressive strain (eigenvector corresponding to the most negative eigenvalue of the strain rate matrix). However, alignment of vorticity with the other two eigenvectors is more probable when vorticity is normal to either the α_s or γ_s direction.

The sign of $\nabla^2 p$ of equation (1.4) indicates whether the strain or vorticity dominates locally the dynamical processes. At $x_2^+ = 12.5$, the present measurements show that the ratio $\frac{1}{2}\overline{\omega_k^2}/\overline{(s_{ik}\, s_{ik})}$ has a value of 0.22 which suggests that on average the strain dominates the near-wall region. The data of Tsinober *et al.* indicated a value of this ratio of 0.32 obtained at $x_2/\delta = 0.2$. Another indication of the strong prevalence of the strain is the relative magnitude of the first two source terms in equation (5.3) $\overline{s_{ik}\, s_{kj}\, s_{ij}}/\frac{1}{4}\overline{\omega_i\, \omega_j\, s_{ij}}$ which at $y^+ = 12.5$ appears to be 22.

Although these time-averaged values may indicate the prevailing situation, the most

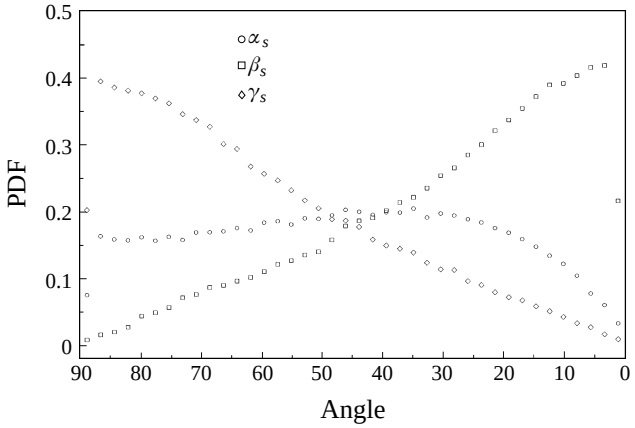

FIGURE 32. Probability density function of the alignment of the vorticity with each of the three eigenvectors α_s, β_s, and γ_s associated with the strain rate matrix.

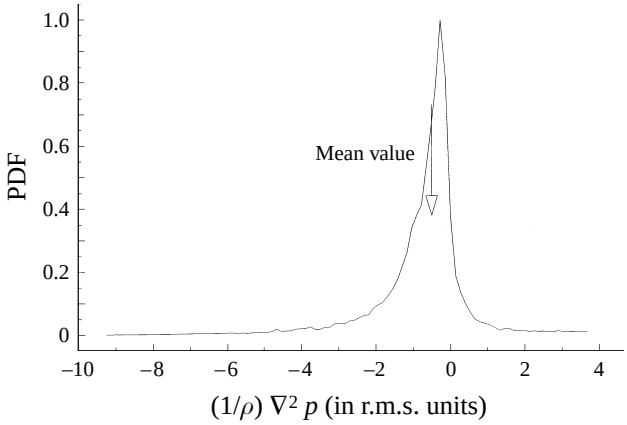

FIGURE 33. Probability density function of $(1/\rho)\nabla^2 p$.

significant dynamical processes may not be described by them because large fluctuations are associated with these quantities. For instance, the p.d.f. of $(1/\rho)\nabla^2 p$, shown in figure 33, is highly skewed in the negative direction. Negative excursions of the order of 9 r.m.s. in amplitude have been observed and not only the mean but also the most probable value of the distribution are negative, which is indicative of the dominance of the strain over rotation. It appears that enstrophy fluctuations dominate the dynamics of pressure fluctuations less frequently than the strain.

One general characteristic of all source/sink terms appearing in both transport equations (5.1) and (5.3) is that they fluctuate considerably about their mean. The ratio of r.m.s. to mean for the quantity $s_{ik}\,s_{ki}\,s_{ij}$ is -20 while for $\omega_i\,\omega_j\,s_{ij}$ it is 40. Consequently long-time averaging may mask some of dynamically important phenomena. Consider for instance, the time series of several of the terms of these transport equations, some of which can be considered as matrix invariants of the velocity gradient or strain-rate tensor (Soria *et al.* 1994), $\omega_j\,s_{lj}$, $(1/\rho)\nabla^2 p$, $s_{ij}\,s_{ij}$, $\omega_i\,\omega_j\,s_{ij}$ and $s_{ik}\,s_{ki}\,s_{ij}$ together with the shear stress $u_1\,u_2$ and ω_1 as shown in figure 34. All signals have been normalized by their corresponding r.m.s. It is very interesting to observe that

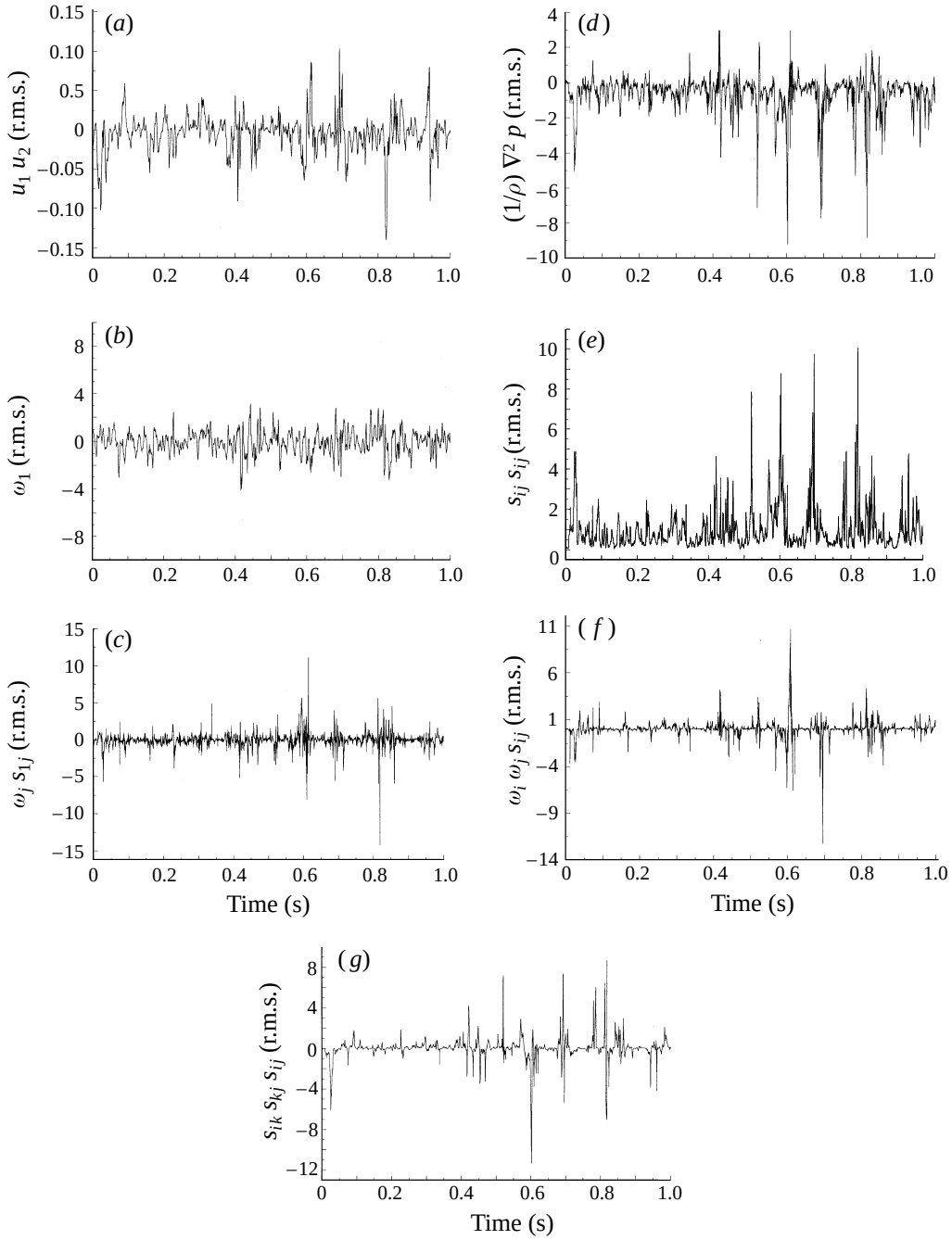

FIGURE 34. Typical signals of various quantities.

all these terms exhibit a very strong intermittent behaviour which is characterized by bursts of large amplitude, sometimes up to 10 r.m.s. values, followed by less violent periods. Several of these bursts are evident in all signals, suggesting that a specific flow phenomenon may be the common cause.

5.13. *Further analysis by conditional sampling techniques*

In order to further investigate the type of structures present in the flow the detection criteria of the conditional sampling procedure are now modified to distinguish high-amplitude events identified with strongly non-Gaussian strain and vorticity fluctuations and to explore correlations of strong and weak regions with all other measured flow quantities of importance to the dynamics of near-wall turbulence. In particular, besides the three velocity and three vorticity components, the stretching vector $\omega_k s_{ki}$, and the terms $\omega_i \omega_j s_{ij}$ and $s_{ij} s_{ij}$ were also considered. The signals were conditioned on the three vorticity components ω_1, ω_2 and ω_3, the two vorticity gradients at the wall, $\partial\omega_1/\partial x_2$ and $\partial\omega_3/\partial x_2$ and the stretching vector $\omega_k s_{ki}$ and $s_{ij} s_{ij}$ independently. The algorithm is made to lock on to that part of the signal to be conditioned, where the amplitude is above a given threshold k and counts as an 'event' of duration 50 time units above and below the reference time when the signal is at its local extreme. While this period is somewhat arbitrary it is equivalent to about 21 viscous time units, which is estimated to be the duration of the intense activity (see Haritonidis, Gresko & Breuer 1988). Thus all reference points are brought into alignment and the ensemble average of all such captured events is considered a candidate indicator of a 'typical structure'. A positive peak event is declared whenever the signal exceeds threshold k and a negative peak event when the signal is less than $-k$. The number of events accumulated by this technique is dependent directly on the value of the threshold k set during the pass but these events, at least in a qualitative sense, are believed to focus on the same feature in the flow. This detection method has been previously used by Her (1986) to detect high-amplitude pressure peaks and by Haritonidis *et al.* (1988). This algorithm is different from the commonly employed VITA (Variable Interval Time Averaging) technique of Blackwelder & Kaplan (1976) in which an event is counted when the short-time r.m.s. value of the signal is either above or below a predetermined value. Thus the VITA technique detects structures mostly with positive and negative amplitude, i.e. forces a change of sign, while the present detection technique avoids this type of biasing. This is a substantial difference between the two techniques and it should be taken into account when interpreting the results. In other words, when a typical structure obtained by the VITA technique contains a change of sign is not a surprise. However, when the peak detection technique yields a typical structure with a sign change it indicates that this type of structure really dominates over many others.

The ensemble-averaged values of fluctuations above their corresponding long time mean are normalized by the r.m.s. value of the respective quantity and the time units are normalized by the viscous time ν/u_τ^2 before they are plotted. The negative abscissa is interpreted as downstream and positive as upstream with respect to the measuring location. The conditioned results are analysed and compared to the dynamic events of streak formation, ejection, bursts and sweeps. It should be mentioned that a variety of structures, all related to the mechanism of turbulence, named for their shape and size, e.g. horseshoe, hairpin, pancake/surfboard eddies, arrowhead eddies etc., have been hypothesized in the extensive literature on the boundary layer flows. (See e.g. Perry, Lim & Teh 1981; Landahl 1984; Blackwelder & Haritonidis 1983).

Shown in figures 35(*a*) and 35(*b*) are some of the ensemble averages conditioned on positive thresholds of ω_1 for $k = 2\,(\omega_1)_{rms}$ and $k = -2\,(\omega_1)_{rms}$ respectively, obtained at $x_2^+ \approx 12.5$. Results conditioned on ω_2 and ω_3 can be found in Honkan (1994). The discussion is based mainly on the conditioning results for the two extreme values of $k = \pm 2$ with the assumption that the typical structures identified are the strongest. It was noted, however, that the results for other values of k exhibited similar qualitative

variation in general. The conditioning process is expected to extract the coherent content from the stochastic background because the events are averaged after the mean value is subtracted. The turbulent structures associated with ω_1 seem to be of longer duration than those associated with the other two components of vorticity when conditioned on ω_1. The velocity gradient $\partial u_3/\partial x_2$ dominates over $\partial u_2/\partial x_3$ and thus accounts for most of the contributions to the streamwise vorticity ω_1 near the wall, and at the wall its second derivative $\partial^2 u_3/\partial x_2^2$ is directly proportional to the spanwise pressure gradient $\partial p/\partial x_3$. Therefore these ω_1 events, which are rather intense since the effect of suppressed mean ω_1 is minimal, may also be associated with the passage of strong localized shear layers generated by the gradient $\partial u_3/\partial x_2$. They are reported to be more prevalent near the outer edge of the viscous sublayer ($x_2^+ \approx 15$), finally rolling up to form streamwise vortical structures. The high values of ω_1 fluctuations have also been reported by Kasagi *et al.* (1995) to be linked to the streamwise streak formation and regions of low pressure. The spanwise vorticity ω_3 is noticeably inactive and mostly negative but the normal component ω_2 shows a small and sharp peak at the same time as that of ω_1 and the structure therefore is considered to be sheet like (in the x_1, x_2-plane). This typical structure, recognized by ensemble averaging for $k = 2$, appears to be tilted upwards by about 16° and moving away from the wall ($u_2 > 0$, shown in figure 35*c*). The decreasing u_1 at the same time is suggestive of 'bursting' phenomena while sweeping motions are observed with these structures for $k = -2$ (figure 35*d*), which are inclined towards the wall at about 10° and appear to be moving towards the wall ($u_2 < 0$) with strong negative streamwise vorticity, eventually affecting the turbulent shear stress which shows a sharp negative peak. This event may also be viewed as one of the legs of the hairpin model being lifted up or it may be an isolated longitudinal vortex. This notion is supported by the fact that the spanwise velocity component u_3 shows the reversal of sign while $u_1 u_2$ reaches very high negative values for $k = 2$ and ω_3 is negative for both $k = 2$ and $k = -2$. The turbulent shear stress also has a distinct negative peak for $k = -2$.

Figures 35(*e*) and 35(*f*) show the term $\langle s_{ij} s_{ij} \rangle$, the three stretching components $\langle \omega_k s_{k1} \rangle$, $\langle \omega_k s_{k2} \rangle$, $\langle \omega_k s_{k3} \rangle$ and the enstrophy-generating term $\langle \omega_i \omega_j s_{ij} \rangle$. The 'dissipation' term $\langle s_{ij} s_{ij} \rangle$ remains positive during the duration of both events and peaks at $T^+ = 0$. This analysis also establishes a link between the conditioning vorticity component ω_1 and the stretching component $\omega_k s_{k1}$. If the viscous term in equation (1.2) is ignored, then the rate of change of vorticity $\langle \mathrm{D}\omega_i/\mathrm{D}t \rangle$ is directly affected by the stretching term $\langle s_{ik} \omega_k \rangle$. Considerable stretching is present during the $\omega_1 > 0$ events and compression of vortex lines is evident during the peak of strong $\omega_1 < 0$ events. Thus the application of any stretching is immediately evident in the corresponding vorticity component which itself contains the cumulative effect of the rate of change $\langle \mathrm{D}\omega_i/\mathrm{D}t \rangle$. It is interesting to observe that the enstrophy-generating term $\langle \omega_i \omega_j s_{ij} \rangle$ is negative, i.e. below its long-time mean during these events.

It is apparent that the normal gradient $\partial u_1/\partial x_2$ is the dominating term for ω_3 near the wall and its spatial gradient term $\partial^2 u_1/\partial x_2^2$ strongly correlates with the axial pressure gradient $\partial p/\partial x_1$. The vorticity flux $\partial \omega_3/\partial x_2$ is thus expected to exhibit this correlation. The signatures of wall pressure p, vorticity fluxes at the wall $\partial \omega_1/\partial x_2$ and $\partial \omega_3/\partial x_2$, vorticity components ω_i, velocities u_i, along with the turbulent shear stress $-u_1 u_2$ when conditioned on $\partial \omega_3/\partial x_2$ for $k = 1.5$ are shown in figures 36(*a*), 36(*b*) and 36(*c*). It should be noted that the Entran module for wall pressures/vorticity flux measurements was placed approximately 12.5 mm ($\frac{1}{2}$ in.) upstream of the vorticity probe so that the measurements by the pressure sensors are not adversely affected by the probe disturbance and interference. This difference in the position translates to about $+8$

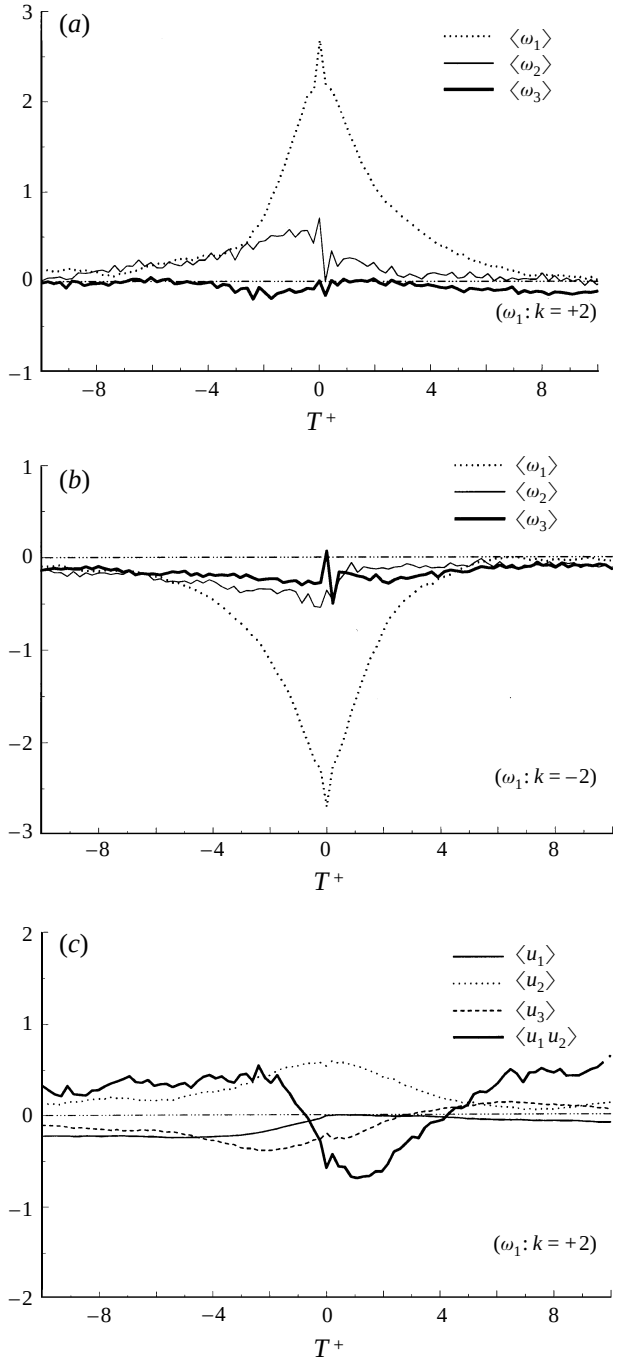

FIGURE 35(*a–c*). For caption see facing page.

viscous time units for the patterns of wall pressure and the two vorticity fluxes to reach the hot-wire position in the conditional results. The vorticity flux data should be interpreted as the vorticity shed off the solid wall and sensed, to a first-order approximation, at a nearby point inside the flow at a distance Δx_2 from the wall as

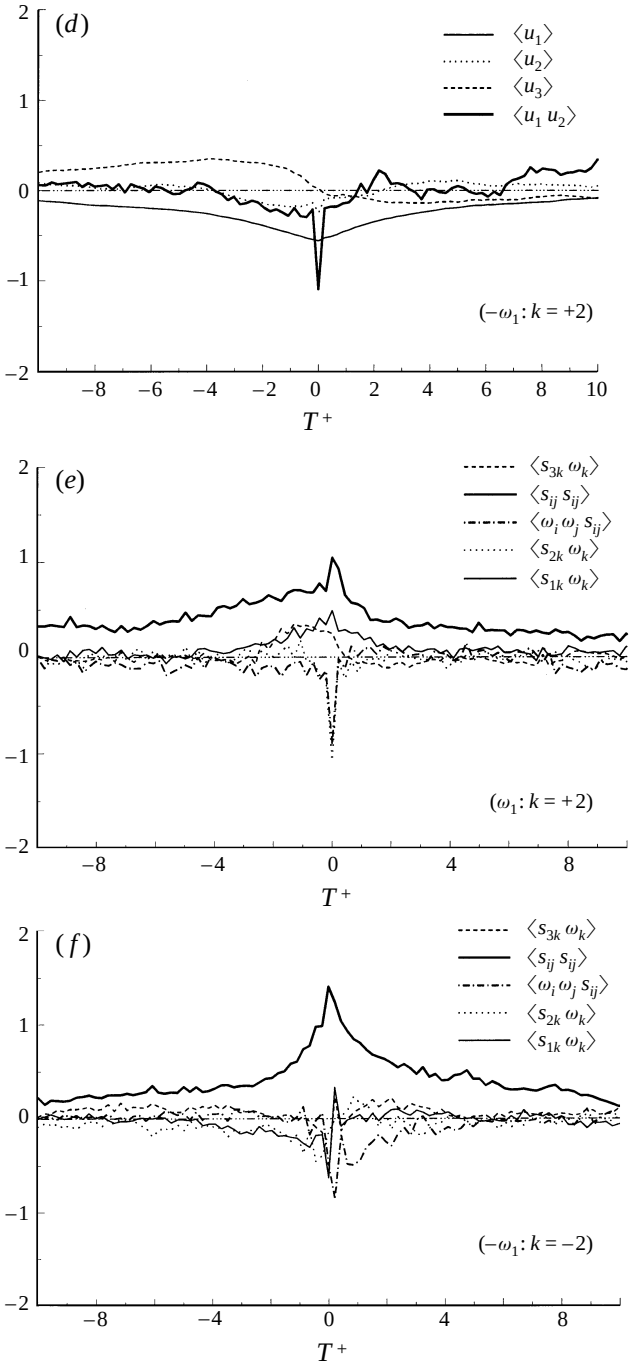

FIGURE 35. Conditional-averaged patterns based on ω_1.

$$\Delta\omega_3 = -\left[\frac{\partial\omega_3}{\partial x_2}\right]_w \Delta x_2, \quad \Delta\omega_1 = -\left[\frac{\partial\omega_1}{\partial x_2}\right]_w \Delta x_2.$$

The pressure data demonstrate distinct peaks when conditioned on $\partial\omega_3/\partial x_2$ The

regions of intense spanwise vorticity presumed to be related to the tails of the hairpin vortices thus illustrate strong correlation with wall pressure event.

5.14. *Bursts and sweeps*

The data shown in figures 36(*a*), 36(*b*) and 36(*c*) indicate that the local maxima/minima of pressure occur at the same time $T^+ = 0$ as the maxima of $\langle \partial\omega_3/\partial x_2 \rangle$. Since the pressure leads velocity and vorticity data the effects attributed to active events of spanwise vorticity flux in any of the three vorticity components are visualized with a time delay. In fact the conditional results on $\partial\omega_3/\partial x_2$ show that vorticity $\Delta\omega_1$, and $\Delta\omega_3$ shed off the wall at $T^+ = 0$ is in phase with the vorticity sensed at $T^+ = 8$. The work of Andreopoulos & Agui (1996) established that sweeps are associated with a very rapid rise with time of $\langle \partial\omega_3/\partial x_2 \rangle$ and that ejections are distinguished by the fast drop with time of the same quantity. It was also postulated that sweeps and ejections may share one common vortex lobe. The large value of positive $\langle u_2 \rangle$ shown in figure 36(*c*) at $T^+ = 8$ indicates the passage of ejections which may have been formed shortly after $T^+ = 0$, as shown by the rapid drop of $\langle \partial\omega_3/\partial x_2 \rangle$.

When the signals are conditioned on $\omega_3 > 0$ the passage of structures of rather short duration is detected. Figure 37(*a*) shows the ensemble-averaged values of the three vorticity components. These averages are above their corresponding long-time mean value, which for the spanwise component is -0.6 r.m.s. units. If this long-time mean is added to the $\langle \omega_3 \rangle$ then the pattern of ω_3 will have s substantial part with negative values immediately after $T^+ = 0$ in the positive direction. The $\langle u_2 \rangle$ pattern of figure 37(*b*) reveals that during the time $-1 < T^+ < 1$ the normal velocity component suddenly drops while u_1 remains negative. This configuration is a typical behaviour of sweeps, which are usually characterized as high-momentum fluid, evident here by the large excursion of $\langle u_1, u_2 \rangle$, moving towards the wall. Morisson, Subramanian & Bradshaw (1992) by using the VITA technique postulated that sweeps are inverted mushroom vortices moving towards the wall which are toppled by the mean vorticity to form an ejection further downstream. The present results, although based on different conditioning techniques, confirm that sweeps are distinguished by ω_3 vorticity sharply decreasing with time. In addition, the present results show that $\langle \omega_1 \rangle$ is negligible and that $\langle \omega_2 \rangle$ has values very close to $\langle \omega_3 \rangle + \bar{\omega}_3$ suggesting there is considerable tilting of the structure towards the x_2-direction, of the order of 45°. It is also interesting to observe that the dissipation term $\langle s_{ij} s_{ij} \rangle$ is maximum at $T^+ = 0$ and that the two components of the stretching vector $\langle \omega_k s_{k2} \rangle$, $\langle \omega_k s_{k3} \rangle$ are opposite in sign to that of the two vorticity components $\langle \omega_2 \rangle$, $\langle \omega_3 \rangle$, indicating that there is considerable compression of vorticity during sweeps.

The patterns shown in figures 38(*a*), 38(*b*) and 38(*c*) are the outcome of conditioning the results on $\omega_3 < 0$ The sudden increase of $\langle u_2 \rangle$ at about the origin and the low value of $\langle u_1 \rangle$ strongly suggest the presence of ejections in the flow pattern. The presence of a positive stretching component $\langle \omega_k s_{k3} \rangle$ throughout the entire event further intensifies the negative $\langle \omega_3 \rangle$. Thus, it appears that during ejections negative spanwise vorticity is amplified while longitudinal vorticity remains very small. The data also show that the normal component of vorticity reaches relatively large negative values at $T^+ = 0$ when a sudden eruption takes place as the result of significant stretching by the component $\langle \omega_k s_{k2} \rangle$, which is sizeable.

6. Conclusions

The basic statistical properties of velocity and vorticity fields computed from the measurements by the miniature probe in the boundary layer experiments are consistent

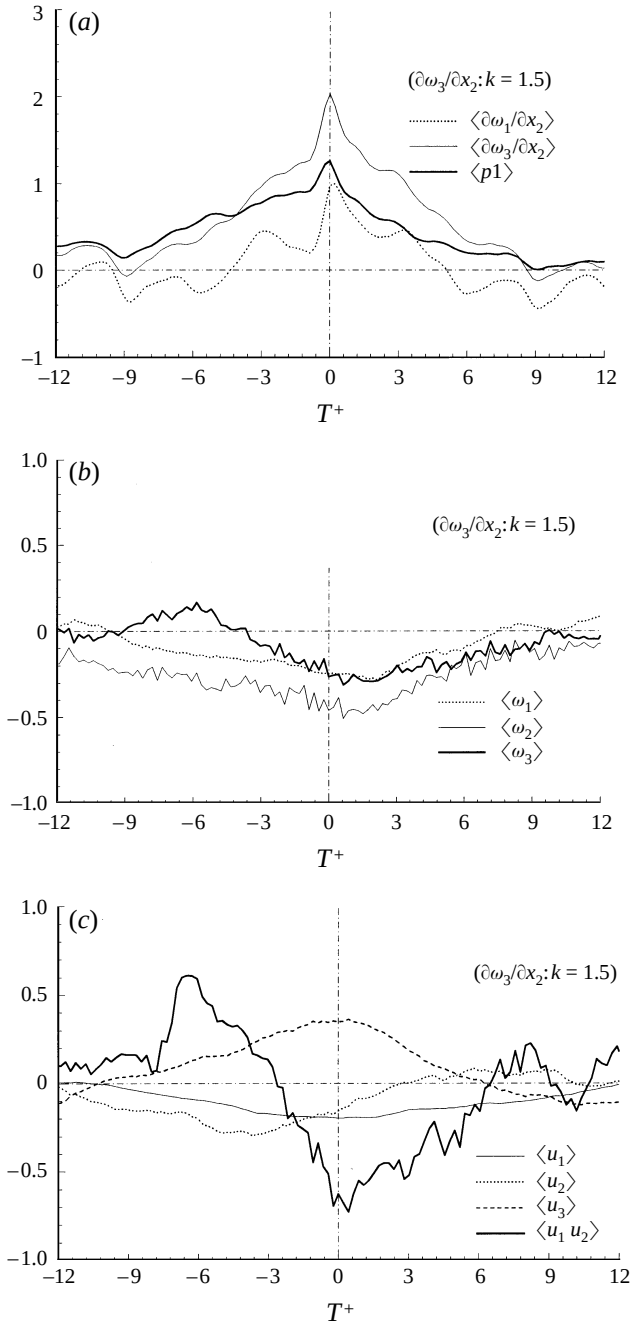

FIGURE 36. Conditional averaged patterns based on $\partial\omega_3/\partial x_2$.

with the existing datasets obtained in different facilities, under different conditions and for a wide range of spatial resolution and, more importantly, confirmed the recent results of Balint *et al*. (1991). In particular, their demonstration for the first time of the shift of maximum energy to higher wavenumbers by comparing the spectra of velocity and vorticity is strongly supported by the similar shift noted in the spectra of enstrophy and turbulent kinetic energy of the present flow at comparable Reynolds number.

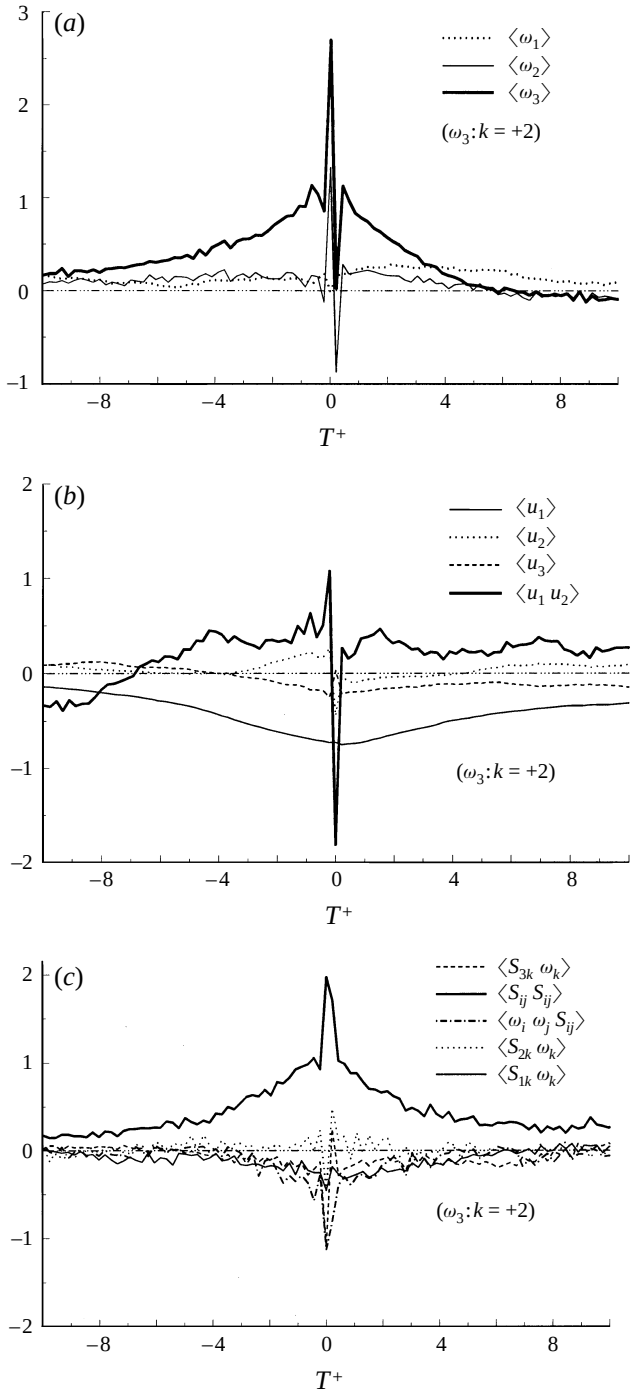

FIGURE 37. Conditional-averaged patterns based on $\omega_3 > 0$.

Further, the probability density distributions of all three fluctuating vorticity components also confirmed those of Balint *et al.* (1991), especially the distinct long tails in the p.d.f.s of ω_2 and ω_3. Statistics of velocity and vorticity fluctuations are in reasonable agreement with the results of Balint *et al.* (1991). Some deviations of the

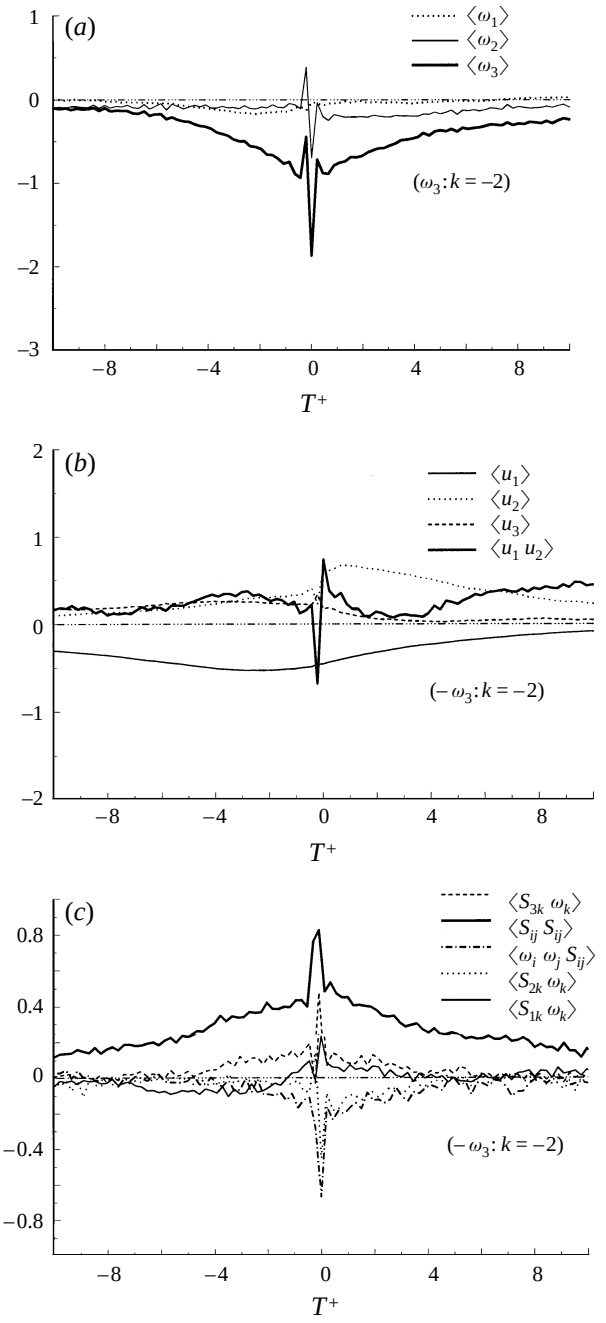

FIGURE 38. Conditional averaged patterns based on $\omega_3 < 0$.

individual velocity gradients can be explained in terms of key differences between the present probe and the one used by Balint *et al.* (1991), as listed below.

(*a*) The present probe does not use a common prong and therefore permits the electronic operation of each sensor independently.

(*b*) The probe, because of its different geometry, has a 'cone of validity' of instantaneous velocity vectors much larger than that of Balint *et al.* (1991) which has

one wire inclined 45° to the plane formed by the other two, whereas the present probe has the same wire inclined at 90° since each of the three wires are mutually orthogonal.

(*c*) Each sensor of the nine-wire probe could be operated at higher overheat ratios which allowed variations of yaw and pitch responses of each wire to be taken into account, which are intrinsically unique for each sensor.

(*d*) The streamwise velocity terms of normal and spanwise vorticity have been more accurately estimated by computing all the terms of Taylor's hypothesis.

One of the major observations is that the profiles of higher moments of velocity and vorticity did not collapse under a variety of different scales attempted, indicating the difficulty of choosing proper scaling parameters which has been reported by other researchers.

In addition to the confirmation of the flow properties reported by Balint *et al.* (1991) of turbulent boundary layers, in this investigation the following new results have been obtained.

(i) The profiles of flow yaw and pitch angles θ_f and ϕ_f in the near-wall region and their probability density distributions at $y^+ = 12.5$ indicate rather rare but intense fluctuations of the velocity vector orientation.

(ii) The probability density distributions of the orientation of vorticity vectors in the plane parallel to the wall reveal preferential directions when conditioned at various threshold levels of $(\omega_3)_{rms}$. These are believed to be associated with bursts and sweeps and the hairpin-like vortices formed in the near wall. The results of the joint probability distribution of the vorticity vector orientation angles, shown for the first time, indicate that the angles may be tied to those of hairpin vortex structures.

(iii) The conditional properties of the simultaneous measurements of wall pressures, the three components of velocity and vorticity and the two wall-normal gradients of axial and spanwise vorticity are investigated for the first time. They identify structures near the wall which are almost always associated with positive and negative spanwise vorticity of comparable magnitude. The pressure peaks, reported to be strongly related to the near-wall shear layer and the wavy patterns associated with buffer region flow instability, (Haritonidis *et al.* 1988) were also observed in these results.

(iv) The relationship of the strain rate matrix and vorticity vector showed the vorticity vector at the position closest to the wall to be least likely to align with the most compressive eigenvector of the strain rate matrix. The modified conditioning technique in a limited sense revealed some of the complex structural characteristics of turbulence mechanisms near the wall.

(v) The results on vorticity flux statistics confirmed the previous measurements obtained by Andreopoulos & Agui (1996) and extended their Re_θ range.

(vi) Several matrix invariants, $(1/\rho)\nabla^2 p$, $s_{ij}s_{ij}$, $\omega_i\omega_j s_{ij}$ and $s_{ik}s_{ki}s_{ij}$, were considered in the analysis together with the stretching $\omega_j s_{1j}$, shear stress $u_1 u_2$ and ω_1, ω_2, ω_3. All these invariants exhibit a very strong intermittent behaviour which is characterized by bursts of large amplitude, occasionally up to 10 r.m.s. values, followed by less violent periods. It appears that the strain dominates the fluctuations of pressure more than enstrophy.

(vii) The present results also demonstrated experimentally the effects of the stretching vector on vorticity. The application of stretching was found to immediately affect vorticity.

The financial support of the National Science Foundation is gratefully acknowledged. The authors are grateful to John Foss for helpful discussions and comments. Suggestions and recommendations made by the referees are also appreciated.

REFERENCES

AGUI, J. H. & ANDREOPOULOS, J. 1994 Development of a New LASER Vorticity Probe-LAVOR. *Fluids Engineering Div., Intl Symp.* on *LASER Anemometry*. Lake Tahoe NV, June 20–24 (ed. T. Huange & M. Otugen) ASME FED vol. 191, pp. 11–19.

ANDREOPOULOS, J. 1983*a* Improvements of the performance of triple hot wire probes. *Rev. Sci. Instrum.* **54**, 733–740.

ANDREOPOULOS, J. 1983*b* Statistical errors associated with turbulence intensity and probe geometry in hot-wire anemometry. *J. Phys.* E, *Sci. Instrum.* **16**, 1264–1271.

ANDREOPOULOS, J. & AGUI, J. H. 1996 Wall-vorticity flux dynamics in a two-dimensional turbulent boundary layer. *J. Fluid Mech.* **309**, 45–84.

ANDREOPOULOS, J., DURST, F., ZARIC, Z. & JOVANOVIC, J. 1984 Influence of Reynolds number on characteristics of turbulent wall boundary layers. *Exps. Fluids* **2**, 7–16.

ANDREOPOULOS, J. & WOOD, D. 1982 The response of a turbulent boundary layer to short length of roughness. *J. Fluid Mech.* **118**, 143–164.

ANTONIA, R. H., ZHU, Y. & KIM, J. 1993 On the measurement of lateral velocity derivatives in turbulent flows. *Exps. Fluids* **15**, 65–69.

APOSTOL, M. 1981 *Calculus*. McGraw Hill.

ASHURST, W. T., KERSTEIN, A. R., KERR, R. M. & GIBSON, C. H. 1987 Alignment of vorticity and scalar gradient with strain rate in simulated Navier–Stokes turbulence. *Phys. Fluids* **30**, 2342–2353.

BALINT, J.-M., VUKOSLAVČEVIĆ, P. & WALLACE, J. M. 1988 The transport of enstrophy in a turbulent boundary layer. In *Near Wall Turbulence 1988 Zoran Zaric Memorial Conf.* (ed. S. J. Kline & N. H. Afgan), pp. 932–950. Hemisphere.

BALINT, J., WALLACE, J. M. & VUKOSLAVČEVIĆ, P. 1991 The velocity and vorticity vector fields of a turbulent boundary layer. Part 2. Statistical properties. *J. Fluid Mech.* **228**, 53–86.

BLACKWELDER, R. F. & ECKELMANN, H. 1979 Streamwise vortices associated with the bursting phenomenon. *J. Fluid Mech.* **94**, 577–594.

BLACKWELDER, R. F. & HARITONIDIS, J. H. 1983 Scaling of the bursting frequency in turbulent boundary layers. *J. Fluid Mech.* **132**, 87–103.

BLACKWELDER, R. F. & KAPLAN, R. E. 1976 On the wall structure of the turbulent boundary layer. *J. Fluid Mech.* **76**, 89–112.

BRADSHAW, P. 1971 *Introduction to Turbulence and Its Measurements*. Pergamon.

BRADSHAW, P. & HUANG, G. P. 1995 The law of the wall in turbulent flow. *Proc. R. Soc. Lond.* A **451**, 165–188.

BREDERODE, V. & BRADSHAW, P. 1974 Influence of side walls on the turbulent centre-plane boundary layer in a square duct. *Trans. ASME J. Fluids Engng* **100**, 98–104.

BRUNS, J., DENGEL, P. & FERNHOLZ, H. H. 1992 Mean flow and turbulence measurements in an incompressible two-dimensional boundary layer. Part I: Data. *Hermann-Föttinger-Institut für Thermo- und Fluiddynamik, Technische Universität Berlin*, Rep. 02/92.

CHANG, P. H., ADRIAN, R. J. & JONES, B. G. 1983 Comparison between triple-wire and x-wire measurement techniques in high intensity turbulent shear flows. *8th Biennial Symp. on Turbulence, University of Missouri-Rolla*.

COLES, D. E. 1962 'The turbulent boundary layer in a compressible fluid. In Appendix A: A manual of experimental boundary layer practice of low speed flow. *Rand Rep.* R403-PR., ARC 24473.

CRAWFORD, C. & KARNIADAKIS, G. 1996 Shear stress modification and vorticity dynamics in near-wall turbulence. *Rep.* CFM 96-2. Brown University.

DUSSAUGE, J. P., FERNHOLZ, H., SMITH, R. W., FINLEY, P. J., SMITS, A. J. & SPINA, E. F. 1996 Turbulent boundary layers in subsonic and supersonic flow. *AGARD* AG-335.

ECKELMANN, H. 1974 The structure of the viscous sublayer and the adjacent wall region in turbulent channel flow. *J. Fluid Mech.* **65**, 439–549.

FOSS, J. F. & WALLACE, J. M. 1989 The measurement of vorticity in transitional and fully developed turbulent flows. In *Advances in Fluid Mechanics Measurements* (ed. M. Gad-el-Hak). Lecture Notes in Engineering, vol. 45. Springer.

Gad-el-Hak, M. & Bandyopadhyay, R. P. 1994 Reynolds number effects in wall bounded turbulent flows. *Appl. Mech. Rev.* **47**, 307–000.

George, W. K. & Hussain, H. J. 1991 Locally axisymmtric turbulence. *J. Fluid. Mech.* **233**, 1–23.

Haidari, A. H. & Smith, C. R. 1994 The generation and regeneration of single hairpin vortices. *J. Fluid Mech.* **277**, 135–162.

Haritonidis, J. H., Gresko, S. K. & Breuer, K. S. 1988 Wall pressure peaks and waves. In *Near Wall Turbulence 1988 Zoran Zaric Memorial Conference* (ed. (S. J. Kline & N. H. Afgan), p. 397. Hemisphere.

Head, M. R. & Bandyopadhyay, P. 1981 New aspects of turbulent boundary layer structure. *J. Fluid Mech.* **107**, 297–338.

Her, J.-Y. 1986 The relation between wall pressure and the flow field in the wall region of a turbulent boundary layer. PhD thesis, Department of Ocean Engineering, Massachusetts Institute of Technology.

Hinze, J. O. 1969 *Turbulence, an Introduction to Its Mechanism and Theory*. McGraw Hill.

Honkan, A. 1994 An experimental study of the vortical structure of turbulent flows. PhD thesis, City University of New York.

Honkan, A. & Andreopoulos, J. 1993 Direct calibration mapping and data analysis in triple hot-wire anemometry. In *Thermal Anemometry* (ed. D. Stock, S. Serif & A. J. Smits). FED vol. 167, pp. 67–78. ASME.

Jorgensen, F. E. 1971 Directional sensitivity of wire and fibre-film probes. *DISA Information*, vol. 11, p. 31–37.

Jovanović, J., Ye, Q.-Y. & Durst, F. 1995 Statistical interpretation of the turbulent dissipation rate in wall-bounded flows. *J. Fluid. Mech.* **293**, 321–347.

Kasagi, N., Sumitani, Y., Suzuki, Y. & Iida, O. 1995 Kinematics of the quasi-coherent vortical structure in near-wall turbulence. *Intl J. Heat Fluid Flow* **16**, 2–10.

Kastrinakis, E. G. & Eckelmann, H. 1983 Measurement of streamwise vorticity fluctuations in a turbulent channel flow. *J. Fluid Mech.* **137**, 165–186.

Kim, J. & Antonia, R. 1993 Isotropy of the small scales of turbulence at low Reynolds number. *J. Fluid Mech.* **251**, 219–238.

Kim, J., Moin, P. & Moser, R. 1987 Turbulence statistics in fully developed channel flow at low Reynolds number. *J. Fluid Mech.* **177**, 133–166.

Klebanoff, P. S. 1954 Characteristics of turbulence in a boundary layer with zero pressure gradient. *NACA TN* 3178.

Klewicki, J. C. 1989 On the interactions between the inner and outer region motions in turbulent boundary layers. PhD dissertation, Michigan State University, East Lansing, Michigan.

Klewicki, J. C. & Falco, R. E. 1990 On accurately measuring statistics associated with small-scale structure in turbulent boundary layers using hot-wire probes. *J. Fluid Mech.* **219**, 119–142.

Kline, S. J., Reynolds, W. C., Schraub, F. A. & Runstadler, P. W. 1967 The structure of turbulent boundary layer. *J. Fluid Mech.* **30**, 741–773.

Kolmogorov, A. A. 1941 The local structure of turbulence in incompressible viscous fluid for very large Reynolds numbers. *C. R. Akad. Sci. SSSR* **30**, 301–306.

Kreplin, H. P. & Eckelman, H. 1979 Instantaneous direct of the velocity vector in a fully developed turbulent channel flow. *Phys. Fluids* **22**, 1210–1211.

Landahl, M. T. 1984 *Z. Flugwiss. Weltraumforsch.* **8**, 4, 233–242.

Lekakis, I. C., Adrian, R. J. & Jones, B. G. 1989 Measurement of velocity vectors with orthogonal and non-orthogonal triple sensor probes. *Exps. Fluids* **7**, 228.

Lemonis, G. C. 1995 An experimental study of the vector fields of velocity and vorticity in turbulent flows. Doctoral thesis, Swiss Federal Institute of Technology, Zürich, Institute of Hydro-mechanics and Water Resources.

Lighthill, M. J. 1963 *Boundary Layer Theory in Laminar Boundary Layers* (ed. L. Rosenhead). Oxford University Press.

Lu, L. J. & Smith, C. R. 1988 Image processing of hydrogen bubble flow visualization for quantitative evaluation of hairpin-type vortices as a flow structure of turbulent boundary layers. *Tech. Rep.* FM-14. Lehigh University.

LYMAN, F. A. 1990 Vorticity production at a solid boundary. *Appl. Mech. Rev.* **43**, 157–158.

MANSOUR, N. N., KIM, J. & MOIN, P. 1988 Reynolds-stress and dissipation-rate budgets in a turbulent channel flow. *J. Fluid Mech.* **194**, 15–44.

MARASLI, B., NGUYEN, P. & WALLACE, J. M. 1993 A calibration technique for multiple-sensor hot-wire probes and its application to vorticity measurements in the wake of a circular cylinder. *Exps. Fluids* **15**, 209–218.

MEINHART, C. D. & ADRIAN, R. J. 1995 Measurements of the zero-pressure-gradient turbulent boundary layer using particle image velocimetry. *AIAA Paper* 95-0789.

MOIN, P. & KIM, J. 1985 The structure of the vorticity field in a turbulent channel flow. Part 1. Analysis of instantaneous field and statistical correlations. *J. Fluid Mech.* **155**, 441–464.

MORRISON, J. F. & BRADSHAW, P. 1991 Bursts and sources of pressure fluctuation in turbulent boundary layers. *Eighth Symp. on Turbulent Shear Flows, Munich.*

MORRISON, J. F., SUBRAMANIAN, C. S. & BRADSHAW, P. 1992 Bursts and the law of the wall in turbulent boundary layers. *J. Fluid Mech.* **241**, 75–108.

PANTON, R. L. 1984 *Incompressible Flow*. John Wiley and Sons.

PERRY, A. E., LIM, T. T. & TEH, E. W. 1981 A visual study of turbulent spots. *J. Fluid Mech.* **104**, 387–405.

PURTELL, L. P., KLEBANOFF, P. S. & BUCKLEY, F. T. 1981 Turbulent boundary layer at low Reynolds number. *Phys. Fluids* **24**, 802–811.

RAJAGOPALAN, S. & ANTONIA, R. H. 1993 RMS spanwise vorticity measurements in a turbulent boundary layer. *Exps Fluids* **14**, 142–144.

ROBINSON, S. K. 1991 Coherent motions in the turbulent boundary layer. *Ann. Rev. Fluid Mech.* **23**, 601–639.

SCHEWE, G. 1983 On the structure and resolution of wall-pressure fluctuations associated with turbulent boundary-layer flow. *J. Fluid Mech.* **134**, 311–328.

SHE, Z.-S., JACKSON, E. & ORSZAG, S. A. 1991 Structure and dynamics of homogeneous turbulence. In *Turbulence and Stochastic Processes: Kolmogorov's Ideas 50 Years On* (ed. J. C. R. Hunt, O. M. Phillips & D. Williams). The Royal Society, London.

SMITH, C. R. & WALKER, J. D. A. 1995 Turbulent wall-layer vortices. In *Fluid Vortices* (ed. S. I. Green). Kluwer.

SORIA, J., SONDERGAARD, R., CANTWELL, B. J. & PERRY, A. E. 1994 A study of the fine-scale motions of incompressible time-developing mixing layers. *Phys. Fluids A* **6**, 871–883.

SPALART, P. R. 1988 Direct simulation of a turbulent boundary layer up to $R_\theta = 1410$. *J. Fluid Mech.* **187**, 61–98.

SPALDING, D. B. 1961 A single formula for the law of the wall. *Trans. ASME* E: *J. Appl. Mech.* **28**, 455–458.

TENNEKES, H. & LUMLEY, J. L. 1972 *A First Course in Turbulence*. MIT Press.

THEODORESEN, T. 1952 Mechanism of turbulence. *Proc. 2nd Midwestern Conf. on Fluid Mechanics, Ohio State University, Columbus, Ohio.*

TSINOBER, A., KIT, E. & DRACOS, T. 1992 Experimental investigation of the field of velocity gradients in turbulent flows. *J. Fluid Mech.* **242**, 169–192.

TUTU, N. K. & CHEVRAY, R. 19765 Cross-wire anemometry in high intensity turbulence. *J. Fluid Mech.* **71**, 785–800.

VRETTOS, N. 1984 Experimentelle Untersuchung der Ausbreitung von Kũlturmschwaden im Windkanal. Studienarbeit, University of Karlsruhe.

VUKOSLAVČEVIĆ, P. WALLACE, J. M. & BALINT, J. 1991 The velocity and vorticity vector fields of a turbulent boundary layer. Part 1. Simultaneous measurement by hot-wire anemometry. *J. Fluid Mech.* **228**, 25–51.

WALLACE, J. M., BALINT, J. & ONG, L. 1992 An experimental study of helicity density in turbulent flows. *Phys. Fluids* A **4**, 2013–2026.

WALLACE, J. M. & FOSS, J. 1995 The measurement of vorticity in turbulent flows. *Ann. Rev. Fluid Mech.* **27**, 469–514.

WEI, T. & WILLMARTH, W. W. 1989 Reynolds number effects on the structure of a turbulent channel flow. *J. Fluid Mech.* **204**, 57–95.

WILLMARTH, W. W. 1985 Geometric interpretation of the possible velocity vectors obtained with multiple sensor probes. *Phys. Fluids* **28**, 462–466.

WILLMARTH, W. W. & BOGAR, J. J. 1977 Surveys and new measurements of the turbulent structure near the wall. *Phys. Fluids* **20**, p. s9.

WU, J. C. & WU, J. M. 1996 Boundary vorticity dynamics since Lighthill's 1963 article – review and development. *Intl Symp. on Theoretical and Computational Fluid Dynamics*, *Nov. 1996*, *Florida State University*, *Tallahassee*, *FL*.

WYNGAARD, J. C. 1969 Spatial resolution of the vorticity meter and other hot-wire arrays. *J. Phys* E: *Sci. Instrum.* **2**, 983–987.